

*Russian Original Vol. 59, No. 1, July, 1985*

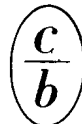
January, 1986

SATEAZ 59(1) 531-630 (1985)

# SOVIET ATOMIC ENERGY

АТОМНАЯ ЭНЕРГИЯ  
(ATOMNAYA ÉNERGIYA)

TRANSLATED FROM RUSSIAN



CONSULTANTS BUREAU, NEW YORK

# SOVIET ATOMIC ENERGY

*Soviet Atomic Energy* is abstracted or indexed in *Chemical Abstracts*, *Chemical Titles*, *Pollution Abstracts*, *Science Research Abstracts*, *Parts A and B*, *Safety Science Abstracts Journal*, *Current Contents*, *Energy Research Abstracts*, and *Engineering Index*.

*Soviet Atomic Energy* is a translation of *Atomnaya Energiya*, a publication of the Academy of Sciences of the USSR.

An agreement with the Copyright Agency of the USSR (VAAP) makes available both advance copies of the Russian journal and original glossy photographs and artwork. This serves to decrease the necessary time lag between publication of the original and publication of the translation and helps to improve the quality of the latter. The translation began with the first issue of the Russian journal.

## Editorial Board of *Atomnaya Energiya*:

**Editor:** O. D. Kazachkovskii

**Associate Editors:** A. I. Artemov, N. N. Ponomarev-Stepnoi, and N. A. Vlasov

I. A. Arkhangel'skii  
I. V. Chuvilo  
I. Ya. Emel'yanov  
I. N. Golovin  
V. I. Il'ichev  
P. L. Kirillov  
Yu. I. Koryakin  
E. V. Kulov  
B. N. Laskorin  
V. V. Matveev

A. M. Petras'yants  
E. P. Ryazantsev  
A. S. Shtan  
B. A. Sidorenko  
Yu. V. Sivintsev  
M. F. Troyano  
V. A. Tsykanov  
E. I. Vorob'ev  
V. F. Zelenskii

Copyright © 1986, Plenum Publishing Corporation. *Soviet Atomic Energy* participates in the Copyright Clearance Center (CCC) Transactional Reporting Service. The appearance of a code line at the bottom of the first page of an article in this journal indicates the copyright owner's consent that copies of the article may be made for personal or internal use. However, this consent is given on the condition that the copier pay the flat fee of \$9.50 per article (no additional per-page fees) directly to the Copyright Clearance Center, Inc., 27 Congress Street, Salem, Massachusetts 01970, for all copying not explicitly permitted by Sections 107 or 108 of the U.S. Copyright Law. The CCC is a nonprofit clearinghouse for the payment of photocopying fees by libraries and other users registered with the CCC. Therefore, this consent does not extend to other kinds of copying, such as copying for general distribution; for advertising or promotional purposes, for creating new collective works, or for resale, nor to the reprinting of figures, tables, and text excerpts. 0038-531X/85/\$09.50

Consultants Bureau journals appear about six months after the publication of the original Russian issue. For bibliographic accuracy, the English issue published by Consultants Bureau carries the same number and date as the original Russian from which it was translated. For example, a Russian issue published in December will appear in a Consultants Bureau English translation about the following June, but the translation issue will carry the December date. When ordering any volume or particular issue of a Consultants Bureau journal, please specify the date and, where applicable, the volume and issue numbers of the original Russian. The material you will receive will be a translation of that Russian volume or issue.

## Subscription (2 volumes per year)

Vols. 58 & 59: \$645 (domestic); \$715 (foreign)      Single Issue: \$100  
Vols. 60 & 61: \$695 (domestic); \$770 (foreign)      Single Article: \$9.50

## CONSULTANTS BUREAU, NEW YORK AND LONDON



233 Spring Street  
New York, New York 10013

Published monthly. Second-class postage paid at Jamaica, New York 11431.

Mailed in the USA by Publications Expediting, Inc., 200 Meacham Avenue, Elmont, NY 11003.

**POSTMASTER:** Send address changes to *Soviet Atomic Energy*, Plenum Publishing Corporation, 233 Spring Street, New York, NY 10013.

# SOVIET ATOMIC ENERGY

A translation of *Atomnaya Énergiya*

January, 1986

Volume 59, Number 1

July, 1985

## CONTENTS

Engl./Russ.

### ARTICLES

- Recommendations on Calculating the Heat-Transfer Crisis in Pipes on the Basis of a Bank of Experimental Data - P. L. Kirillov, V. P. Bobkov, V. N. Vinogradov, A. A. Ivashkevich, O. L. Peskov, and I. P. Smogalev..... 531 3
- Energy-Liberation Field in the Active Zone of a Boiling-Water-Reactor - A. A. Marakazov, Yu. A. Styurin, and A. A. Suslov..... 539 9
- Taking Account of Height Constraints in Problems of Optimizing the Spatial Energy Distribution - N. A. Kuznetsov, P. T. Potapenko, G. N. Shelepin, O. L. Bozhenkov, and V. V. Mal'tsev..... 546 13
- Reconstruction of the Fields of Physical Quantities in RBMK - A. D. Zhirnov, V. D. Nikitin, A. P. Sirotkin, and V. P. Shaposhnikov..... 553 18
- Complex Radiation Monitoring of the Fuel Distribution in Vibration-Packed Fuel Elements - L. I. Kosarev, N. R. Kuzelev, A. N. Maiorov, A. S. Shtan', and V. M. Yumashev..... 558 22
- A Study of the High-Temperature Creep in Coarse-Grained Uranium Dioxide - A. A. Gridnev, D. N. Dzalandinov, P. V. Zubarev, and A. S. Panov..... 565 27
- Calculation of the Displacement Peaks in the Continuum Approximation - V. P. Zhukov and A. V. Demidov..... 568 29
- Effect of Helium Blistering on the Hydrogen Permeability of the Kh18N10T Stainless Steel - V. M. Sharapov, A. I. Pavlov, A. P. Zakharov, M. I. Guseva, and V. N. Kulagin..... 574 33
- Growth of Helium Pores in the Vicinity of and at the Grain Boundaries - A. I. Ryazanov, G. A. Arutyunova, V. A. Borodin, V. M. Manichev, Yu. N. Sokurskii, and V. I. Chuev..... 577 35
- Hydrogen Permeability in Stainless Steel Interacting with TM-4 Tokamak Plasma - V. I. Bugarya, S. A. Grashin, A. V. Pereslavl'tsev, Yu. M. Pustovoi, V. S. Svishchev, A. I. Livshits, and M. E. Notkin..... 584 40
- Microwave Beam Instability in Proton Synchrotrons - V. I. Balbekov and S. V. Ivanov..... 587 42
- Calculation of the Effects of Neutron Activation of Nuclei for Cases of Superposition of the Signal in Gamma Activation Analysis - A. P. Ganzha, M. G. Davydov, E. M. Davydov, and E. M. Shomurov..... 598 49
- Excitation Cross Section of the Characteristic X Radiation by Protons and He Ions for Elements with  $Z$  in the Range  $22 \leq Z \leq 83$  - E. Brazevich, Ya. Brazevich, V. F. Volkov, S. A. Gerasimov, Lyu Zai Ik, G. M. Osetinskii, and A. Purév..... 603 52
- ### LETTERS TO THE EDITOR
- Influence of Reactor Irradiation upon the Electrophysical Characteristics of Heteroepitaxial p-Silicon-On-Sapphire Layers - B. V. Koba, V. L. Litvinov, A. L. Ocheretyanskii, V. M. Stuchebnikov, I. B. Fedotov, N. A. Ukhin, V. V. Khasikov, and V. N. Chernitsyn..... 610 58

**CONTENTS**

(continued)

Engl./Russ.

Calculation and Experimental Investigation of the Heat Removal Modes of a Shutdown BN-600 Reactor of the Beloyarsk Nuclear Power Station - A. I. Karpenko, A. A. Lyzhin, and A. G. Sheinkman.....	613	60
Influence of the Change in Moisture Content of Atmosphere Air on the Distribution of the Cosmic-Background Neutron Fluxes above a Water Surface - E. M. Filippov.....	616	61
A Pyroelectric Detector of Gamma Radiation with Compensation for the Compton-Electron Current - V. A. Borisenok, E. Z. Novitskii, E. V. Vagin, S. A. Pimanikhin, and V. D. Sadunov.....	620	63
Polynomial Representation of the Bremsstrahlung Spectra of a Thick Target for Electrons of Energy 10-22 MeV - V. E. Zhuchko and Zen Chan Uk.....	622	65
Heat-Transfer Coefficient with Glancing Flow Around Fuel Elements and Tubes - Yu. S. Yur'ev and A. D. Efanov.....	624	66
Using Cadmium Telluride Detectors for the X-Ray Fluorescence Analysis of Uranium Solutions - V. V. Berdikov, A. V. Vasil'ev, O. I. Grigor'ev, B. S. Iokhin, and A. Kh. Khusainov.....	626	67
Half-Lives of the Spontaneous Fission of $^{239}\text{Pu}$ and $^{241}\text{Pu}$ - A. A. Druzhinin, V. N. Polynov, A. M. Korochkin, E. A. Nikitin, and L. I. Lagutina.....	628	68

The Russian press date (podpisano k pechatu) of this issue was 6/28/1985.  
Publication therefore did not occur prior to this date, but must be assumed  
to have taken place reasonably soon thereafter.

# RECOMMENDATIONS ON CALCULATING THE HEAT-TRANSFER CRISIS IN PIPES ON THE BASIS OF A BANK OF EXPERIMENTAL DATA

P. L. Kirillov, V. P. Bobkov,  
V. N. Vinogradov, A. A. Ivashkevich,  
O. L. Peskov, and I. P. Smogalev

UDC 536.2

Existing recommendations on calculating critical heat fluxes appear to have some disadvantages. For example, in the tables in [1] and in [2], data are recommended for calculating these fluxes over restricted ranges in mass flow rate and steam content at the exit ( $x \leq x_{lj}$ ). It is not always convenient to use such tables. The calculation method of [3] is complicated for engineering purposes because of the multiplicity of tabulated values for the properties of water and steam, which are dependent on temperature.

The most reliable recommendations can be derived from a large body of experimental data. As has already been communicated [4], the Thermophysical Data Center at the Power Physics Institute has formulated computerized data banks. About 23,000 experimental points have been recorded in the bank on the heat-transfer crisis in the boiling of water, including data for uniform and nonuniform heating. The bank includes the data of [3] (about 1500 experimental points) and the data from check experiments (2579 experimental points). Table 1 gives the ranges in working and geometrical parameters for uniform heating for the collection of about 14,200 experimental points in the bank.

Control experiments have been performed on the heat-transfer crisis for water in tubes with uniform energy deposition in the USSR during 1979-1982. There were 10 organizations participating. The experiments were performed with identical values of the working and geometrical parameters involving the use of the methods for measuring flow rate, temperature, pressure, and other parameters adopted in those organizations. The main purposes of the experiments were to determine the discrepancies between organizations, to elucidate the reasons for the discrepancies, and to check and refine the recommendations for calculating the heat-transfer crisis.

Preliminary information has been given in [5] on these experiments. Table 2 gives the distributions of the experimental points by mode and geometrical parameters. The following are major points in the statistical analysis of the data set:

- 1) There are considerable differences in the numbers of points provided by the different organizations (from 28 to 629), and these points (from 15 to 119) are unevenly distributed over the working parameters (Table 3);
- 2) there was no preliminary researcher's evaluation of the data accuracy;
- 3) in some of the experiments, the working parameters deviated from the agreed nominal values.

These features to some extent complicate the data processing. The values for diameters differing from nominal (8 mm) were first referred to the nominal value via the formula  $N_{cr} = N_{crd}(8/d)^n$ , where the values of  $n$  were taken in accordance with the recommendations of [6]:

$p$ , MPa	6,9	9,8	13,7	17,7
$n$	0,673	0,511	0,201	0,021

As the deviations in tube diameter did not exceed 3.6%, this correction in most cases was less than 2.1%.

The data from the control experiments were evaluated statistically as regards the conformity between organizations. A preliminary study of the dependence of the critical power

---

Translated from *Atomnaya Energiya*, Vol. 59, No. 1, pp. 3-8, July, 1985. Original article submitted January 30, 1984; revision submitted December 14, 1984.

TABLE 1. Data Structure in Bank

Pressure MPa	Water flow, kg/h	Tube diam., mm	Tube length, m	No. of exptl. points
1,0-5,9	57-1200	2-11	0,04-6,05	930
6,9	85-1220	4-15,1	0,25-6,0	1470
7,3-7,8	57-1220	2-15,1	0,04-6,0	1020
9,8	57-2140	2-15,1	0,04-6,0	2250
11,8	100-2040	4-15,1	0,25-6,0	920
12,2-12,7	57-1280	2-16	0,04-6,0	600
13,7	70-1900	4-15,1	0,25-6,0	2000
14,7	57-1490	2-15,1	0,04-6,0	1350
15,7	140-1950	3,8-15,1	0,25-6,0	840
17,1-17,6	57-1940	2-15,1	0,04-6,0	2070
19,6	57-2070	2-15,1	0,04-6,0	730

TABLE 2. Results from Experimental Data Provided by Various Organizations

Organization No.	No. of exptl. points	Arithmetic mean devia. $\Delta$ , %	SD $\sigma$ , %
1	249	1,33	6,76
2	60	-6,84	11,12
3	190	0,96	6,15
4	477	2,18	6,7
5	629	-1,03	6,43
6	33	-1,15	5,3
7	273	-0,4	6,14
8	223	-2,5	6,22
9	28	3,0	4,99
10	417	-0,68	6,5
For all organ- izations	2579	-0,16	6,6
For all organ- izations apart from No. 2 (Dzerzhinskii Power Institute)	2519	-0,00045	6,46

on the inlet temperature showed that this was close to linear. A detailed analysis showed that the quadratic term was not statistically significant. The dependence of  $N_{cr}$  on the working and geometrical parameters is more complicated. The following approximation was used:

$$N_{cr}(p, \rho w, l, t_{in}) = a(p, \rho w, l)[1 - b(p, \rho w, l)t_{in}]. \quad (1)$$

At the stage of preliminary analysis, we selected the form of the functions

$$a(p, \rho w, l) \text{ and } b(p, \rho w, l),$$

where

$$a = a_1 + a_2 p + a_3 \rho w + a_4 (\rho w)^2 + a_5 (\rho w)^3 + a_6 \rho w p + a_7 \frac{\rho w}{lp} + a_8 \frac{\rho w}{lp^2} + a_9 \frac{(\rho w)^2}{lp^2} + a_{10} \frac{l^2}{p^3} + a_{11} \frac{1}{(lpw)^2} + \quad (2)$$

$$+ a_{12} l + a_{13} l \rho w + a_{14} l (\rho w)^2 + a_{15} l p \rho w + a_{16} l^2 + a_{17} l^2 \rho w + a_{18} l^2 (\rho w)^2 + a_{19} (p \rho w)^2;$$

$$b = b_1 + b_2 l + b_3 \rho w + b_4 l \rho w + b_5 (\rho w)^2 + b_6 l (\rho w)^2 + b_7 \frac{1}{lp \rho w} + b_8 l \rho w p^3 + b_9 \frac{(\rho w)^3}{(lp)^3}. \quad (3)$$

p, MPa	$\rho w$ , kg/m <sup>2</sup> · sec	l, mm	No. of exptl. points	$\Delta$ , %, from (1)	$\sigma$ , %, from (1)	$\Delta$ , %, from (10)– (11)	$\sigma$ , %, from (10)– (11)	p, MPa	$\rho w$ , kg/m <sup>2</sup> · sec	l, mm	No. of exptl. points	$\Delta$ , %, from (1)	$\sigma$ , %, from (1)	$\Delta$ , %, from (10)– (11)	$\sigma$ , %, from (10)– (11)
6,9	500	1000	44	5,40	7,08	–6,77	8,02	13,7	1000	3000	89	3,48	4,70	1,39	3,73
6,9	1000	1000	78	–4,19	8,13	–1,37	5,25	13,7	2000	3000	99	5,3	6,2	3,16	4,70
6,9	2000	1000	101	3,32	8,0	0,25	4,89	13,7	4000	3000	58	0,29	4,73	–1,98	8,45
6,9	4000	1000	56	–3,76	6,52	0,81	10,71	17,6	500	3000	43	–0,46	5,27	–3,70	5,6
9,8	500	1000	45	0,61	3,33	0,57	3,57	17,6	1000	3000	62	3,07	4,56	–0,05	3,27
9,8	1000	1000	83	–4,92	7,35	–4,22	6,87	17,6	2000	3000	77	–4,0	5,69	–2,20	4,08
9,8	2000	1000	114	2,17	6,06	–1,92	6,46	17,6	4000	3000	53	–2,99	4,82	1,97	5,71
9,8	4000	1000	49	4,79	9,93	7,13	12,02	6,9	500	6000	13	–9,3	16,8	–0,68	1,10
13,7	500	1000	47	1,09	5,52	–8,84	9,72	6,9	1000	6000	41	–3,65	8,0	10,02	12,13
13,7	1000	1000	71	1,9	6,63	–4,07	6,54	6,9	2000	6000	42	–2,46	5,32	7,08	8,68
13,7	2000	1000	108	2,42	6,97	1,82	6,12	6,9	4000	6000	15	–6,68	8,23	–4,49	9,58
13,7	4000	1000	35	–0,83	4,99	–1,75	5,03	9,8	500	6000	16	2,68	5,48	5,09	6,02
17,6	500	1000	49	–4,02	7,4	–6,72	8,63	9,8	1000	6000	43	0,38	3,66	11,30	13,13
17,6	1000	1000	52	4,64	8,2	2,99	5,18	9,8	2000	6000	42	3,05	5,9	4,08	7,24
17,6	2000	1000	81	–1,11	5,96	–1,10	6,40	9,8	4000	6000	21	–3,29	5,55	3,62	7,73
17,6	4000	1000	41	–1,01	8,67	–2,27	8,04	13,7	500	6000	17	1,73	2,3	9,09	11,16
6,9	500	3000	36	5,7	7,7	–2,67	4,11	13,7	1000	6000	45	2,70	7,71	13,82	18,35
6,9	1000	3000	65	–9,4	10,33	3,23	5,18	13,7	2000	6000	45	3,26	5,02	6,66	8,19
6,9	2000	3000	72	–6,3	7,5	1,32	4,4	13,7	4000	6000	27	2,83	5,9	–3,64	8,89
6,9	4000	3000	49	–6,6	8,41	–4,10	7,19	17,6	500	6000	18	–6,9	7,48	2,70	3,18
9,8	500	3000	38	–0,28	4,55	2,29	4,38	17,6	1000	6000	31	–4,7	5,52	1,99	4,22
9,8	1000	3000	85	–4,04	4,7	1,18	3,33	17,6	2000	6000	25	–5,0	7,06	0,68	4,13
9,8	2000	3000	119	–1,6	4,63	–4,18	5,51	17,6	4000	6000	15	–1,79	9,79	–1,17	6,67
9,8	4000	3000	81	3,34	5,14	9,00	10,00	For complete set of data from control expt.				–0,16	6,6		
13,7	500	3000	43	4,64	7,17	–0,92	4,7				2579				

We used the following scales for the numerical data:

$$N_{cr} = N_{cr}/100; p = p/10; \rho w = \rho w/1000; t = t/100; l = l/1000. \quad (4)$$

Here  $N_{cr}$  is in kW,  $p$  in MPa,  $\rho w$  in kg/m<sup>2</sup>·sec,  $t$  in °C, and  $l$  in mm.

Although the functions of (1)–(3) are linear in the parameters  $a_i$  and  $b_i$ , the linear problem could not be handled by least squares since the values of the variables  $p$ ,  $\rho w$ ,  $l$ , and  $t$  differed from the nominal values and did not cover the necessary ranges. To determine the optimum coefficients in (2) and (3), we used unconditional nonlinear Davidson–Fletcher–Powell minimization [7]. There was no evaluation of the experimental errors by the original researchers, which meant that a minimizing functional had to be used. There are only comparatively small changes in the critical power (by factors of 2–3), and this with the study of the methods led us to choose the relative standard deviation as the functional fitted to the experimental points:

$$\sigma^2 = \frac{1}{n-28} \sum_{i=1}^n \Delta_i^2 = \frac{1}{n-28} \sum_{i=1}^n \left[ \frac{N_{cr,i}^c - N_{cr,i}^e}{N_{cr,i}^e} \right]^2, \quad (5)$$

which gives an estimator for the relative (weighted) variance. Here  $n = 2579$  is the number of experimental points, 28 is the number of coefficients in (2) and (3),  $N_{cr,i}^e$  are the experimental values of the critical power, and  $N_{cr,i}^c$  are the calculated approximating values at the corresponding points.

Table 4 gives the optimized coefficients. The general results in Tables 2 and 3 indicate a satisfactory approximation by groups and for the data as a whole.

The results in Table 2 deserve separate analysis; it implies that the data from all organizations apart from one are statistically in agreement. One can use Dixon's criterion [8] to analyze for anomalies in the sample elements from the organizations. This criterion is of ranking type for small sets and characterizes the deviations of one or more elements in a series from the adjacent terms. The test indicates reliably that the data from organization No. 2 (Table 2) are statistically anomalous at the 95% confidence level: on average

$i$	1	2	3	4	5
$a_i$	0,447688	-0,214717	0,2444943	0,0508382	-0,00348812
$b_i$	0,144131	0,00857681	0,0610103	-0,00482804	-0,00882715

$i$	6	7	8	9	10
$a_i$	0,0844160	-0,0940023	0,142995	-0,0338257	0,00164519
$b_i$	$0,32836 \cdot 10^3$	-0,00858400	$-0,329807 \cdot 10^3$	$0,138139 \cdot 10^3$	

$i$	11	12	13	14	15
$a_i$	$-0,999607 \cdot 10^3$	$-0,961122 \cdot 10^4$	0,243949	-0,0419301	-0,0030037

$i$	16	17	18	19
$a_i$	-0,00125827	-0,0243218	0,00437281	0,00340268

TABLE 5. Deviations in the Dzerzhinskii Power Institute Data by Groups of Working Parameters

$l, m$	$p, \text{MPa}$	$\rho w, \text{kg/m}^2 \cdot \text{sec}$	No. of points	$\Delta, \%$	$\sigma, \%$
1	9,8	1000	8	-15	17
1	9,8	2000	10	-8,7	9,68
1	13,7	1000	6	-5,19	9,45
1	13,7	2000	8	-8,83	10,18
1	13,7	4000	7	-0,66*	3,17
1	17,6	1000	7	5,66	12,66
1	17,6	2000	6	-3,48*	10,02
1	17,6	4000	8	-13,72	15,07
From all the Dzerzhinskii Power Institute data			60	-6,84	11,12

they are higher than those from the other organizations. Dixon's test applied to the data from the other organizations indicates statistical homogeneity. The following point is notable: out of the 48 matched groups of working parameters, organization No. 2 presented data only for 8 groups and for one length (Table 5). Table 5 shows that small deviations occur only in one group of the data (indicated by asterisks). Here we do not examine the reasons for the deviations, although separate consideration should be given to various points in the design of the Power Institute system and the method of producing the two-phase flow in it.

Marinelli [9] reported a special study performed in Western European laboratories and designed to estimate the reproducibility in data on the heat-transfer crisis. There were



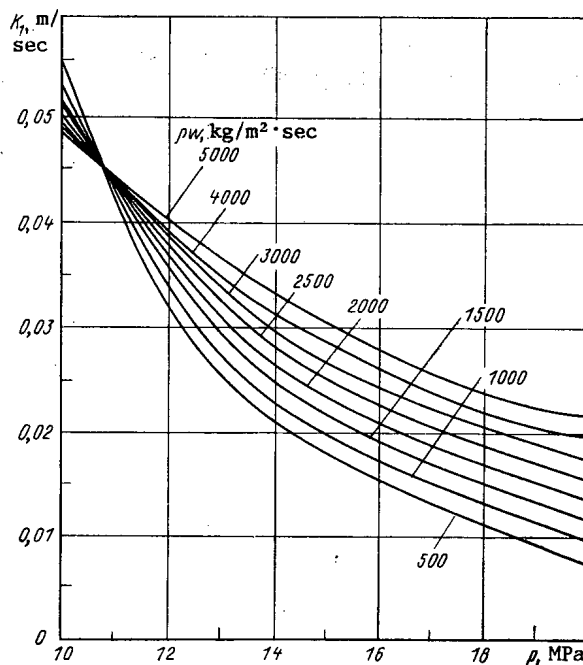
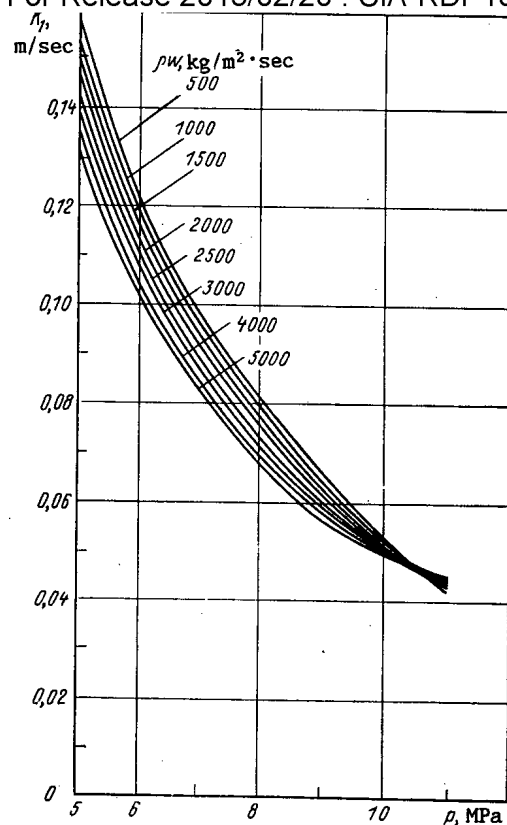
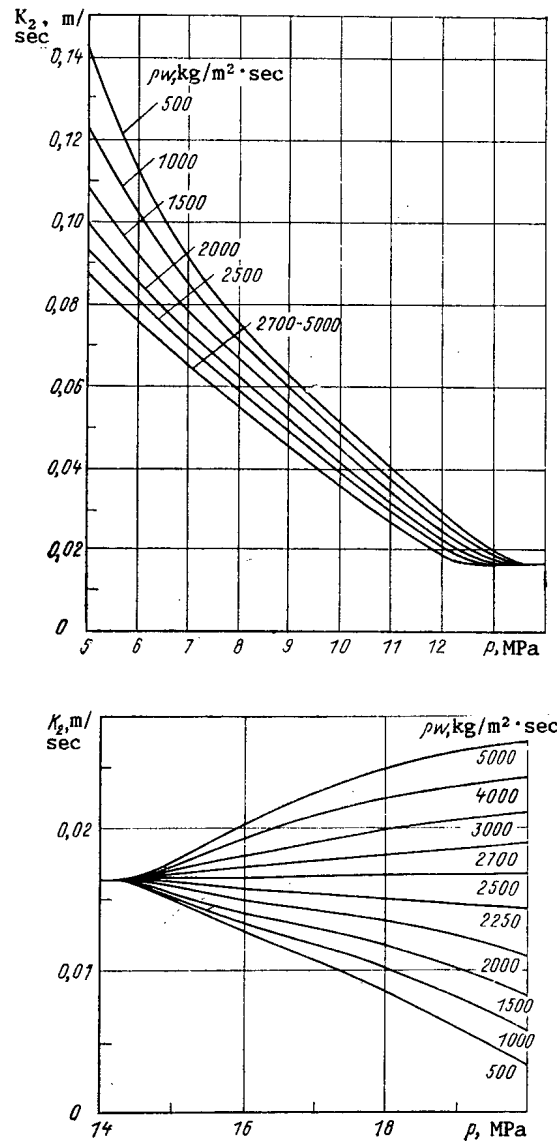


Fig. 1. Graph (nomogram) for determining  $K_1$ .

589 experiments on identical circular tubes ( $d_{in} = 10$  mm,  $l = 2$  m) at 3-9 MPa and  $\rho w = 200$ -6000  $\text{kg/m}^2 \cdot \text{sec}$ . A comparison of 363 points covering the range of parameters represented by the data from all laboratories showed that there were discrepancies of up to 30% for certain data groups from two laboratories by comparison with the results from the others. If we neglect these anomalous data, the standard deviation for the 268 points is 4.2%, the maximum deviations being 14 and 19% on comparing the critical power levels by relation to the optimized dependence on this data set.

Fig. 2. Graph. (nomogram) for determining  $K_2$ .

Practical use of the data bank requires simple and reliable relationships for the critical power. These should be based primarily on the reliable results following a detailed analysis and should have adequate accuracy and the widest possible working range. We devised a simple method for calculating the critical power for the flow of unheated water and for a steam-water flow. The method is based on the formula

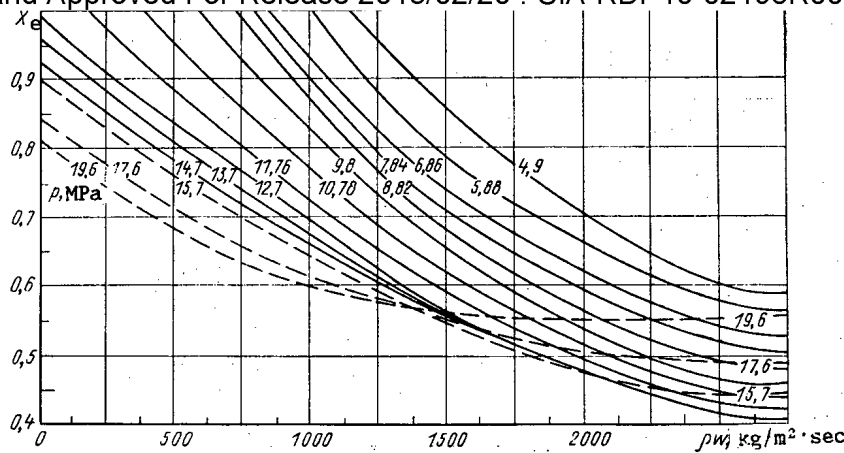
$$N_{cr} = \pi d l K r \rho'' \frac{x_e - x_{in}}{x_e + C}, \quad (6)$$

where

$$C = \frac{K l \rho''}{d (\rho w)};$$

in which  $K$  and  $x_e$  are empirical functions of the pressure and mass velocity,  $r$  is the latent heat of evaporation,  $\rho''$  is the steam density,  $d$  is diameter, and  $l$  is length.

The physical basis of these formulas is given in [10]. The numerous empirical formulas given in the literature at various times [11, 12] confirm the relationship, since they can be reduced to (6).

Fig. 3. Graph (nomogram) for determining  $x_{e1}$ .

From our viewpoint, the working formulas for the critical power as a function of the stream content (or inlet temperature) are more reliable than the values for the critical heat flux density as a function of the critical steam content and are of greater practical value. This is mainly because  $N_{cr}$  and  $t_{in}$  are primary experimental data. On the other hand, the critical power in a uniformly heated tube is much the same as that in a tube with a cosine distribution of the heat flux along the length (the discrepancies do not exceed  $\pm 10\%$ ) if the distribution is not too sharply varying ( $q_{max}/q_{av} < 1.5$ ) [6].

On solving (6) with the heat-balance equation for the tubes, we find that the relation between  $q_{cr}$  and  $x_{cr}$  is linear:

$$q_{cr}/K\rho'' = 1 - (x_{cr}/x_e). \quad (7)$$

Usually [3], the entire range in the critical steam content is split up into three characteristic zones. The first is the region of underheating and of steam contents less than  $x_{li}$ , which extends up to the kink in the  $q_{li} = f(x_{li})$  relation. The second is the region of dispersed annular flow. In that range,  $q_{cr} = f(x_{cr})$  may have a slope differing from that in the first zone. In the third zone, which corresponds to large values of the critical steam content, the slope of  $q_{cr} = f(x_{cr})$  also alters. The third zone is of little practical significance and is usually not considered. This division is now obvious, since it is related to modes of flow in the steam-water mixture and differences in the nature of the crisis. Therefore, the suggestions made in [3] are advantageous.

The linear relationship of (7), but with a relatively large slope, was used to simplify the calculations without altering the form of the relationship in the second zone when  $x_{cr} \approx x_{li}$ . In general, this does not correspond to the actual situation, but it greatly simplifies the calculations without increasing the error substantially.

Therefore, we divide the entire range of critical steam contents into two basic zones. In each of these zones,  $q_{cr} = f(x_{cr})$  is taken as linear. The slope in each zone is defined by the empirical parameter  $K$ , while the point of intersection with the steam content axis is defined by  $x_e$ , and the boundary between the zones is defined by the point of intersection between the two straight lines, which is close to  $x_{li}^0$  not only in physical significance but also in absolute value [2, 13, 14]. The empirical functions  $K_1$ ,  $K_2$ ,  $x_{e1}$ ,  $x_{e2}$  are derived from the experimental data [3, 6]. It is found that one can take  $x_{e1} = 0.7 x_{e2}$ , no matter what the values of  $p$  and  $\rho w$ . The values of these parameters are given in Figs. 1-3. As the  $q_{cr} = f(x_{cr})$  dependence is only slightly affected by the tube diameter, we introduced a factor reflecting the effects of the diameter on  $K_1$  and  $K_2$  in the form

$$m = \left( \frac{12 \cdot 10^{-3}}{d} \right)^{0.4}.$$

The critical power is calculated as follows:

1) One determines the boundary  $x_{li}$  between the first and second zones. Here it is necessary to find the point of intersection between the straight lines from the formula

$$x_{li} = x_{e2} \frac{K_1 - K_2}{K_1 - 1.43K_2}. \quad (8)$$

2) One finds the approximate value of the critical steam content from

$$x_{cr} = x_{e2} \frac{C_2 m + x_{in}}{C_2 m + x_{e2}}, \quad (9)$$

where

$$C_2 = \Delta K_2 l \rho'' / d \rho w.$$

This formula has been obtained on solving (7) with the heat-balance equation. The values of the empirical parameters correspond to the first zone. Therefore, the formula is exact for the second zone but approximate for the first one. As it is necessary to calculate  $x_{cr}$  in this case only to determine the region or zone, this simplification does not introduce a substantial error.

3) The zone in which  $x_{cr}$  falls (the first if  $x_{cr} < x_{li}$  and the second if  $x_{cr} > x_{li}$ ) is used to determine the critical power from the formula

$$N_{cr,i} = K_i r \rho'' \left( \frac{x_{ei} - x_{in}}{m C_i + x_{ei}} \right) F m, \quad (10)$$

where  $i = 1$  for the first zone and  $i = 2$  for the second. In (10)

$$C_1 = \frac{4K_1 l \rho''}{d \rho w}; \quad C_2 = \frac{4K_2 l \rho''}{d \rho w};$$

$$F = \pi d l; \quad m = \left( \frac{12 \cdot 10^{-3}}{d} \right)^{0.4}; \quad x_{e1} = 0.7 x_{e2}$$

(here  $K$  is in m/sec,  $r$  in kJ/kg,  $\rho''$  in kg/m<sup>3</sup>,  $l$  in m,  $N_{cr}$  in kW,  $\rho w$  in kg/m<sup>2</sup>·sec, and  $d$  in m).

If routine calculations are required, the graphical information for these parameters can be loaded into the computer by standard programs.

We compared the calculated and observed  $N_{cr}$  over wide ranges in the working and geometrical parameters ( $4.9 \leq p \leq 18$  MPa;  $500 \leq \rho w \leq 5000$  kg/(m<sup>2</sup>·sec);  $1 \leq l \leq 6$  m;  $8 \cdot 10^{-3} \leq d \leq 20 \cdot 10^{-3}$  m), which showed that the standard deviation was not more than 7%. Table 3 compares calculations from (10) with the data from the control experiments. We checked the formula on the basis of the earlier data from the Power Physics Institute and the Boiler and Electrical Turbine Research Institute [3, 6] over the ranges  $p = 5-20$  MPa,  $\rho w = 500-5000$  kg/(m<sup>2</sup>·sec),  $l = 0.25-6.5$  m;  $d = 3.8-17$  mm (a total of 9967 points), which indicated a satisfactory agreement ( $\Delta = 0.04\%$ ,  $\sigma = 13.8\%$ ).

The following conclusions are therefore drawn:

1. The data on the critical power obtained by various workers at different times in the main are in agreement one with another and with the data from the control experiments.

2. Optimized formulas have been derived for calculating  $N_{cr}$  in the boiling of water in uniformly heated tubes for fairly wide ranges in the defining parameters. Arithmetic means and standard deviations have been obtained. In computer calculations for tubes of diameter 8 mm, one can use (1)-(3), which describe the experimental data with the error given in Table 3.

1. Recommendations on Calculating the Heat-Transfer Crisis for Water Boiling in Circular Tubes [in Russian], Preprint 1-57, IVT Akad. Nauk SSSR, Moscow (1980), p. 68.
2. V. E. Doroshchuk, Heat-Transfer Crises in the Boiling of Water in Tubes [in Russian], Énergoizdat, Moscow (1983), p. 120.
3. V. N. Smolin et al., "Experimental data and calculation methods on the heat-transfer crisis in the boiling of water circulating in tubes with uniform and nonuniform heat deposition," Aspects of Nuclear Science and Engineering, Reactor Physics and Engineering Series [in Russian], Issue 5(9) (1979), pp. 3-154.
4. V. P. Bobkov et al., "The thermophysical data center for nuclear power systems," At. Energ., 53, Issue 3, 183-184 (1982).
5. P. L. Kirillov, N. P. Serdun', and O. L. Peskov, "A control experiment on the heat-transfer crisis for the boiling of water in tubes," At. Energ., 57, Issue 6, 422-423 (1984).
6. B. A. Zenkevich et al., Analysis and Generalization of Experimental Data on the Heat-Transfer Crisis in the Forced Flow of Boiling Water in Tubes [in Russian], Atomizdat, Moscow (1969).
7. D. M. Himmelblau, Applied Nonlinear Programming, McGraw-Hill (1972).
8. D. M. Himmelblau, Process Analysis by Statistical Methods, Wiley (1970).
9. V. Marinelli, "Critical heat flux: a review of recent publications," Nucl. Technol., 34, No. 2, 135-171 (1977).
10. P. L. Kirillov and I. P. Smogalev, "Analysis of the heat-transfer crisis on the basis of a droplet deposition model," Teplofiz. Vys. Temp., 11, No. 4, 794-804 (1973).
11. O. V. Remizov, The Heat-Transfer Crisis in Tubes: an Analytical Survey, Parts I and II [in Russian], OB-9, Obninsk (1975), p. 138.
12. P. L. Kirillov, "Calculating critical heat loads for boiling in tubes for water below the saturation temperature (uniformly distributed heat load)," in: The Heat-Transfer Crisis for Boiling in Channels [in Russian], Obninsk (1974), pp. 100-173.
13. P. L. Kirillov, I. P. Smogalev, and M. Ya. Suvorov, "The flow limits for a steam-water mixture with rapid droplet deposition," Teplofiz. Vys. Temp., 14, No. 1, 139-145 (1976).
14. É. F. Gal'chenko and V. V. Sergeev, "Generalizing from data on limiting steam contents," Teploenergetika, No. 3, 58-59 (1983).

#### ENERGY-LIBERATION FIELD IN THE ACTIVE ZONE OF A BOILING-WATER-WATER REACTOR

A. A. Marakazov, Yu. A. Styurin,  
and A. A. Suslov

UDC 621.039.5:681.3

At present, a promising type of reactor for AST built in the USSR is the vessel reactor with a boiling water moderator-coolant and natural circulation. For calculations of such reactors, in particular, for physical calculations of the active zone, a reasonable starting point is the program of physical calculation for water-cooled, water-moderated power reactors [1-3], the construction and operating conditions of which are similar to those adopted for AST reactors: hexagonal fuel-assembly geometry, regulation of the reactivity by inserting absorber clusters, conditions of partial reloading, etc. These programs belong to the category of large-grid algorithms [4] for calculating the active zone, which are intended to insure an acceptable computer calculation time with satisfactory accuracy of calculation of the energy-liberation field, effective breeder coefficient, and working life of the reactor. The method of physical calculation developed for a boiling water-water reactor, which is realized in the BIPR-K program, has the following features in comparison with the BIPR-series programs widely used for water-cooled, water-moderated reactors [1, 2]:

---

Translated from Atomnaya Énergiya, Vol. 59, No. 1, pp. 9-13, July, 1985. Original article submitted May 24, 1984; revision submitted August 13, 1984.

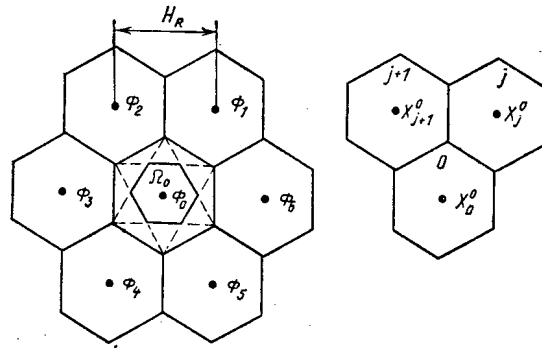


Fig. 1. Hexagonal calculation grid in the horizontal cross section of the active zone.

discontinuity of the moderating properties (diffusion coefficients and neutron-migration areas) of the active zone is taken into account;

a thermohydraulic-calculation module is provided, allowing the distribution of the density and flow rates of a steam-water mixture with a specified energy-liberation field in the active zone to be found (it is possible to consider both natural and induced circulation of the heat carrier);

the constants of the physical calculation are approximated by polynomial dependences describing the complex character of the feedback in conditions of moderator-coolant boiling.

In addition to calculating the state of the active zone (energy-liberation field and effective breeding factor), the BIPR-K program provides for simulation of fuel burnup, regulation of the reactivity, reloading, transient processes in adjusting the reactor power, etc. The method of calculating the energy-liberation field realized in the BIPR-K program (in other words, the principles of physical calculation of the reactor) is described below.

#### Formulation of the Problem

Consider a system of two-group diffusion equations

$$\begin{aligned} -\operatorname{div} D^b \operatorname{grad} \Phi^b(r) + (\Sigma_a^b + \Sigma_{in}^b) \Phi^b(r) &= \frac{1}{k_{ef}} [v \Sigma_f^b \Phi^b(r) + v \Sigma_f^t \Phi^t(r)]; \\ -\operatorname{div} D^t \operatorname{grad} \Phi^t(r) + \Sigma_a^t \Phi^t(r) &= \Sigma_{in}^t \Phi^b(r) \end{aligned} \quad (1)$$

in the three-dimensional region  $V$  consisting of some set of cells - regular hexahedral prisms. The prisms are formed by dividing the hexahedral fuel assemblies by a series of equally spaced horizontal planes. The coefficients of the system are assumed to be constant within the calculation cells and to have the usual meanings.

At the boundary  $G$  of region  $V$  in the direction of the external normal  $\bar{n}$ , the specified boundary conditions are assumed

$$\left. \frac{d\Phi^{b,t}}{dn} \frac{1}{\Phi^{b,t}} \right|_G = - \frac{1}{d^{b,t}}. \quad (2)$$

The extrapolation lengths  $d$  may be different for each of the cell boundaries at the boundary  $G$ . Both external boundaries (with a reflector) and internal boundaries (definite sections of the regulator not including fuel) are meant by  $G$ . The problem of determining the eigenvalues is solved and the minimum eigenvalue  $\lambda = 1/k_{ef}$  is found. The group neutron fluxes  $\Phi^b(r)$  and  $\Phi^t(r)$  are calculated, as well as the mean relative energy liberation over each of the cells

$$\bar{\Psi} = \Sigma_f^b \Phi^b(r) + \Sigma_f^t \Phi^t(r). \quad (3)$$

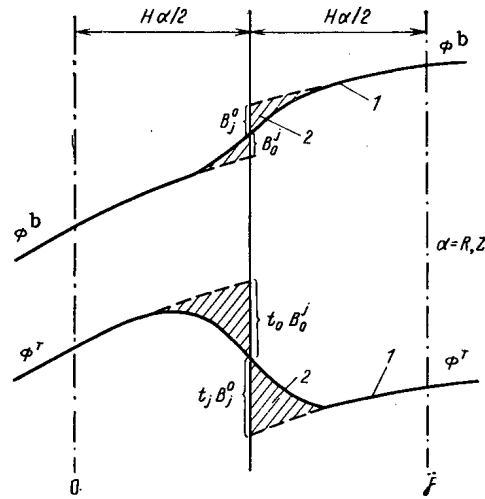


Fig. 2. Modal two-group model: 1) asymptotic mode; 2) transient mode.

### Method of Solution

In solving Eq. (1), a modal method is used, representing the group fluxes inside each cell in the form of a superposition of modes X and Y

$$\left. \begin{aligned} \Phi^b &= X + Y \\ \Phi^r &= rX + tY \end{aligned} \right\}. \quad (4)$$

Here X and Y satisfy Helmholtz equations

$$\Delta X + \mu^2 X = 0; \quad (5)$$

$$\Delta Y - v^2 Y = 0, \quad (6)$$

and

$$r = \frac{\Sigma_{in}^r}{\Sigma_a^r (1 + \mu^2 L_r^2)}; \quad t = \frac{\Sigma_{in}^b}{\Sigma_a^b (1 - v^2 L_r^2)};$$

$$\mu^2 = \frac{k_{\infty}/k_{ef} - 1}{M^2}; \quad L_r^2 = \frac{D^r}{\Sigma_a^r};$$

$$v^2 = \frac{1}{L_r^2} + \frac{1}{D^b} \left( \Sigma_a^b + \Sigma_{in}^b - \frac{1}{k_{ef}} v \Sigma_f^b \right) + \mu^2;$$

$$k_{\infty} = \frac{v \Sigma_f^b + v \Sigma_f^r}{\Sigma_a^b + \Sigma_a^r}; \quad M^2 = \frac{D^b + D^r}{\Sigma_a^b + \Sigma_a^r}.$$

Mode X is called the asymptotic mode; mode Y is the transient mode, and significantly influences the group fluxes only close to disturbance of the properties of the medium. This is because the following relations hold for the given types of water-water reactors

$$\mu^2 H_{\alpha}^2 \approx 1; \quad (7)$$

$$v^2 H_{\alpha}^2 \gg 1. \quad (\alpha = R, Z) \quad (8)$$

Here  $H_R$  is the lattice spacing of the fuel assembly (Fig. 1), and  $H_Z$  is the calculation step in the axial direction, which may be chosen so as to take account of the satisfaction of Eqs. (7) and (8).

To find the distribution of mode X over the whole of calculation region V, Eq. (5) is written in the form

$$-\operatorname{div} D^b \operatorname{grad} X + D^b \mu^2 X = 0$$

(9)

with characteristic values of  $D^b$  and  $\mu^2$  for each calculation cell.

By means of Eq. (7), it is possible to solve Eq. (9) using the finite-difference representation. The constructional principles of this difference scheme were outlined in [1]. A nine-point pattern is used: the surrounding points are placed at the center of six adjacent cells horizontally and two points vertically. Points at the corner of the calculation cells are implicitly used here. The finite-difference form of Eq. (9) is

$$\begin{aligned} & \frac{1}{H_R^2} \left( \sum_{j=1}^6 \tilde{X}_j - 6X_0^0 \right) + \frac{2}{H_Z^2} \left( \sum_{j=7}^8 \tilde{X}_j - 2X_0^0 \right) + \mu_0^2 X_0^0 + \frac{1}{16} \left( \sum_{j=1}^6 \tilde{X}'_j - 6\mu_0^2 X_0^0 \right) + \frac{1}{6} \left( \sum_{j=7}^8 \tilde{X}'_j - 2\mu_0^2 X_0^0 \right) + \\ & + \frac{1}{48} \sum_{j=1}^6 \frac{D_0^b (\mu_0^2 - \mu_j^2) X_0^0 + D_j^b (\mu_j^2 - \mu_0^2) X_j^0}{D_0^b + D_j^b + D_{j+1}^b} + \frac{1}{48} \sum_{j=1}^6 \frac{+ D_{j+1}^b (\mu_{j+1}^2 - \mu_0^2) X_{j+1}^0}{D_0^b + D_j^b + D_{j+1}^b} + \\ & + \frac{1}{12} \sum_{j=7}^8 \frac{D_0^b (\mu_0^2 - \mu_j^2) X_0^0 + D_j^b (\mu_j^2 - \mu_0^2) X_j^0}{D_0^b + D_j^b} + \frac{1}{X_0^0} \left( \frac{1}{8H_Z^2} + \frac{1}{6H_R^2} \right) \left( \sum_{j=1}^6 \tilde{X}_j - 6X_0^0 \right) \times \\ & \times \left( \sum_{j=7}^8 \tilde{X}_j - 2X_0^0 \right) + \frac{1}{H_R^2} \sum_{j=1}^6 (\Delta P_1^R)_j + \frac{2}{H_Z^2} \sum_{j=7}^8 (\Delta P_1^Z)_j = 0 \end{aligned} \quad (10)$$

under the assumption of spatial separability of the variables.

The conditions of continuity of the group fluxes and neutron fluxes are used in deriving Eq. (10). Therefore, the difference equations also include the values of the transient mode at the boundary of the calculation cell, which are grouped in the complexes  $\Delta P_1^R$ ,  $\Delta P_1^Z$ . The notation in Eq. (10) corresponds to Fig. 1

$$\begin{aligned} \tilde{X}_j &= \begin{cases} \frac{D_0^b X_0^0 + D_j^b X_j^0 + D_{j+1}^b X_{j+1}^0}{D_0^b + D_j^b + D_{j+1}^b}, & (j = 1, \dots, 6); \\ \frac{D_0^b X_0^0 + D_j^b X_j^0}{D_0^b + D_j^b}, & (j = 7, 8); \end{cases} \\ \tilde{X}'_j &= \begin{cases} \tilde{X}_j \frac{D_0^b \mu_0^2 + D_j^b \mu_j^2 + D_{j+1}^b \mu_{j+1}^2}{D_0^b + D_j^b + D_{j+1}^b}, & (j = 1, \dots, 6); \\ \tilde{X}_j \frac{D_0^b \mu_0^2 + D_j^b \mu_j^2}{D_0^b + D_j^b}, & (j = 7, 8). \end{cases} \end{aligned}$$

For the homogeneous region V, the finite-difference approximation in Eq. (10) is equivalent to the representation

$$\Delta_R \Phi = \frac{2}{3H_R^2} \left( \sum_{j=1}^6 \Phi_j^0 - 6\Phi_0^0 \right) - \frac{H_R^2}{16} \Delta_R^2 \Phi \quad (11)$$

for a problem in the horizontal plane, and

$$\Delta_Z \Phi = \frac{1}{H_Z^2} \left( \sum_{j=7}^8 \Phi_j^0 - 2\Phi_0^0 \right) - \frac{H_Z^2}{12} \Delta_Z^2 \Phi \quad (12)$$

for a problem in the vertical plane.



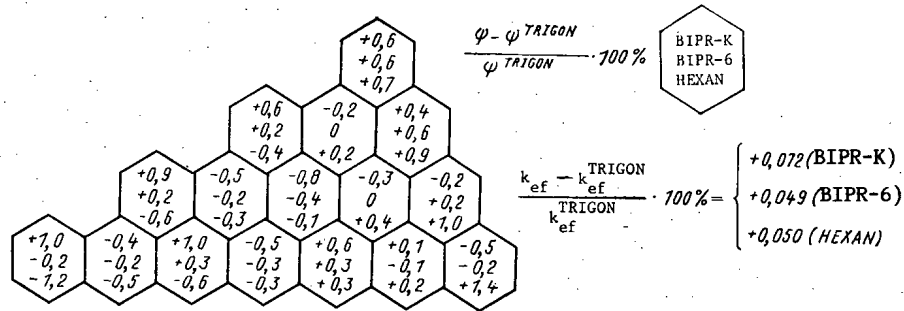


Fig. 3. Discrepancy between the fuel-assembly power  $\Psi$  obtained by a two-group calculation according to large-grid and fine-grid programs (TRIGON test).

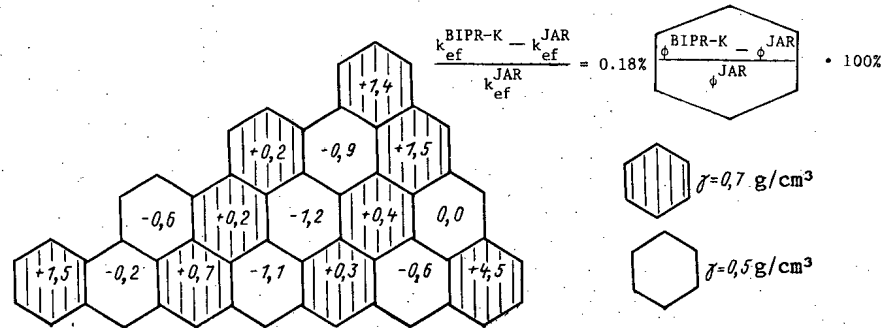


Fig. 4. Discrepancy of the fuel-assembly power  $\Psi$  obtained by the BIPR-K program and the fine-grid calculation program.

The second term on the right-hand side of Eqs. (11) and (12) characterizes the nonlinearity in the finite-difference representation of the differential operator. Thus, the use of points at the corners of the calculation cells allows these nonlinear corrections to be taken into account; they are significant in reactors with a large fuel assembly (VVER-1000 and AST-500, where  $H_R = 23-25$  cm).

In the BIPR-6 program [1] intended for calculating the VVER-1000 reactor, a finite-difference representation of the type in Eq. (10) with  $D^b = \text{const}$  is realized. If the influence of the transient mode on the group fluxes is neglected, Eq. (9) transforms to the equation for a group of decelerating neutrons

$$-\operatorname{div} D^b \operatorname{grad} \Phi^b + D^b \mu^2 \Phi^b = 0. \quad (13)$$

The single-group approximation is asymptotic. In the BIPR-5 program [2], Eq. (13) is solved with  $D^b = \text{const}$ . The nonlinear corrections to Eqs. (11) and (12) are neglected here; this is justified in VVER-440 calculations, where  $HR = 14.69$  cm.

Proceeding now to the solution of Eq. (6) for the transient mode, the solution according to Eq. (8) may be approximated by the following function for a problem in the vertical plane (plane geometry)

$$Y(x) = B_0^j e^{v_0(x - H_Z/2)} \quad (j = 7, 8). \quad (14)$$

The coordinate origin is at the center of the cell and  $B_j$  is the value of mode Y at the j-th end boundary of the cell.

for a problem in the horizontal plane (hexagonal geometry) in the BIRK-K program the corresponding Bessel-function approximation is used. Then the solution of Eq. (6) in the direction away from the center of the cell to the midpoint of each of the six lateral faces may be described by the function

$$Y(x) = \frac{B_0^j \sqrt{H_R/2}}{\sqrt{x}} e^{v_0(x-H_R/2)} \quad (j=1, \dots, 6), \quad (15)$$

where  $B_0^j$  is the value of mode Y at the j-th lateral face of the calculation cell.

A modal representation of the group fluxes is shown graphically in Fig. 2. This is equivalent to considering two halfspaces. It is obvious that

$$Y'(x)|_{x=H_\alpha/2} = v_0^* B_0^j \quad (j=1, 2, \dots, 8), \quad (16)$$

where

$$v_0^* = \begin{cases} v_0, & \alpha = Z; \\ v_0 - 1/H_R, & \alpha = R. \end{cases}$$

The following approximation is also used

$$X'(x)|_{x=H_\alpha/2} = \frac{A_0^j - X_0^0}{H_\alpha/2} \quad (\alpha = R, Z), \quad (17)$$

where  $A_0^j$  and  $X_0^0$  are the values of mode X at the j-th boundary and at the center of the cell, respectively.

Now using the continuity conditions for the group fluxes and the neutron fluxes at the boundary of cells 0 and j, an expression of the following type may be obtained

$$B_0^j = f(X_0^0, X_j^0, r_0, r_j, t_0, t_j, v_0^*, v_j^*, D_0^T, D_j^T, D_0^G, D_j^G, H_\alpha) \quad (18)$$

( $j=1, 2, \dots, 8; \alpha=R, Z$ ).

Thus, the transient mode Y uniquely determines the values of the asymptotic mode at two adjacent points according to Eqs. (14) and (15). It is obvious that, in this case, the mean value of mode Y over the cell is also uniquely determined by these values

$$\bar{Y} = \frac{v_0^*}{v_0^0} \left( \frac{2}{3H_R} \sum_{j=1}^6 B_0^j + \frac{1}{H_Z} \sum_{j=7}^8 B_0^j \right). \quad (19)$$

Turning now to the finite-difference Eq. (10) for the asymptotic mode X, it is solved using internal and external iterations. Here the terms  $\Delta P_1^R, \Delta P_1^Z$  including the values of the transient mode are assumed to be known at the stage of internal iteration. They are recalculated at the stage of external iterations on the basis of values of the asymptotic mode determined in the course of internal iteration.

The relations obtained show that this method allows the solution of the two-group system in Eq. (1) to be reduced to solving the single-group Eq. (9) for asymptotic mode X. This uniquely determines the transient mode Y in accordance with Eq. (18), and ultimately also the group fluxes  $\phi^b$  and  $\phi^T$ .

### Results

The possibility of using the algorithm of the BIPR-K program has been investigated by comparison with the results of fine-grid calculations by the program of [5-7] and the results of other large-grid programs [1, 2, 8].

Fine-grid calculations are conducted, as a rule, in the two-group approximation. This is intended to elucidate the scale of errors in the two-group calculation by the BIPR-K program which are related both with the use of a large grid and with the features of the solution of the two-group system of operations. The number of points of the two-dimensional (horizontal) fine grid is  $\sim 200-300$  for each fuel assembly, which corresponds to the size of the calculation grid in calculations of water-cooled, water-moderated and AST reactors on a fuel-element-by-fuel-element basis. Note that in practice the constraints associated with the computer memory capacity complicate the corresponding three-dimensional fine-grid calculations.

The results of two-group calculations for the TRIGON test problem [1], which is characteristic for water-cooled, water-moderated reactors (fuel-assembly lattice step  $H_R = 14.69$  cm with weak variation in the parameters  $D$  and  $M^2$  over the active zone), are shown in Fig. 3. The discrepancy between the results obtained by the BIPR-K program and by fine-grid calculations by the TRIGON program [5] is  $\sim 1\%$  for the energy liberation (power) of the fuel assembly and  $0.07\%$  for the  $k_{eff}$ . Approximately the same error in the fuel-assembly power is characteristic for the HEXAN [8] and BIPR-6 programs.

A series of test calculations has been performed, simulating the distribution of the moderator density over the active zone of the boiling-water-water reactor. A comparison with fine-grid calculations by the JAR program [6] is shown in Fig. 4 for one set of test results. In this case, homogeneous cells with a water density of  $0.5$  and  $0.7$  g/cm<sup>3</sup> are considered. The error in the fuel-assembly power is no greater than  $1.5\%$ . An exception is the peripheral fuel assembly, introducing three faces in the reflector, in which the power is overestimated by  $4.5\%$ . The error in determining  $k_{eff}$  is  $0.2\%$ .

Test loads for fuel assemblies with an extremely small moderator density of  $0.3$  g/cm<sup>3</sup> are also considered. In these cases, the error in calculating the fuel-assembly power by the BIPR-K program is  $3-4\%$ ; for fuel assemblies with three faces in the reflector, it may reach  $6\%$ . The error in determining  $k_{eff}$  in this case is  $0.8\%$  for a lattice step  $H_R = 18-25$  cm. The error in this case is obviously associated with the disruption of the condition in Eq. (8) with a small moderator density inside the fuel assembly. However it must be taken into account that, in real conditions, the mean moderator density over the calculation-cell cross section (taking account of the density of water in the gap between fuel assemblies) either does not reach such extremely small values or else is observed only over a small region in the upper part of the active zone, without introducing large errors in the mean fuel-assembly power.

A series of test problems is intended for the investigation of the influence of heterogeneous effects on the accuracy of calculations by the BIPR-K program. Heterogeneity of the calculation cells in their horizontal cross section is due primarily to the gap between the fuel assemblies, the water density in which may be significantly different from the density of the steam-water mixture inside the fuel assemblies, to the absorber clusters, and to the nonuniform fuel burnup. Test calculations show the possibility of using homogenized constants in the BIPR-K program, taking effective account of the presence of the gap by means of averaging over space and the neutron flux. The error in calculating the fuel-assembly power is no greater than  $3-4\%$ , and the error in  $k_{eff}$  is no more than  $0.2-0.3\%$ .

The region where the clusters are located in the fuel assemblies of VVER-1000 and AST-500 reactors corresponds approximately to subregion  $\Omega_0$  in Fig. 1. The properties of the central and peripheral parts of the fuel assembly on introducing the clusters are characterized by the breeder properties. Therefore, heterogeneous effects associated with the absorber clusters may be estimated using single-group calculations. The accurate calculation here is taken to be single-group fine-grid calculation, in which the central and peripheral parts of the fuel assembly with characteristic spread of the properties are distinguished. Test calculations show that the use of the corresponding homogenized constants allows the fuel-assembly power to be determined from the BIPR-K program with an error of  $\sim 5\%$  and  $k_{eff}$  to be determined with an error of  $0.2\%$ .

The algorithm of the BIPR-K program offers the fundamental possibility of assigning different properties to the central and peripheral parts of the calculation cell. It seems that the influence of the absorber clusters may be more correctly taken into account or non-uniform burnup of the fuel across the fuel assembly may be effectively taken into account by means of the corresponding calculation scheme.

It remains to thank A. N. Novikov for numerous fruitful discussions, L. K. Shishkov for useful comments, and E. V. Grishmanovskii and E. A. Zholkevich for assistance in performing the test calculations.

## LITERATURE CITED

1. A. A. Marakazov, Method of Calculating the Power of Cassettes for Water-Cooled, Water-Moderated Power Reactors in the Two-Group Diffusional Approximation [in Russian], Preprint IAÉ-2781, Institute of Atomic Power, Moscow (1977).
2. E. D. Belyaeva, I. L. Kireeva, and D. M. Petrunin, BIPR-5, a Program for Calculating the Energy-Liberation Fields and Fuel Burnup in a Single-Group Diffusional Approximation for Water-Cooled, Water-Moderated Power Reactors [in Russian], Preprint IAÉ-2518, Institute of Atomic Power, Moscow (1975).
3. E. Kaloinen, P. Siltanen, and R. Terasvirta, "Two-group modal calculations in hexagonal fuel assembly geometry," in: Proceedings of NFACRP Specialists' Meeting on Calculation of the Three-Dimensional Rating Distributions in Operating Reactors, Paris (1979).
4. N. Gupta, "Nodal methods for three-dimensional simulators," in: Progress in Nuclear Energy, Pergamon, London (1981).
5. E. Kaloinen, TRIGON, a Two-Dimensional Multigroup Diffusion Code for Trigonal or Hexagonal Mesh, Nuclear Engineering Laboratory, Technical Research Center, Finland (1973).
6. M. N. Zizin, L. K. Shishkov, and L. N. Yaroslavtseva, Test Neutron-Physics Calculations of Nuclear Reactors [in Russian], Atomizdat, Moscow (1980).
7. I. Vanichuk, Program for Solving Group Diffusional Equations in Hexagonal Geometry [in Russian], IYaI, Rzhesh (1982).
8. M. Makai and J. Arkuszewski, Trans. Am. Nucl. Soc., 38, 347 (1981).
9. M. Wagner and K. Koebke, Atomkernenerg., 43(2), 117 (1983).

#### TAKING ACCOUNT OF HEIGHT CONSTRAINTS IN PROBLEMS OF OPTIMIZING THE SPATIAL ENERGY DISTRIBUTION

N. A. Kuznetsov, P. T. Potapenko,  
G. N. Shelepin, O. L. Bozhenkov,  
and V. V. Mal'tsev

UDC 621.039.562.2

Recently, mathematical methods of the theory of linear programming have come to be widely used to solve problems of optimal control of the spatial energy distribution. The effectiveness of this approach has been confirmed by both experimental and theoretical data [1-5].

However, it is characteristic of a large part of the published work that the range of problems considered there is limited to problems of the optimization of radial-azimuthal energy distribution. At the same time, modern requirements of increased efficiency and safety of nuclear-reactor operation sharply pose the question of solving the problem of optimizing the parameters of the energy distribution over the whole volume of the active zone. One version of this approach was considered in [6], for the example of an algorithm of extremal regulation of the energy distribution in an RBMK reactor. Among the constraints of the problem, the condition of stabilization and elimination of skewing in the energy distribution over the height was taken into account.

In the present work, as the first step toward solving the problem of three-dimensional stabilization of the spatial energy distribution by mathematical-programming methods, a method is proposed for calculating the optimal displacements of the control rods (CR), on the basis of introducing into the simplex-method algorithm additional constraints, which are physically equivalent to the height constraints of [6] and also the corresponding modification of the criterion regarding the choice of column to be inserted in the basis.

---

Translated from Atomnaya Energiya, Vol. 59, No. 1, pp. 13-18, July, 1985. Original article submitted June 11, 1984.

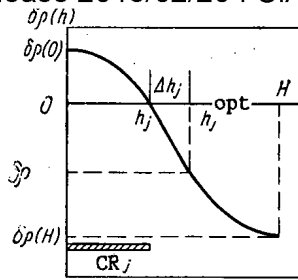


Fig. 1. Determining the boundary values of the reactivities  $\delta\rho_j(0)$  and  $\delta\rho_j(H)$  and optimal position  $h_j^{\text{opt}}$  with respect to the calibration characteristic of the  $CR_j$  as a function of its position in the active zone before beginning the optimizational calculation.

### Basic Assumptions

As a rule, operative control of the power distribution among the fuel channels in modern power reactors is accomplished by moving the CR. The radial energy distribution is usually controlled by this means, adding a leveled distribution over the channels with an identical burnup depth. The difficulty in controlling the axial power distribution by means of solid rods is that different movements and positions of the CR ends are required than in controlling the radial field. In this case, it is necessary to have a large number of rods immersed in the active zone to different depths or abbreviated rods introduced into the active zone from the top and the bottom [7].

Experience to date in solving optimization problems for the two-dimensional (radial-azimuthal) energy distribution permits the development of controlling programs that are able to function effectively in the real operating conditions of nuclear power units in terms of their basic indices [1-5]. Nevertheless, there remains a series of problems due to the conflicts in the required movements and positions of the CR ends to control the radial and height energy distributions. For example, if in the conditions of the two dimensional-optimization problem there are no constraints taking account of the integral effect of the optimal CR movements on the height energy distribution in any form, it is very probable that the optimal solution of the radial problem may prove to be unrealizable in practice because of conflict with the requirements on the form of the field over the height of the active zone. Therefore, it is of real practical interest at present to develop methods of solving the two-dimensional problem that would eliminate these deficiencies to some degree without significant increase in dimensionality of the optimization problem.

One possible version of this approach is now considered. In solving problems of optimizing the radial azimuthal energy distribution by linear-programming methods, the desired optimal solutions are usually the CR displacements  $\delta\rho_j^{\text{opt}}$  expressed in units of the reactivity. Regardless of the form of the target function and the physical formulation of the problem, the whole set of conditions here forms a system of linear relations with constant coefficients, which, as a rule, includes inequalities of two types [1-5]

$$y + a_{i1}\delta\rho_1 + \dots + a_{in}\delta\rho_n \leq b_i; \quad i = 1, \dots, m; \quad (1)$$

$$c_{k1}\delta\rho_1 + \dots + c_{kn}\delta\rho_n \leq d_k; \quad k = m+1, \dots, M, \quad (2)$$

where the variable  $y$  characterizes the value of the target function to be minimized (maximized), while the constants  $a_{ij}$ ,  $b_i$ ,  $c_{kj}$ ,  $d_k$  are determined by a theoretical-experimental method on the basis of physical laws reflecting the influence of the CR displacements  $\delta\rho_j$  ( $j = 1, \dots, n$ ) on the physical and thermal-engineering parameters of the active zone and the technological circuits of the energy unit. For example, in inequalities of the type in Eq. (2), to which constraints on the finiteness of the CR-displacement range of the following form reduce

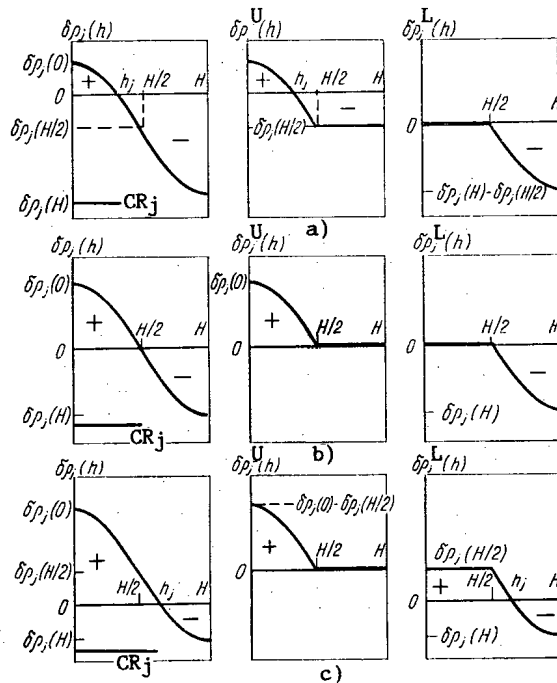


Fig. 2. Calibration characteristics of rods  $HR_j^U$  and  $HR_j^L$  as a function of the  $CR_j$  position in the active zone before the beginning of the optimizational calculation; a)  $CR_j$  in the upper half of the active zone; b)  $CR_j$  in the middle; c)  $CR_j$  in the lower half.

$$\alpha_j \leq \delta\rho_j \leq \beta_j, \quad j = 1, \dots, n, \quad (3)$$

the constant terms  $\alpha_j$  and  $\beta_j$  are determined from the calibration characteristics for the corresponding  $CR_j$ , and on the basis of Fig. 1 the following numerical values are adopted

$$\alpha_j = \delta\rho_j(H) \leq 0; \quad \beta_j = \delta\rho_j(0); \quad j = 1, \dots, n, \quad (4)$$

where  $\delta\rho_j(0)$  and  $\delta\rho_j(H)$  are the reactivities introduced by the  $j$ -th  $CR$  when it is moved (before the beginning of the optimizational calculation) to the completely withdrawn and completely immersed states, respectively;  $H$  is the maximum achievable immersion depth of the  $j$ -th  $CR$ , m. In ending the calculation, the required displacement  $\Delta h_j$  of each  $CR_j$  in the optimal position  $h_j^{\text{opt}}$  is recalculated on the basis of the values of  $\delta\rho_j^{\text{opt}}$  obtained in accordance with its calibration characteristic (Fig. 1).

In the initial formulation, depending on the type of functional relation between the technological parameters of the active zone and the desired variables of the radial problem  $\delta\rho_j$ , not all the constant terms  $b_i$  and  $d_k$  in Eqs. (1) and (2) are nonnegative. Therefore, in accordance with [8], a series of successive transformations is applied to Eqs. (1) and (2), including:

replacement of the variables  $\delta\rho_j$  ( $j = 1, \dots, n$ ) with no sign constraints by the nonnegative variables  $u_j = \delta\rho_j - \alpha_j \leq \beta_j - \alpha_j$  and the corresponding transformation of the right-hand side of Eqs. (1) and (2);

introducing nonnegative additional variables for transition from the inequalities in Eqs. (1) and (2) to equations;

transformation of the system of equations obtained to a system of equations with nonnegative right hand sides.

This sequence of transformations allows a canonical form of the linear-programming problem to be obtained with only one artificial variable. Then, applying any form of simplex algorithm, after a finite number of iterations of the computational process, the optimal solution  $\delta\rho^{\text{opt}} = [\delta\rho_1^{\text{opt}}, \delta\rho_2^{\text{opt}}, \dots, \delta\rho_n^{\text{opt}}]^T$  of the radial problem may be determined or incompatibility of its conditions may be established. The need for a priori determination of the first permissible basis solution is eliminated here.

The given scheme of solution for a two-dimensional problem, which has been tested in developing a program for calculating the optimal controlling perturbations (CR displacements) for the second-unit reactor of the I. V. Kurchatov Beloyarskii atomic power plant, has confirmed its effectiveness [4]. With slight variations, this method is also applicable to the solution of the radial problem, taking account of the integral action of optimal CR displacements in the height energy distribution.

#### Method of Solution

With spatial control of the reactor using CR, the regulation of the height distribution in basic conditions is of subordinate type and reduces, as a rule, to stabilization of the specified amplitude value of the first axial harmonic or a specified power relation between the upper and lower halves of the reactor [7, 8]. A definite compromise between the CR positions required for the radial and height distribution may be achieved if, in forming the height field, the optimal control of the radial-azimuthal energy distribution is such that the first axial harmonic is not excited. In the first approximation, this condition may be satisfied if a relation of the following form is added to the constraints on the radial problem (see [1-5], for example):

$$\left| \sum_{j=1}^n \delta\rho_j^U - \sum_{j=1}^n \delta\rho_j^L \right| \leq \varepsilon_\gamma, \quad (5)$$

where  $\delta\rho_j^U$  and  $\delta\rho_j^L$  are the reactivities introduced in the  $j$ -th CR in the upper and lower half of the reactor;  $\varepsilon_\gamma$  is a small positive number eliminating the degeneracy of the initial basis solution of the problem.

The use of the constraint in Eq. (5) means that the resulting displacement of the  $j$ -th CR  $\delta\rho_j$  in solving the radial problem must be expressed as a superposition of its displacements ( $\delta\rho_j^U + \delta\rho_j^L$ ) bounded by the limits of the upper and lower halves of the reactor, respectively, so that, as before, Eq. (3) must hold, that is

$$\alpha_j \leq (\delta\rho_j = \delta\rho_j^U + \delta\rho_j^L) \leq \beta_j; \quad j = 1, \dots, n, \quad (6)$$

where  $\alpha_j$  and  $\beta_j$ , as before, are determined in accordance with Eq. (4). To this end, each CR $_j$  is conventionally replaced by two rods HR $_j^U$  and HR $_j^L$ , the first of which may only be introduced from above in the active zone and the second from the middle. It is understood here that the range of displacement of each HR $_j$  is bounded by the limits of the upper and lower halves of the reactor, respectively. It is also assumed that the two HR $_j$  are positioned in the same channel as the corresponding CR $_j$ , while the resulting action of their combined displacement on the radial-azimuthal energy distribution is uniquely determined by the influence function and calibration characteristic of the CR $_j$ . Then the calibration characteristics of the HR $_j$  as a function of the depth of CR $_j$  immersion before beginning the optimizational calculation will appear as in Fig. 2. With choice of characteristics,  $\delta\rho_j(h) = \delta\rho_j^U(h) + \delta\rho_j^L(h)$ , and the sections with  $\delta\rho_j^U = \text{const}$  and  $\delta\rho_j^L = \text{const}$  correspond to zero efficiencies of the HR $_j^U$  and HR $_j^L$  outside the range of their displacement.

Introducing the pair of conventional rods HR $_j^U$  and HR $_j^L$  into consideration for each CR $_j$ , the possibility of formal replacement of the variable  $\delta\rho_j$  in Eqs. (1) and (2) by the sum of variables  $\delta\rho_j^U$  and  $\delta\rho_j^L$  appears, with subsequent representation of the initial conditions of the optimization problem in the form

$$y + a_{i1}(\delta\rho_1^U + \delta\rho_1^L) + \dots + a_{in}(\delta\rho_n^U + \delta\rho_n^L) \leq b_i; \quad (7)$$

$$c_{k1}(\delta\rho_1^U + \delta\rho_1^L) + \dots + c_{kn}(\delta\rho_n^U + \delta\rho_n^L) \leq d_k; \quad (8)$$

$$k = m+1, \dots, M.$$

The conditions in Eq. (2) which correspond to constraints of the type in Eq. (3) for the radial problem, taking account of the permissible range of HR<sub>j</sub> displacement ( $j = 1, \dots, n$ ), must be transformed to give

$$\alpha_j^U \leq \delta\rho_j^U \leq \beta_j^U; \quad (9)$$

$$\alpha_j^L \leq \delta\rho_j^L \leq \beta_j^L.$$

The constants  $\alpha_j^U, \alpha_j^L, \beta_j^U, \beta_j^L$  in Eq. (9), as before, are determined from the calibration characteristic of CR<sub>j</sub> as a function of its position before the beginning of the calculation. For example, if CR<sub>j</sub> is in the upper position of the active zone (Fig. 2a), then

$$\alpha_j^U = \delta\rho_j(H/2); \quad \alpha_j^L = \delta\rho_j(H) - \delta\rho_j(H/2); \quad (10)$$

$$\beta_j^U = \delta\rho_j(0); \quad \beta_j^L = 0.$$

In this case

$$\delta\rho_j(H) = \alpha_j = \alpha_j^U + \alpha_j^L \leq (\delta\rho_j = \delta\rho_j^L) \leq \beta_j^U + \beta_j^L = \beta_j = \delta\rho_j(0) \quad (11)$$

and Eq. (3) for the  $j$ -th CR of the radial problem is satisfied. It is readily evident that, in accordance with Fig. 2, Eq. (11) will be satisfied with any initial position of CR<sub>j</sub> within the limits of the active zone.

With formal replacement of the variable  $\delta\rho_j$  by the sum of variables  $\delta\rho_j^U + \delta\rho_j^L$ , Eqs. (7)-(9), as before, characterize a set of conditions of the radial problem in Eqs. (1) and (2), the only difference being that the number of variables is doubled. From the perspective of using the simplex method to solve the optimization problem with the set of constraints in Eqs. (7)-(9), the variables  $\delta\rho_j^U$  and  $\delta\rho_j^L$  are independent of one another. From a practical viewpoint, this means that the same value of  $\delta\rho_j^{\text{opt}}$  may be obtained with different combinations of values  $\delta\rho_j^U$  and  $\delta\rho_j^L$ . For example, in the optimal solution,  $\delta\rho_j^U$  and  $\delta\rho_j^L$  may take intermediate positions within the limits of the boundary values  $\alpha_j^U, \beta_j^U$  and  $\alpha_j^L, \beta_j^L$ . Then the same CR<sub>j</sub> must be simultaneously immersed partially in both the upper and lower halves of the reactor. It is obvious that, when using solid CR, this solution is impossible to realize in practice. Therefore, instead of the formal representation of the actual displacement of CR<sub>j</sub> as a superposition of the motion of the conventional rods HR<sub>j</sub><sup>U</sup> and HR<sub>j</sub><sup>L</sup>, it is necessary to impose a definite rule on the sequence of their displacements: rod HR<sub>j</sub><sup>L</sup> cannot begin to move within the limits of the lower half of the active zone until rod HR<sub>j</sub><sup>U</sup> reaches its lower boundary. Analogously if rod HR<sub>j</sub><sup>L</sup> is in the lower half, the position of HR<sub>j</sub><sup>U</sup> is fixed at the level of the middle of the active zone (lower limit of HR<sub>j</sub><sup>U</sup>) and cannot be changed until HR<sub>j</sub><sup>L</sup> reaches its upper limit. Hence it follows that if physically realizable optimal solutions are to be obtained, the rules governing the sequence of HR<sub>j</sub> displacements must be taken into account in the simplex-method algorithm. This is especially important in solving the radial problem, taking account of the height constraint in Eq. (5).

On the basis of which conditions may the HR<sub>j</sub> position be determined at any iteration of the computational process? It is known that the use of the simplex algorithm is possible if all the variables of the linear-programming problem are nonnegative. At the same time, it follows from Eqs. (4) and (9)-(11) that the variables  $\delta\rho_j^U$  and  $\delta\rho_j^L$  have no constraints on the sign. Therefore, following the above-described scheme of reducing the initial conditions of the optimization problem to the canonical form of the linear-programming problem, the new non-negative variables  $u_j^U$  and  $u_j^L$  are described, with the definitions



$$u_j^U = \delta \rho_j^U - \alpha_j^U; \quad u_j^L = \delta \rho_j^L - \alpha_j^L, \quad j = 1, \dots, n. \quad (12)$$

It is possible to rewrite Eq. (9) in the form

$$u_j^U \leq \beta_j^U - \alpha_j^U; \quad u_j^L \leq \beta_j^L - \alpha_j^L, \quad j = 1, \dots, n, \quad (13)$$

where for all  $j$

$$u_j^U \geq 0 \quad \text{и} \quad u_j^L \geq 0.$$

Replacing the variables  $\delta \rho_j^U$  and  $\delta \rho_j^L$  by  $u_j^U + \alpha_j^U$  and  $u_j^L + \alpha_j^L$ , respectively, in all the conditions in Eqs. (7) and (8) and transforming them as shown above, a canonical form of the linear-programming problem is obtained. The inequality in Eq. (13) may then take the form of an equation, with the following form

$$u_j^U + x_j^U = \beta_j^U - \alpha_j^U; \quad u_j^L + x_j^L = \beta_j^L - \alpha_j^L, \quad j = 1, \dots, n. \quad (14)$$

where  $x_j^U$  and  $x_j^L$  are additional nonnegative variables.

It follows from an analysis of Eq. (14) that, if in any iteration of the simplex algorithm the variable  $u_j^U = 0$  ( $u_j^L = 0$ ), i.e., falls outside the basis, then the corresponding HR $_j$  is at its lower boundary (completely immersed), according to Eq. (12). If  $x_j^U$  ( $x_j^L$ ) is not in the basis, however, i.e.,  $x_j^U = 0$  ( $x_j^L = 0$ ), it follows from Eqs. (14) and (12) that the corresponding HR $_j$  is at its upper limit (completely withdrawn). It is readily evident that, if both the variables  $u_j^U$  and  $x_j^U$  ( $u_j^L$  and  $x_j^L$ ) are nonzero (in the basis), the corresponding HR $_j$  takes an intermediate position within the limits of its range of displacement. Thus, from the presence or absence of the variables  $u_j^U$ ,  $x_j^U$ ,  $u_j^L$ ,  $x_j^L$  in the basis at each iteration of the computational process, the position of the HR $_j$  may be monitored within the limits of its range of displacement. This allows the logic of the simplex algorithm to be corrected in determining the current variable, which is introduced in the basis in such a way that the specified sequence of HR $_j$  displacements is not disrupted.

In accordance with simplex-method theory, each iteration is accompanied by successive transition from one basis solution to another (at the stage of determining the permissible basis solution) or from one permissible basis solution to another (at the stage of searching for an optimal plan) [9]. In both cases, this transition is associated with the replacement of one of the basis variables by a variable not belonging to the current basis. The criterion for choice of the variable to be introduced in the basis is a maximum (in modulus) negative value of the characteristic difference. Since the characteristic differences are calculated independently for all the independent variables, all the nonbasis variables are equally correct for introduction in the basis from the viewpoint of the usual simplex-algorithm scheme. Therefore, using this scheme cannot ensure the required sequence of HR displacements in the course of solving the optimization problem.

At the same time, in the given problem of optimizing the spatial energy distribution, the physical meaning of the successive transition from one basis to another by replacing a basis variable by a nonbasis variable is that, within the limits of a single iteration of the computational process, the position of only one of the rods HR $_j^U$ , HR $_j^L$  ( $j = 1, \dots, n$ ) may be changed. If it is also taken into account that the presence or absence of the variables  $u_j^U$ ,  $x_j^U$ ,  $u_j^L$ ,  $x_j^L$  ( $j = 1, \dots, n$ ) in the current basis may be used to unambiguously judge the position of any of the HR $_j$  before the beginning of each iteration of the simplex algorithm, the possibility of governing the sequence of HR displacements in the course of the whole computational process emerges.

This may be accomplished if the selection rule for the variable to be introduced into the basis is corrected as follows. From among the variables  $u_j^U$ ,  $x_j^U$ ,  $u_j^L$ ,  $x_j^L$  ( $j = 1, \dots, n$ ) not belonging to the current basis, a preliminary choice is made of those associated with the UR $_j$  for which the change in position in the next iteration is permissible in accordance with

the established rule. To this subset are added nonbasis variables unrelated to  $HR_j$ . Next, the usual selection rule for the variable to be introduced into the basis is applied to the set of nonbasis variables limited in this way, and the next iteration of the computational process is performed in complete agreement with the standard scheme of the simplex algorithm. Note that the method of preliminary selection of nonbasis variables here proposed is analogous to the method of simultaneous calculation of the characteristic differences or suboptimization, described in [10], in which successive solution of the optimization problem is performed with limited sets of nonbasis variables. The only difference here is that the selection criterion for the nonbasis variables is subject to a set rule of HR displacement.

The proposed method of solving the radial problem, taking account of the height constraint in Eq. (5), is also applicable, without any changes, in the case when each of the  $CR_j$  is replaced not by two but by a large number of HR with permissible displacement regions, uniformly distributed within the limits of each half of the active zone. The condition of nonexcitation of the first axial harmonic may be written here in the following form

$$\left| \gamma_i \left( \sum_{j=1}^n \delta \rho_{ij}^U - \sum_{j=1}^n \delta \rho_{ij}^L \right) + \dots + \gamma_i \left( \sum_{j=1}^n \delta \rho_{ij}^U - \sum_{j=1}^n \delta \rho_{ij}^L \right) \right| \leq \varepsilon_{\gamma}, \quad (15)$$

where  $\delta \rho_{ij}^U$  and  $\delta \rho_{ij}^L$  are the reactivities introduced by the  $j$ -th CR when it moves into the  $i$ -th region of the upper and lower halves of the reactor;  $\gamma_i$  is a weighting factor characterizing the influence of  $CR_j$  displacement within the limits of the  $i$ -th region of each half of the active zone on the amplitude of the first axial harmonic.

Note, in conclusion, that optimization problems may be solved by the proposed method not only in the case when all the CR are introduced in the active zone only from above and below but also when rods are introduced both from above and from below. If sectioned liquid or gas control units with independently variable liquid-column height or absorber density are used to control the spatial energy distribution [7], no changes in the logic of the standard simplex algorithm are required to take account of height constraints of the type in Eq. (5) or Eq. (15) and the optimal-control problem is solved in the usual manner.

### Practical Results

The effectiveness of the optimizing program written in accordance with the method proposed for selecting the variable to be introduced in the basis has been preliminarily tested on the basis of comparing the results of solving the radial problem without the constraint in Eq. (5) in the formulation published in [4] in the usual manner and also when account is taken of the replacement of each of the  $CR_j$  ( $j = 1, \dots, n$ ) by a pair of conventional rods  $HR_j^U$  and  $HR_j^L$  with a prescribed sequence of displacements. The results of the comparison show that the optimal solutions obtained in the two cases are identical. After testing, a program for calculating the optimal displacements of the control rods was developed on the basis of the above-described method of taking height constraints of the type in Eq. (5) into account and introduced into experimental-commercial use at the second-unit reactor of the I. V. Kurchatov Beloyarskii atomic power plant. Calculations performed at this plant confirm the effectiveness of the given algorithm and show that it is sufficiently efficient.

### LITERATURE CITED

1. I. Ya. Emel'yanov, V. G. Nazaryan, and V. V. Postnikov, "Optimizing the energy distribution in the active zone of a large operational power reactor," *At. Energ.*, **44**, No. 4, 310-315 (1978).
2. A. A. Anikin and Ya. V. Shevelev, "Formulation and methods of computer solution of the problem of controlling the heat-liberation field in RBMK-type reactors," *Vopr. At. Nauki Tekh.*, Ser. Fiz. Tekh. Yad. Reakt., No. 3(12), 35-47 (1980).
3. A. A. Anikin, V. P. Gorbunov, and Ya. V. Shevelev, "Some problems of the operative control of the energy-liberation field of large power reactors," in: *Atomic Power Stations* [in Russian], Atomizdat, Moscow (1980), pp. 130-136.
4. O. L. Bozhenkov, V. G. Dunaev, N. A. Kuznetsov, et al., "Controlling the energy distribution of the second-unit reactor at the Beloyarskii atomic power plant," *At. Energ.*, **15**, No. 2, 91-96 (1981).
5. A. M. Afanas'ev, "Calculating the optimal energy distribution in the reactor," *At. Energ.*, **54**, No. 5, 368-370 (1983).

6. I. Ia. Lamei yarov, V. V. Fushnikov, and G. V. Iurkin, "Algorithm of extremal regulation of the energy distribution in a power reactor," *At. Energ.*, **47**, No. 1, 8-12 (1979).
7. E. V. Filipchuk, P. T. Potapenko, and V. V. Postnikov, *Controlling the Neutron Field of a Nuclear Reactor* [in Russian], Energoizdat, Moscow (1981).
8. P. T. Potapenko, "Harmonic regulation of the power of an energy reactor," *At. Energ.*, **50**, No. 1, 8-15 (1981).
9. S. I. Gass, *Linear Programming*, McGraw-Hill, New York (1975).
10. L. S. Lesdon, *Optimizing Large Systems* [Russian translation], Nauka, Moscow (1975).

## RECONSTRUCTION OF THE FIELDS OF PHYSICAL QUANTITIES IN RBMK

A. D. Zhirnov, V. D. Nikitin,  
A. P. Sirotkin, and V. P. Shaposhnikov

UDC 621.039.51

The determination of the fields of physical quantities, such as the neutron flux density and the capture or fission cross sections, is one of the most important problems which are solved for purposes of monitoring the power of fuel channels (FC). Experience in operating RBMK shows that for a "fresh" active zone the neutron-physical calculation using the BOKR program [1, 2] gives results which are in satisfactory agreement with the measurements ( $\sigma = 8\%$ ). With time, however, the disagreement increases, which lowers the quality of the monitoring. A gradual increase in the error of the neutron-physical calculation is basically a consequence of the accumulation of errors in determining the instantaneous values of the nuclide composition and other characteristic affecting the macroscopic constants.

At the present time there exist many methods for reconstructing the energy-release field based on data produced by neutron-physical calculations and the indicators of intrareactor monitoring sensors [3-5]. It is shown in [3, 6] that good reconstruction is achieved when the microstructure of the resulting field is close to the computed structure, while the macrostructure corresponds to the indicators of the intrareactor monitoring sensors. This principle was used and developed in subsequent works. Thus, for example, algorithms of the PRIZMA program, which enable the determination of the energy-release field in RBMK based on a neutron-physical calculation and indications of intrareactor monitoring sensors using the method of statistical interpolation, are described in the monographs [1, 7]. One method for reconstructing the energy-release field while simultaneously adjusting the starting data for the neutron-physical calculation is proposed in [5].

In this paper we propose a new approach to the determination of the fields of physical quantities in a reactor and the correction of starting data for the neutron-physical calculation. Unlike the method in [5], the problem is solved here in two stages. First the neutron flux density field is reconstructed by fitting the computed data to the indications of the intrareactor monitoring sensors. The macroconstants in the neutron-physical calculation are then corrected in order to decrease the methodical error of the calculation to a level determined by the model used. In so doing, the neutron flux density fields over the reactor are doubly differentiated, which dictates the requirements that the reconstruction of fields must be of high quality and the fields and their derivatives up to and including second order must be continuous.

Since the neutron-physical calculation describes well the microstructure of actual fields the ratio of the actual field to the computed field is a function  $U(x, y)$  which varies slowly over an area of several cells of the reactor. Its variation over the active zone can be significant. At the locations of the sensors the function is known with some error. The problem of reconstructing the field can be reduced to the selection of a method for extrapolating the function  $U(x, y)$  over the entire reactor.

Such a function must, of course, be smooth, slowly varying, and close to its known values at the locations of the sensors. The smoothness and slow variation will be guaran-

---

Translated from *Atomnaya Energiya*, Vol. 59, No. 1, pp. 18-21, July, 1985. Original article submitted June 25, 1984.

$$K = \int_S \left[ \left( \frac{\partial^2 U}{\partial x^2} \right)^2 + \left( \frac{\partial^2 U}{\partial y^2} \right)^2 \right] dS, \quad (1)$$

where  $S$  is a region encompassing the entire cell of the reactor including the reflector, the coordinates  $x$  and  $y$  are dimensionless.

As a measure of the deviation of the function  $U(x, y)$  from the function  $Q(x, y)$ , representing the ratio of the measured values of the field to the computed values, we used the integral

$$R = \int_S \rho (U - Q)^2 dS, \quad (2)$$

where  $\rho(x, y)$  is a weight function which is chosen to be 0 in regions free of sensors and inversely proportional to the variance of the indications of sensors at their locations:

$$\rho = \sum_k \frac{D}{D_k} F_k \delta(r - r_k), \quad k = 1, \dots, N, \quad (3)$$

where  $D$  and  $D_k$  are the average variance and the variance at the point  $r_k$ ;  $F_k$ , area of some region referring to the sensor, for example, the area of the cell; and  $N$ , number of sensors.

We now introduce the functional

$$I = K + \alpha R, \quad (4)$$

where  $\alpha > 0$  is some coefficient characterizing the contribution of the integral  $R$  to the functional  $I$ . The value of  $\alpha$  can be chosen only in practice. Minimization of the functional  $I$  permits finding the function  $U(x, y)$  with whose help some compromise will be made between the requirement that the functional  $K(I)$  be minimized and the requirement that the function  $U$  be close to the values of  $Q$ .

The requirement that the variations of the functional  $I$  vanish leads to the equation

$$\frac{\partial^4 U}{\partial x^4} + \frac{\partial^4 U}{\partial y^4} + \alpha \rho (U - Q) = 0 \quad (5)$$

and the boundary conditions

$$\begin{aligned} \frac{\partial^3 U}{\partial y^3} \tau_x - \frac{\partial^3 U}{\partial x^3} \tau_y - \frac{\partial}{\partial l} \left[ \left( \frac{\partial^2 U}{\partial x^2} - \frac{\partial^2 U}{\partial y^2} \right) \tau_x \tau_y \right] &= 0; \\ \frac{\partial^2 U}{\partial x^2} \tau_y^2 + \frac{\partial^2 U}{\partial y^2} \tau_x^2 &= 0, \end{aligned} \quad (6)$$

where  $\partial/\partial l$  indicates differentiation along the line of the boundary enclosing the region of integration  $S$ ;  $\tau_x$  and  $\tau_y$  are the components of the unit vector tangent to the boundary line. This equation together with the indicated boundary conditions is quite complicated and is solved in practice by numerical methods.

We shall denote the partial derivatives below by  $U_x$ ,  $U_{xx}$ ,  $U_y$  etc.

The sum of the fourth-order derivatives of the function  $U(x, y)$  in Eq. (5) on a five-point grid is approximated by a difference approximation using  $U_x$  and  $U_y$  which has proven itself well in practical calculations:

$$-U^{i,j-1} + \frac{h}{2} (U_x^{i+1,j} - U_x^{i-1,j} + U_y^{i,j+1} - U_y^{i,j-1})], \quad (7)$$

where the difference approximation on a three-point grid is used for the first derivatives of the function  $U(x, y)$ :

$$U_x^{i,j} = \frac{3}{4h} (U^{i+1,j} - U^{i-1,j}) - \frac{1}{4} (U_x^{i+1,j} + U_x^{i-1,j});$$

$$U_y^{i,j} = \frac{3}{4h} (U^{i,j+1} - U^{i,j-1}) - \frac{1}{4} (U_y^{i,j+1} - U_y^{i,j-1}). \quad (8)$$

In this case the difference analog of the differential equation (5) can be written in the form

$$h^2 \hat{L}U + \alpha \rho^{i,j} (U^{i,j} - Q^{i,j}) = 0, \quad (9)$$

where  $\rho^{i,j}$ , according to (3), has the following form:

$$\rho^{i,j} = \begin{cases} h^2 \frac{D}{D^{i,j}} & \text{in a cell containing a sensor} \\ & \text{with variance } D^{i,j}, \\ 0 & \text{in cells without sensors.} \end{cases}$$

The most natural grid step for RBMK is  $h = 25$  cm, i.e., one computed point for the correction function for each reactor cell. However, an even sparser grid can be used with a step equal to a multiple of 25 cm. The grid can even be rotated by an angle of  $45^\circ$ . For cells which do not fall on the nodes of the sparse grid, the values of the correction function can be obtained by interpolation based on the nearest four nodes of the grid at which the values of the function and its first derivatives are known. The following expression is proposed for the interpolation formula:

$$U(x,y) = U^{i,j} \Phi(\xi) \Phi(\eta) + U^{i+1,j} \Phi(1-\xi) \Phi(\eta) + U^{i,j+1} \Phi(\xi) \Phi(1-\eta) +$$

$$+ U^{i+1,j+1} \Phi(1-\xi) \Phi(1-\eta) + h U_x^{i,j} \Psi(\xi) \Phi(\eta) - h U_x^{i+1,j} \Psi(1-\xi) \Phi(\eta) +$$

$$+ h U_x^{i,j+1} \Psi(\xi) \Phi(1-\eta) - h U_x^{i+1,j+1} \Psi(1-\xi) \Phi(1-\eta) + h U_y^{i,j} \Phi(\xi) \Psi(\eta) -$$

$$- h U_y^{i,j+1} \Phi(\xi) \Psi(1-\eta) + h U_y^{i+1,j} \Phi(1-\xi) \Psi(\eta) - h U_y^{i+1,j+1} \Phi(1-\xi) \Psi(1-\eta), \quad (10)$$

where  $\xi = (x - x^i)/h$ ,  $\eta = (y - y^j)/h$ , and  $x$  and  $y$  are coordinates of the interpolation points within the intervals  $(x^i, x^{i+1})$  and  $(y^j, y^{j+1})$ , respectively. The functions  $\Phi$  and  $\Psi$  defined in the interval  $(0, 1)$  are cubic polynomials:

$$\Phi(\xi) = (1 + 2\xi)(1 - \xi)^2;$$

$$\Psi(\xi) = \xi(1 - \xi)^2. \quad (11)$$

Thus the equations (9) with the difference approximation (7) and the interpolation formula (10) enable finding an approximate solution of Eq. (5). In the case of "absolutely accurate" sensors ( $\alpha \rightarrow \infty$ ), located at each node of the grid, including the boundary, this solution is a two-dimensional spline [8].

The algorithm described above was implemented on a BESM-6 computer in the form of the COMEX programmed module as part of the DACOR complex, intended for correcting the neutron-physical constants for two-dimensional calculations of the reactor. The computational time depends on the parameter  $\alpha$ . For  $\alpha \gg 1$ , which corresponds to absolutely accurate sensors ( $U = Q$ ), and a computational grid with a step of  $h = 25$  cm the processor time is equal to 4-6 min. For a sparse grid with a step of  $h = 100$  cm the computational time is about 10 sec.

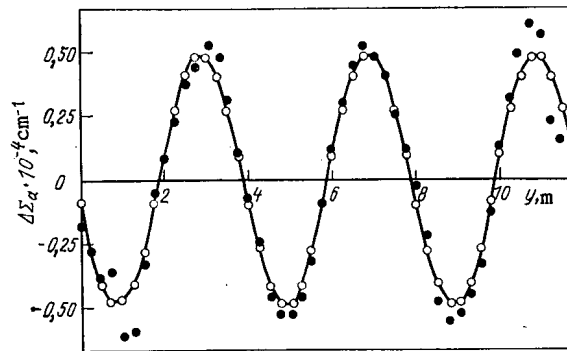


Fig. 1. Introduced (○) and reconstructed (●) perturbations of the absorption macroscopic cross section.

The value  $\alpha = 0.04$ , for which the disagreement between the computed values of  $U$  and the values of  $Q$  at the locations of the sensors is equal to  $\sim \sqrt{D}$ , was selected by trial and error. The processor time in this case was two times longer than the case  $\alpha \gg 1$ .

The algorithm includes a block for automatic rejection of sensors according to the condition

$$|U^{i,j} - Q^{i,j}| > 2.5 \sqrt{D^{i,j}}, \quad (12)$$

where  $D^{i,j}$  is the variance of the corresponding sensor.

The correction function  $U(x, y)$  found is multiplied by the computed neutron flux density field at all points of the working grid. The field obtained, which has the required micro- and macrostructure, is used for determining the corrections to the absorption cross sections at all computational points of the reactor with the help of the diffusion equations.

To evaluate the quality of the reconstruction of the fields and the correction of the neutron-physical constants, a computational study was performed in which for some state of the reactor sinusoidally distributed disturbances with an amplitude of approximately 4% were introduced into the starting absorption cross sections. The neutron flux density field of the perturbed neutron-physical calculation was then processed using the proposed procedure in the approximation of absolutely accurate sensors. The values of the neutron flux density of the unperturbed neutron-physical calculation at 130 points were used as the sensor indications.

In order to characterize the deviation of the field with the perturbed cross sections from the starting field, we calculated the variance of the deviations, i.e., the mean-square differences of the values of the neutron flux density for the perturbed and unperturbed distributions. The variance was calculated for the reconstructed field also. The calculations show that for a grid with a step  $h = 25$  cm the variance of the reconstructed field is approximately  $10^4$  times smaller than the variance of the perturbed field, and in the case when the grid step is  $h = 100$  cm and the interpolation formula (10) is used the variance of the reconstructed field is  $10^3$  times smaller than the variance of the perturbed field.

The quality of the correction of the absorption cross sections can be judged by how well the corrections to their values, introduced during the reconstruction process, correspond to the perturbations introduced. The circles in Fig. 1, connected for visual clarity by the solid line, show the values of the perturbations  $\Delta \Sigma_a$  along the  $Oy$  axis (the perturbations along the  $Ox$  axis are identical), while the dots indicate the corrections to the absorption cross sections for a typical series of channels. After the correction is introduced, the norm of the residual disturbance was equal to about 0.3 of the norm of the introduced disturbance, and the rms error of the reconstructed field in this case is equal to 0.4%.

To evaluate the quality of the proposed reconstruction of the fields in the case of an irregular perturbation, we performed a series of calculations in which random uncorrelated perturbations ("white noise") with a variance of  $10\%^2$  were introduced into the starting absorption cross section of each cell in the active zone. The rms deviations from the unper-

Declassified and Approved For Release 2013/02/20 : CIA-RDP10-02196R000300070001-4  
turbid field were equal to 15-20%, which approximately corresponds to the values observed in practice. Then an error with a variance of  $10\%^2$  was introduced into 130 values of the neutron flux density of the unperturbed neutron-physical calculation (sensor indications). After reconstructing the field with  $\alpha = 0.04$  based on the indicated sensor indications, the rms deviation of the reconstructed field from the unperturbed field decreased to 3.5-3.7%.

Although the problem of exact reconstruction of a single realization of white noise in the starting data based on the indications of 130 sensors cannot be solved, it nevertheless is of definite interest for characterizing the possibilities of the method under extreme conditions. It turned out that the "reconstructed" white noise - comparatively smooth with a characteristic scale of the order of the distance between the sensors and with a small admixture of high-frequency components of the function - is, according to the norm, approximately five times smaller than the perturbation introduced; the correction of the cross section decreases the norm of the perturbation insignificantly (by 1.5%).

To check the method, real states of the reactor in the first block of the Kursk nuclear power plant on May 27 and June 9 and 17, 1980 were calculated. Each of 130 sensors used for radial monitoring was selected as the control sensor and using the proposed procedure the expected indication of the control sensor was found based on the actual indications of the remaining sensors. Analysis of the expected and actual indications gave an rms reconstruction error of 3.9, 4.1, and 4.1%, respectively, for states on the indicated days.

Taking into account the correction obtained from the actual indications of sensors on May 27 in the neutron-physical calculation on June 17 decreased the variance between the results of the calculation and the sensor indications on June 17 from  $270\%^2$  to  $36\%^2$ . We note that over this period the state of the active zone changed due to overloads, during which the fuel cells were replaced by nonfuel cells and vice versa.

The calculation of the corrections to the absorption cross section for real states of RBMK showed that the rms value of the correction over the active zone is equal to 0.5-1.0% of the absorption cross section of the fuel cell, which is consistent with the a priori information on the accuracy of the constants.

Comparison of the proposed algorithm with the method of statistical interpolation (maximum likelihood) can be made based on [3, 4], where the problem of reconstructing fields for real states of the Beloyarsk and Bilibinsk nuclear power plants is solved. In these studies the variance of the reconstructed fields is equal to  $16\%^2$  and  $16-21\%^2$ , respectively. It is evident from the comparison that the proposed method is no worse than the method of statistical interpolation, though in principle the latter must be more accurate. In order to make full use of the possibilities of the indicated method, however, very accurate mathematical expectation and correlation functions must be obtained. For RBMK which have large and strongly heterogeneous active zone and operate in a continuous overload mode, the latter require substantial computer calculations.

Thus the algorithm developed enables reconstructing the energy-release and neutron flux fields with very high accuracy. In addition, the accuracy of the neutron-physical calculation can be increased by taking into account the errors, which cannot be controlled by different means, in the determination of characteristics of all components of the active zone. In the proposed method these errors, which in part also include the methodical error of the neutron-physical calculation, refer to the absorption cross section. The resulting corrections to the absorption cross section can be used in calculations of subsequent states of the reactor over some period of time.

The proposed algorithm can be used as a supplement to the existing algorithm in the centralized control system. At the level of nonoperational calculations, the algorithm can be used to calibrate separate sensors, determine the temperature fields, etc. A variant of the algorithm with a sparse difference grid and the interpolation formula (10) can be implemented and efficiently used on class SM minicomputers.

#### LITERATURE CITED

1. N. A. Dollezhal' and I. Ya. Emel'yanov, Channel Nuclear Power Reactor [in Russian], Atomizdat, Moscow (1980).
2. I. Ya. Emel'yanov, M. B. Egiazarov, V. I. Ryabov, et al., "Physical startup of the RBMK reactor in the second block of the Leningrad V. I. Lenin Nuclear Power Plant," At. Energ., 40, No. 2, 127-132 (1976).

5. I. S. Akimov and R. A. Zemtsova, Vopr. At. Nauki Tekh., Ser. Fiz. Tekh. Yad. Reaktorov, No. 1(23), 13 (1982).
6. I. Ya. Emel'yanov, B. G. Dubovskii, Yu. V. Evdokimov, et al. "Monitoring energy-release fields based on the relative efficiency of control rods," At. Energ., 30, No. 5, 422-427 (1971).
7. E. V. Filipchuk, P. T. Potapenko, and V. V. Postnikov, Control of the Neutron Field of a Nuclear Reactor [in Russian], Énergoizdat, Moscow (1981).
8. Yu. I. Mikhalevich and O. K. Omel'chenko, "Procedures for piecewise-polynomial interpolation of a function in one of two variables," Computational Center, Siberian Branch, Academy of Science of the USSR, Novosibirsk (1970).

#### COMPLEX RADIATION MONITORING OF THE FUEL DISTRIBUTION IN VIBRATION-PACKED FUEL ELEMENTS

L. I. Kosarev, N. R. Kuzelev,  
A. N. Maiorov, A. S. Shtan',  
and V. M. Yumashev

UDC 620.179.15:621.039.546

One of the most important stages in the manufacture of fuel elements is monitoring the fuel distribution. At the present time, for monitoring fuel elements with vibration-packed mixed fuel, facilities are used which measure the density distribution of the fuel mixture and the mass of plutonium over the length of the fuel element [1-3]. In addition to these characteristics, the fuel distribution over the cross sections of the fuel element is interesting, and which is estimated very approximately [1, 4].

Procedure for Monitoring the Fuel Distribution. The complex monitoring of the distribution of vibration-packed mixed fuel is carried out expediently using an apparatus based on a combination of several radiation methods [2, 3]. The  $\gamma$ -absorption method is used for determining the density of the fuel mixture and its distribution over the length of the fuel element. In order to monitor the distribution of plutonium, passive  $\gamma$ -scanning is used. Computer tomography allows the fuel distribution over the cross sections of the fuel element to be investigated. The joint use of these methods gives the possibility of increasing the accuracy of the measurements of the required fuel-element characteristics, of using the smallest assembly of equipment, and of achieving a high degree of its unification.

The procedure for monitoring the distribution of vibration-packed fuel over the length of the fuel element, based on the combination of the  $\gamma$ -absorption method and passive  $\gamma$ -scanning, has been developed and used for the prereactor analysis of fast reactor fuel elements [5]. A metrological guarantee of the method and the monitoring equipment has been created for this case.

With the simultaneous use of three radiation methods, the tomographic investigation of the transverse sections of the fuel element is carried out advantageously at the position of measurement of the density. The measurement scheme is shown in Fig. 1. The computer tomography principle is based on recording the radiation passing through a layer of the fuel element, with repeated relative movements of the fuel element and the radiation source-detector system, with subsequent data processing on a computer according to a defined algorithm. The mathematical methods for processing the data are described in detail in [6]. In this case, the method of filtered inverse projections [7] was used, effected by the following expression

$$\mu(x, y) \rho(x, y) = \frac{1}{2\pi^2} \int_0^\pi p^*(r, \varphi) d\varphi, \quad (1)$$

---

Translated from Atomnaya Énergiya, Vol. 59, No. 1, pp. 22-27, July, 1985. Original article submitted August 13, 1984.



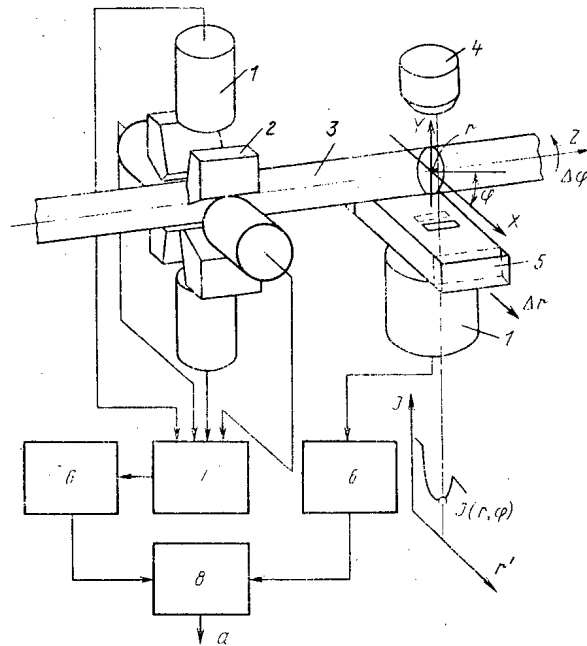


Fig. 1. Measurement scheme for the complex radiation monitoring of the distribution of vibration-packed fuel: 1) detector unit; 2) intrinsic radiation collimator; 3) fuel element; 4) radiation head with radioactive source; 5) collimator for radiation from external source; 6) signal processing unit; 7) summation device; 8) SM-4 computer;  $\Delta\varphi$ , angle of rotation of the fuel element;  $\Delta r$ , pitch of the movement of the fuel element;  $a$ , output to the printer of data about the density distribution of the fuel, mass of plutonium, and the tomograms.

where  $\mu(x, y)$  is the mass attenuation coefficient for an element of the layer with coordinates  $x, y$ ;  $\rho(x, y)$  is the density of this element of the layer;  $p^*(r, \varphi)$  is a filtered projection, calculated as the convolution of the projection  $p(r, \varphi)$  with the filter function  $A(r)$ :

$$p^*(r, \varphi) = \int_{-R}^R p(r', \varphi) A(r - r') dr'. \quad (2)$$

Here

$$p(r, \varphi) = -\ln \frac{I(r, \varphi)}{I_0}, \quad (3)$$

where  $I(r, \varphi)$  is the intensity of the radiation passing through the fuel element, measured at the point with coordinates  $r, \varphi$ ;  $I_0$  is the intensity of the radiation recorded in the absence of the fuel element. The tomogram obtained represents the matrix  $\{\mu(x, y)\rho(x, y)\}$ , uniquely defining the distribution of the fuel over the cross section of the fuel element.

**Modeling of the Monitoring Process on the Computer.** In order to obtain the characteristics being monitored with a high accuracy, it is necessary to investigate the effect of non-stable parameters for both the fuel element itself and for the measurement system. In carrying out the parametric analysis of the monitoring process, the output characteristics of the measurement system and the errors caused by the influencing factors were determined. The model was defined with nominal parameters of the fuel element and of the measurement system. The errors were calculated [8] for the case of indirect measurements:

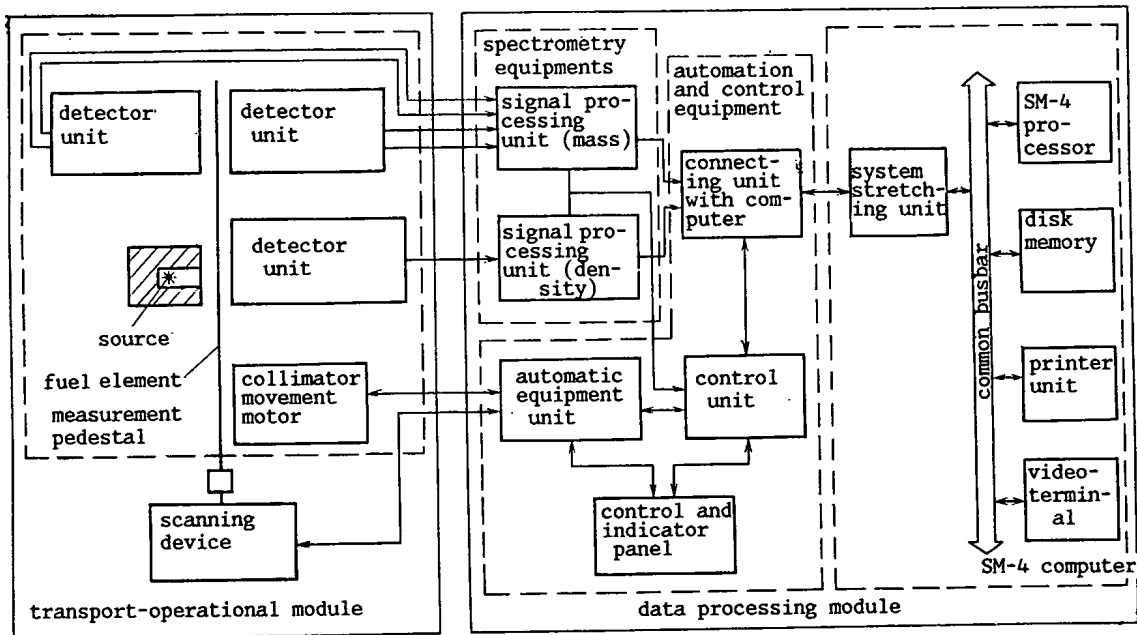


Fig. 2. Structural diagram of the apparatus.

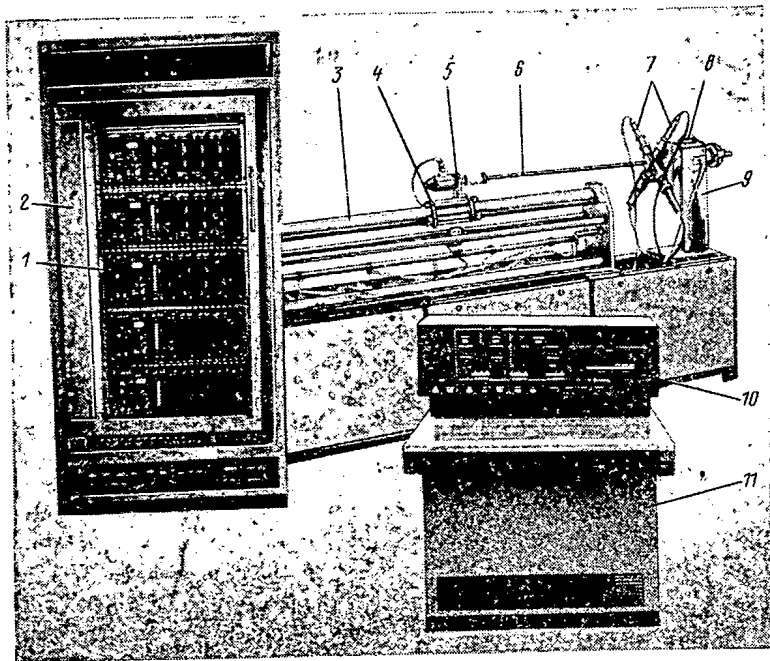


Fig. 3. General view of the MNMG-1M apparatus: 1) spectrometric channel; 2) cabinet for processing units; 3) scanning equipment; 4) motor for moving the fuel element; 5) motor for rotating the fuel element; 6) fuel element; 7) detector unit; 8) radiation head; 9) measurement pedestal; 10, 11) operator's console and desk.

$$S_{\theta} = \sqrt{\sum_{i=1}^N \left( \frac{\partial \theta}{\partial T} S_T \right)^2}, \quad (4)$$

where  $\theta$  is the result of the measurements;  $T$ , parameter of the process;  $S_{\theta}$  and  $S_T$ , mean square deviations of the measurement result and the parameter.

The measurement result is expressed in the form

$$\theta = \bar{\theta} \pm 2S_{\theta}, \quad (5)$$

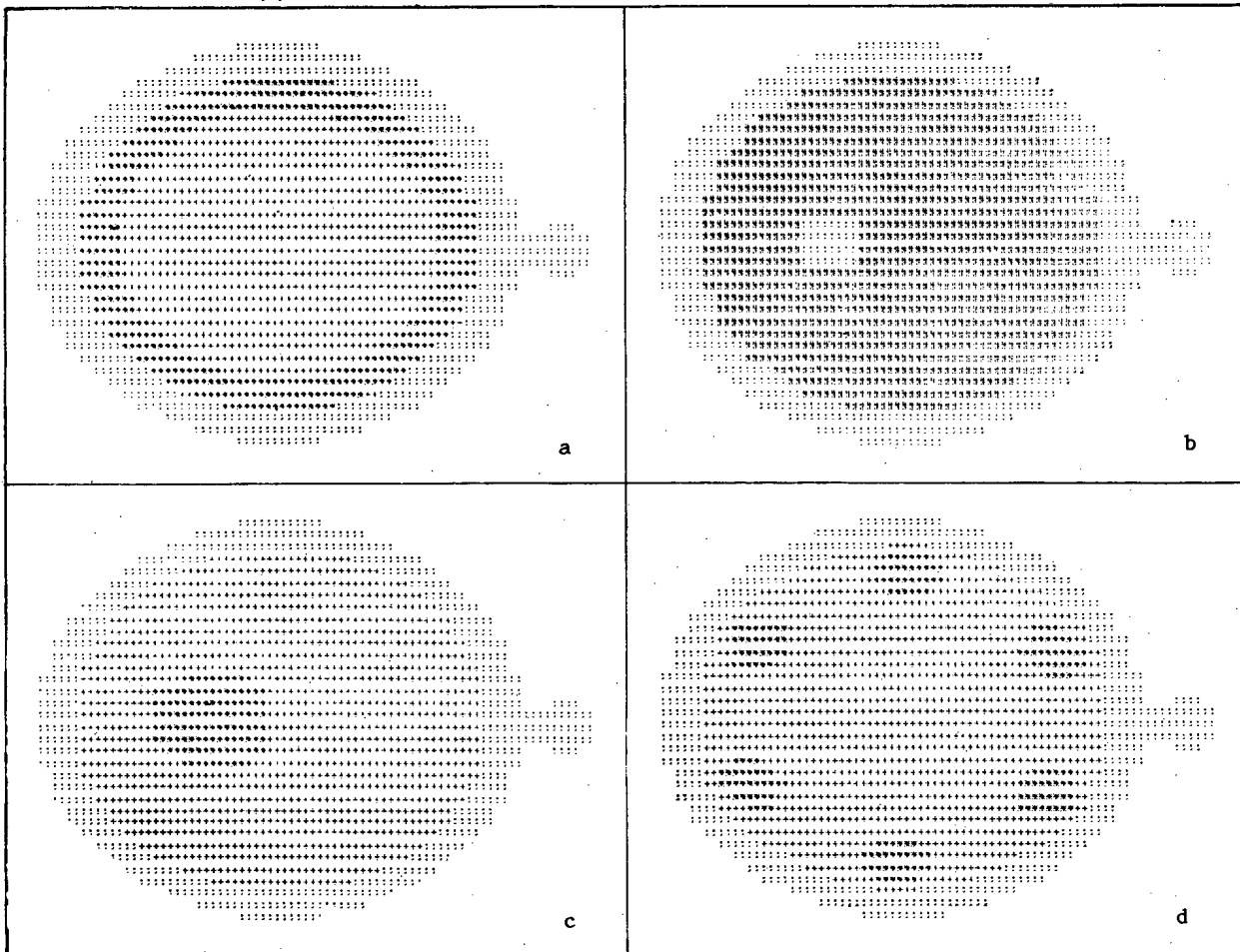


Fig. 4. Tomograms of a fuel-element rod with a different fuel distribution in the core: a) 10% annular thickening with a width of 0.8D; b) 10% local thickening with a diameter of 0.3D; c) air cavity with a diameter of 0.15D; d) six accumulations of plutonium with a diameter of 0.15D.

where  $\bar{\epsilon}$  is the average value of the result (output characteristic for a nominal value of the parameters). All the results were determined with a confidence coefficient of 0.95.

For example, the model of the density measurement is based on the relation describing the interaction of the  $\gamma$  radiation from the external source with the material of elementary volumes of the layer of the fuel element being monitored, and the intensity of the radiation passing through the layer with the specified characteristics is determined. From the values of the intensity, the error of the density measurement, caused by a change of the parameters of the monitoring process, is found.

The errors in the density measurement, caused by variations of the diameter and thickness of the fuel-element cladding, fluctuations of the nuclide composition of the fuel, and the inaccuracy of locating the fuel element at the measurement position, were investigated by the method described. The results of the investigations showed that the change of diameter and the inaccuracy of locating the fuel element had the strongest effect on the error; however, in the case of fluctuations of these factors within the permissible limits, the error of the density measurement should not exceed 1.5%. An analysis of the results enabled the optimum range of the collimator width to be determined (0.7-0.9 of the diameter of the fuel element), for which the errors of the density measurements are minimal.

In addition, the errors in the density measurement, caused by the nonuniform distribution of the fuel over the transverse cross section of the fuel element, were analyzed. The distribution cannot be completely uniform, in consequence of the final size and nonsphericity of the fuel particles and existence of pores and regions with an increased content of plutonium [1, 2]. The following cases of nonuniform fuel distribution were analyzed: annular zones of different density and width, local zones of increased density, and air gaps. It

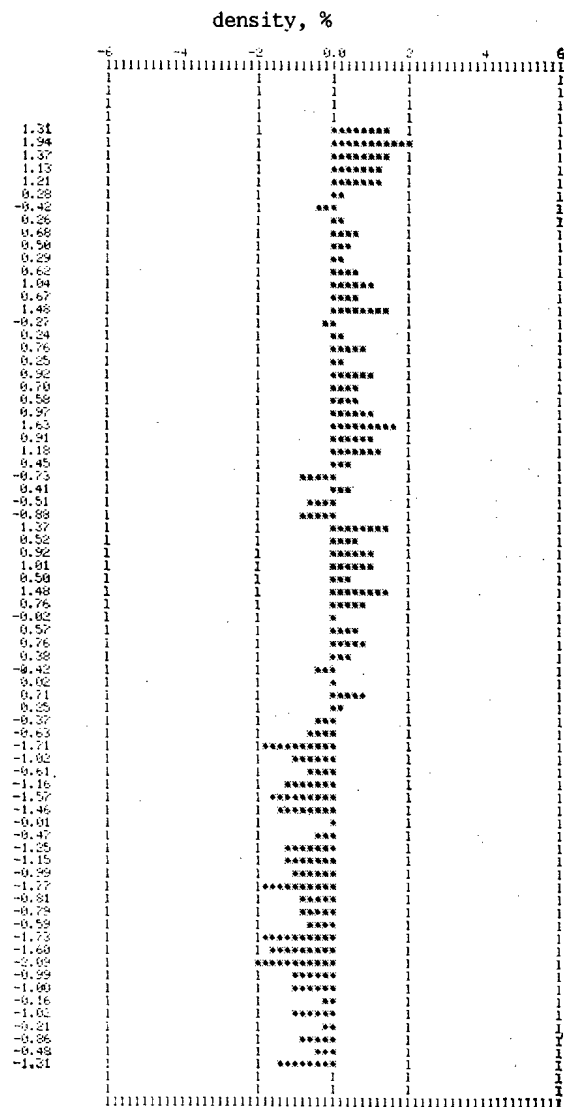


Fig. 5. Results of monitoring the density distribution of vibration packed fuel along the length of a fuel-element rod.

TABLE 1. Results of the Density Measurement of a Special Fuel-Element Sample

Parameter	Number of section			
	1	2	3	4
$\bar{\rho}$ , g/cm <sup>3</sup>	8,52	8,78	8,86	9,05
$\Delta$ , %	0,7	0,7	0,7	0,8
$\Delta$ , %	1,2	0,9	0,8	0,9

wa established that with the presence in the layer of an annular zone with a width of more than 0.1D (D is the diameter of the core), with a density increased by 5% or an air pore with a diameter greater than 0.1D, the error in the density determination exceeds 0.5%, and this effect must be taken into consideration.

Modeling of the tomograph process on the computer showed that the cases of nonuniform distribution of the fuel considered can be detected even with the use of the <sup>137</sup>Cs "hard" radiation. The modeling results were used in order to choose the principal technical characteristics of the monitoring apparatus.

Apparatus for Monitoring the Plutonium Distribution. The MNMG-1M equipment, designed for monitoring fuel element rods with vibration-packed fuel, is constructed on the basis of the module-orientated design principle and includes a transport-operational module and a data processing module. This apparatus operates in conjunction with a minicomputer of the SM-4 type (Figs. 2 and 3).

The transport-operation module is intended for conducting measurements during the movement of the fuel element, and also for its location and fixing. The module is a horizontal frame structure with a length of ~5 m and contains the measurement pedestal, the device for scanning the fuel element and a loading and unloading channel (not shown in the figure). The radiation head and the five detector units are installed in the measurement pedestal. A  $\gamma$ -radiation source based on  $^{137}\text{Cs}$  and detector scintillation units with NaI(Tl) crystals are used. The drive motor for moving the collimator perpendicular to the axis of the fuel element is installed in the pedestal.

The scanning device incorporates the motor for the step movement of the fuel element longitudinally and for rotating it to a specified angle. All the motors are unified and made on the basis of the use of a screw-nut drive, and also a step motor with a small ( $1.5^\circ$ ) rotation step. This solution ensures a high accuracy of the mechanical movements of the fuel element and simplicity of control by the motors.

Processing of the detector signals, control of the operation of the transport-operative module and linking of the apparatus with the computer are effected with the data processing module, providing automatic operation of the whole equipment assembly. The data processing module includes the signal processing units, the operator's console, and the step motor control units.

Five spectrometric channels are provided in the signal processing units. The control, indicator, and automatic equipment units, computer link units, and the power supply units are located in the operator's console.

An SM-4 minicomputer is used for the collection and storage of information, its digital processing and extraction of the results on a display and printout equipment. In addition, it performs the separate control functions and monitors the efficiency of the whole complex. The program assurance assembly performs calibration of the apparatus, input of data to the computer during measurements, provision of the density and mass distributions of plutonium over the length of the fuel element and tomograms of the diametrical layers, and also certification of the results.

During monitoring, the fuel element is placed on the carriage and moved into the measurement pedestal. One of the detectors records the intensity of the  $^{137}\text{Cs}$  radiation passing through the fuel element, and four detectors measure the natural radiation of the plutonium. The signals from the detectors are fed to the spectrometric channels for separation of useful data and background signals. After this, the signals are fed to the counters of the control unit, whence they are transferred to the computer for processing. The intensity measurements are conducted in succession, in the intervals between the step movements. Before each measurement, the fuel element is rotated by a defined angle, in order that the spacing wire on the fuel element cladding is outside of the radiation beam. For the tomography, one of the zones of the fuel element is automatically installed at the density monitoring position between the radiation head and the detector unit. The measurements of the intensity of the radiation passing through this zone are conducted in succession between the step rotations of the fuel element. After each complete rotation of the fuel element, the collimator is moved by one step. All the measurements are recorded in the computer memory and then processed.

The apparatus functions in three regimes: fuel density monitoring, fuel density and plutonium mass monitoring, and tomographic monitoring. The principal technical characteristics of the apparatus are given below.

Time of measurements in the regime, min:

fuel density monitoring	$\leq 5$
fuel density and plutonium mass monitoring	$< 120$
tomographic monitoring	4-30
Step of movement of fuel element, mm	2.5, 5.0, 10.0

Step of movement of collimator, mm	0.3, 0.6, 0.9
External radiation source	<sup>137</sup> Cs, IGI-Ts-4
γ-Radiation detectors	NaI(Tl), BDÉG-2-22, 6931-17
Maximum permissible error, %	
for fuel density measurement	≤ 2
for plutonium mass measurement	≤ 2
Maximum size of tomogram	62 × 62 elements
Maximum size of tomogram element, mm	0.15

Results of Experimental Investigations. During investigation and production tests, the technical characteristics of the apparatus were determined. In the first stage, the errors in operating the motors of the transport-operational module were established. As a result, it was found that the error in the step of the movement of the fuel element does not exceed 0.5% and the error in locating the fuel element relative to the radiation beam is not more than 0.1 mm. A special fuel-element sample, having several sections with a different density, was used for the metrological certification of the MNMG-1M apparatus. Values of the density were determined by means of a certified mass of fuel and of the volume of part of the core. The error in the density measurement amounted to ±0.4%. The density of each zone was determined by means of five series of measurements of 30 measurements in each. The results and the measurement errors are shown in Table 1, where  $\rho$  is the average value of the density for the section;  $\lambda$  is the random component of the measurement error, and  $\Delta$  is the measurement error. The values of the random component of the error were determined with a confidence coefficient of 0.95. In all the experiments, the principal measurement error of the density did not exceed 2%. Monitoring of a batch of fuel elements showed that the duplication of the results of measurement of the average density is not more than 0.6%.

In the tomographic investigation regime, tomograms of the fuel distribution over individual cross sections of the fuel element were obtained (Fig. 4). Layers with local thickening and air pores are shown in Fig. 4b, c. The feasibility of determining zones with an increased content of plutonium is illustrated in Fig. 4d. The core and cladding of the fuel element are clearly distinguished in all the tomograms, and also the spacing wire can be seen. As an illustration of the capability of the apparatus, Fig. 5 shows the fuel density distribution along the length of the vibration-packed core of a fuel-element rod.

Conclusions. The monitoring procedure, based on the combined use of a number of radiation methods, gives the possibility of obtaining complete information about the distribution of fuel materials in a fuel element. It is expedient to use the γ-absorption method in conjunction with passive gamma-scanning and computer tomography.

Parametric modeling of the monitoring process on a computer allows the characteristics of the monitoring apparatus to be optimized, and its errors to be analyzed.

The MNMG-1M apparatus can be used for monitoring the distribution of vibration-packed fuel in fuel-element rods at both the stage of development and research and also in the conditions of their commercial production.

#### LITERATURE CITED

1. V. V. Gorskii, "Nondestructive monitoring of the content of fissile materials and gadolinium in fuel elements," *At. Tekh. Rubzhom*, No. 9, 3-9 (1983).
2. V. S. Baklanov, G. Yu. Besednev, G. I. Gadzhiev, et al., *Automated Facility for the Technological Monitoring of the Mixed Fuel Distribution in Fuel Elements AKORT-2*; [in Russian], Preprint Scientific-Research Institute of Nuclear Reactors-10(525), Dimitrovgrad (1982), p. 15.
3. A. K. Gorobets, Yu. I. Leshenko, and A. L. Semenov, *Measurement of the Distribution of Plutonium in Fuel Elements by the Gamma-Scanning Method* [in Russian], Preprint Scientific-Research Institute of Nuclear Reactors-7(522), Dimitrovgrad, p. 16 (1982).
4. W. Winn, "A gamma-ray monitor for plutonium uniformity in fuel tubes," *Nucl. Instrum. Methods*, **193**, No. 10, 251-255 (1982).
5. G. I. Gadzhiev, Yu. I. Leshchenko, A. K. Gorobets, et al., "Monitoring the Distribution of Plutonium in Unirradiated Fuel Elements with Vibration-Packed Mixed Fuel," *Problems of Nuclear Science and Technology, Series Physics and Technology of Nuclear Reactors* [in Russian], Issue 3(40) (1984), pp. 11-16; G. I. Gadzhiev, A. K. Gorobets, and A.

- L. Semenov, "Technological Monitoring of Fuel Elements for the Quality of the Distribution in Them of Uranium-Plutonium Fuel," Problems of Nuclear Science and Technology, Series Physics and Technology of Nuclear Reactors [in Russian], Issue 3(40) (1984), pp. 16-18.
6. G. Herman, Image Restoration by Projections. Principles of Reconstructural Tomography [Russian translation], Mir, Moscow (1983).
  7. É. Yu. Vasil'eva, L. I. Kosarev, N. R. Kuzelez, et al., "Radiation computer tomography of spherical fuel elements," At. Energ., 56, No. 6, 400-405 (1984).
  8. G. D. Burdun and B. N. Markov, Principles of Metrology [in Russian], Standartov, Moscow (1972).

## A STUDY OF THE HIGH-TEMPERATURE CREEP IN COARSE-GRAINED URANIUM DIOXIDE

A. A. Gridnev, D. N. Dzalandinov,  
P. V. Zubarev, and A. S. Panov

UDC 620.1.173.25

There have been a number of publications [1-3] on the effect of grain size on the steady-state (secondary) creep rate of uranium dioxide at elevated temperatures. At the present time, it is considered that at temperatures above  $0.5T_{mp}$  the creep rate of coarse-grained materials does not depend on grain size. This has been experimentally established for Cu and Al [4], LiF [5], ZrC [6], and  $UO_2$  [3]. We note that all the creep studies on uranium dioxide were carried out on the specimens having a grain size of 5-50  $\mu m$ . The aim of the present work is to study creep of uranium dioxide having a grain size of the order of a few hundred to a few thousand microns over a wide temperature and stress range.

We used specimens of coarse-grained uranium dioxide virtually corresponding to the stoichiometric composition ( $O/U \approx 1.9999$ ) and consisting of elongated grains measuring 150-250  $\mu m$  in diameter and 500-3500  $\mu m$  in length produced by recondensation [7] (Fig. 1).

During the tests, the load was applied both in the directions parallel and perpendicular to the grain texture  $\langle 111 \rangle$ . The density of the specimens was found to be 81-99% of the theoretical value. For the purpose of comparison, tests were carried out on the fine-grained (5-10  $\mu m$ ) and the stoichiometric ( $O/U \approx 2.0001$ ) uranium dioxide having a 96-98% theoretical density.

We determined the accumulation of plastic deformation during creep using the compression method under a vacuum of  $2 \cdot 10^{-3}$  Pa on a 1246-R unit. The test temperature was maintained in the 1770-2170°K range, the stress range was 5-40 MPa, and the specimens measured 8 mm in diameter and 16 mm in height. Specimen deformation was measured using a KM-6 cathetometer. Temperature was monitored using tungsten-rhenium thermocouples and an OPPIR-017 optical pyrometer.

Figure 2 illustrates typical creep curves of the coarse grained uranium dioxide (having different porosity values) obtained at 1920°K at a stress of 10 MPa. We note the presence of an intermittent stage of the nonsteady-state creep (up to  $\sim 2$  h).

From the data presented in Fig. 2 and the results of our studies, we may conclude that increasing the porosity up to 13-19% leads to an increase in the creep rate by more than 30 times without affecting the nature of the  $\dot{\epsilon}(\sigma, T)$  relationship. We note that, in the present context, the term "porosity" means a set of structural characteristics of the materials such as the total porosity, open and closed porosity, pore size and shape, pore distribution etc. In view of this, any description of the porosity dependence of properties is only an approximation because of the impossibility of evaluating (presenting) these characteristics with sufficient accuracy. In the given case, the steady-state creep rate is a power function of the porosity (P):  $\dot{\epsilon} \sim PP$ , where  $p \sim 1.9$ , or  $\dot{\epsilon} \sim (1-P)^{-q}$ , where  $q \approx 22.8$ . On the other hand, it was noted [1] that in the case of fine-grained uranium dioxide, a change in porosity from 2.8 up to 5.5% has virtually no effect on the creep rate.

---

Translated from Atomnaya Énergiya, Vol. 59, No. 1, pp. 27-29, July, 1985. Original article submitted March 16, 1984.



Fig. 1. Microstructure of uranium dioxide with nonequiaxial coarse grains.

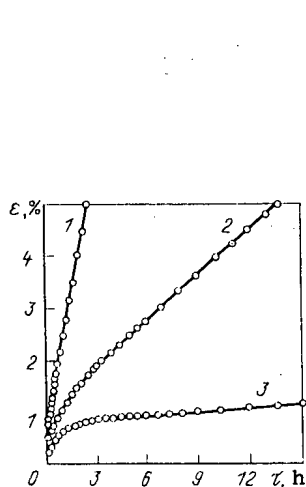


Fig. 2

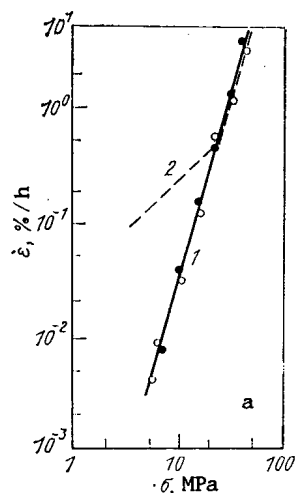


Fig. 3

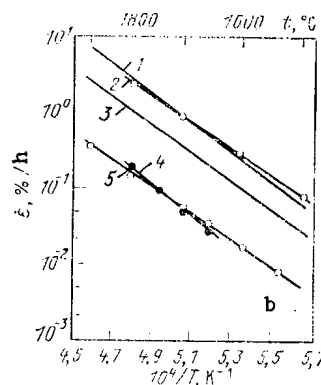


Fig. 2. Creep curves of the coarse-grained uranium dioxide at a stress of 10 MPa and a temperature of 1920°K. Density, % theoretical value: 1) from 81 up to 87; 2) from 91 up to 92; 3) from 94 up to 99.

Fig. 3. Dependence of steady-state creep rate of uranium dioxide on stress at 1920°K (a): ○) loading perpendicular to the texture  $\langle 111 \rangle$ ,  $d = 150-250 \mu\text{m}$ ; ●) loading parallel to the texture  $\langle 111 \rangle$ ,  $d = 500-3500 \mu\text{m}$ ; ---)  $d = 5-10 \mu\text{m}$ , and on temperature (b): 1, 2)  $d$  is equal to 5-10 and 150-250  $\mu\text{m}$ , respectively, at  $\sigma = 20 \text{ MPa}$ ; 3, 4, 5)  $d$  is equal to 5-10, 500-3500, and 150-250  $\mu\text{m}$ , respectively, at  $\sigma = 10 \text{ MPa}$ .

Figure 3a shows the stress dependence of creep rate at 1920°K. In the entire stress range under study (5-40 MPa) the steady-state creep rate follows the law  $\dot{\epsilon} \sim \sigma^{4.2}$ , i.e., the material creeps according to the dislocation-diffusion mechanism. This conclusion is further confirmed by the fact that a change in the grain size in the 150-3500  $\mu\text{m}$  range does not affect the creep rate. Testing the specimens with load application along the texture  $\langle 111 \rangle$  and perpendicular to it changes the effective grain size from 500-3500 up to 150-250



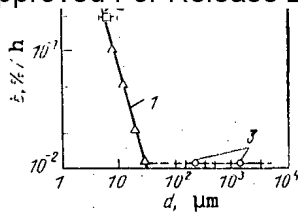


Fig. 4

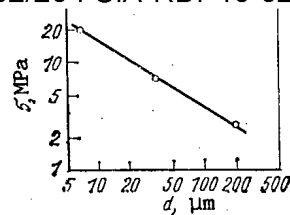


Fig. 5

Fig. 4. Dependence of the steady-state creep rate of uranium dioxide under compression on the grain size at a temperature of 1920°K and a stress of 7 MPa: 1) experimental data [1] (grain size up to 35 μm); 2)  $d = 5-10 \mu\text{m}$ ; 3)  $\text{UO}_2$  with coarse elongated grains.

Fig. 5. Grain-size dependence of the linear creep limit of  $\text{UO}_2$  at 1920°K.

μm, but shows virtually identical steady-state creep rate values (curve 1, Fig. 3a). For the purpose of comparison, the stress dependence of the steady-state creep rate of a fine-grained uranium dioxide having a grain size of 5-10 μm is also shown. In this case, at stresses below the linear creep limit ( $\sigma < 20 \text{ MPa}$ ), the creep rate is directly proportion to the stress ( $\dot{\epsilon} \sim \sigma^{1.0}$ ) indicating that creep occurs according to the Nabarro-Herring vacancy-diffusion mechanism.

Using the grain size dependence of the linear creep limit  $\sigma_c \sim d^{-[2/(h-1)]}$  [1], we obtain  $\sigma_c \approx 2.6 \text{ MPa}$  for uranium dioxide having  $d_{av} \approx 200 \mu\text{m}$  at a temperature of 1920°K. According to our evaluation, the steady-state creep rate at such a stress amounts to  $\sim 10^{-4} \text{ %/h}$ .

Figure 3b shows the temperature dependence of the steady-state creep rate at the stress levels of 10 and 20 MPa. We note that in the 1920-2170°K range the creep rates of uranium dioxide having elongated grains of different orientations virtually coincide (curves 4 and 5, Fig. 3b), i.e., grain size and orientation do not affect the steady-state creep rate. In the case of the uranium dioxide specimens having coarse elongated grains with the  $\langle 111 \rangle$  texture perpendicular to the direction of load application, the computed value of the activation energy for creep amounts to  $410 \pm 10 \text{ kJ/mole}$ ; and when the  $\langle 111 \rangle$  texture coincides with the direction of load application, it amounts to  $456 \pm 12 \text{ kJ/mole}$ . For the fine-grained uranium dioxide specimens this value is equal to  $426 \pm 10 \text{ kJ/mole}$ . The obtained values (410-456 kJ/mole) virtually coincide with the activation energy for self-diffusion of uranium in uranium dioxide (426-450 kJ/mole) [8], indicating that the creep processes are controlled by the self-diffusion processes of uranium in uranium dioxide.

Based on the obtained experimental data, the dependence of the steady-state creep rate of the coarse-grained uranium dioxide specimens having elongated grains on temperature and stress can be presented in the following form:

$$\dot{\epsilon} = A\sigma^{4.2} \exp(-440000/RT),$$

where  $\dot{\epsilon}$  is the steady-state creep rate, %/h;  $A$  is a coefficient;  $\sigma$  is the applied stress ranging from 5 up to 40 MPa;  $R$  is the gas constant, J/(mole·°K); and  $T$  is the temperature ranging from 1770 up to 2170°K.

It is seen from Fig. 3a that in the region where the vacancy-diffusion mechanism operates, the creep rate varies according to the law  $\dot{\epsilon} \sim d^{-2}$ , i.e. it is inversely proportional to the square of the grain size (we note that there are experimental data [2] according to which  $\dot{\epsilon} \sim d^{-1.5}$ ), and in the region where the dislocation-diffusion mechanism operates, the creep rate is clearly independent of the grain size. Figure 4 shows the grain size dependence of the steady-state creep rate of uranium dioxide at a temperature of 1920°K and a stress of 7 MPa. In the case of the uranium dioxide specimens having a grain size up to 35 μm, we observe a well-defined dependence  $\dot{\epsilon} \sim d^{-2}$ . The experimental point for the fine-

grained uranium dioxide (with  $d = 5-10 \mu\text{m}$ ) is located close to it. Finally, the data obtained on the coarse-grained uranium dioxide having elongated grains (curve 3) indicate that there is no effect of grain size on the creep rate. Thus, after attaining certain grain size, the high-temperature creep rate of uranium dioxide and numerous other materials [9] does not depend on grain size.

On examining Fig. 4, it can be seen that the stress level of 7 MPa corresponds to the linear creep limit of  $\text{UO}_2$  having  $d \approx 35 \mu\text{m}$ . Using the experimental data on the linear creep limit of  $\text{UO}_2$  having  $d_{\text{av}} \approx 7 \mu\text{m}$  ( $\sigma_c \approx 20 \text{ MPa}$ ) and the calculated value of  $\sigma_c$  for  $\text{UO}_2$  having  $d_{\text{av}} \approx 200 \mu\text{m}$  ( $\sigma_c \approx 2.6 \text{ MPa}$ ), one can plot the grain size dependence of the linear creep limit of  $\text{UO}_2$  at  $1920^\circ\text{K}$  (Fig. 5). This dependence is described by the equation  $\sigma_c = Kd^{-0.61}$ . The vacancy-diffusion creep mechanism operates in the region below the curve  $\sigma_c = f(d)$ , and the dislocation-diffusion creep mechanism operates in the region above the curve.

#### LITERATURE CITED

1. M. Seltzer, J. Perrin, A. Clauer, and B. Wilcox, "A review of creep behavior of ceramic nuclear fuels," *Reactor Technol.*, **14**, No. 2, 99-135 (1971).
2. A. Solomon, C. Yust, and N. Packan, "Primary creep of  $\text{UO}_2$  and the effect of amorphous grain boundary," *J. Nucl. Mater.*, **110**, No. 3, 333-342 (1982).
3. F. Mohamed and M. Soliman, "On the creep behavior of uranium dioxide," *Mater. Sci. Eng.*, **53**, No. 2, 185-190 (1982).
4. F. Mohamed, "Analysis of creep data on copper at very low stresses," *ibid.*, **40**, No. 1, 101-104 (1979).
5. T. Langdon, "The variation in secondary creep rate at large grain sizes," *Scripta Met.*, **4**, No. 9, 693-695 (1970).
6. L. N. Dement'ev, P. V. Zubarev, L. B. Nezhevenko, and V. I. Groshev, "Effect of grain size on the high-temperature creep of zirconium carbide," *Fiz. Met. Metalloved.*, **39**, No. 3, 578-584 (1975).
7. A. A. Gridnev, "Method of manufacturing tubular ceramic products," *Inventor's Certificate No. 891590*, *Byull. Izobret.*, No. 47 (1981).
8. G. B. Fedorov and E. A. Smirnov, *Diffusion in Reactor Materials* [in Russian], Atomizdat, Moscow (1978).
9. Zh. P. Puar'e, *High-Temperature Plasticity of Crystalline Bodies* [in Russian], Metallurgiya, Moscow (1982).

#### CALCULATION OF THE DISPLACEMENT PEAKS IN THE CONTINUUM APPROXIMATION

V. P. Zhukov and A. V. Demidov

UDC 621.039.531.001.57

In describing the later stages in the evolution of atomic-collision cascades in irradiated materials (displacement peaks, DP), the use of the gas-dynamic problem of perturbation of a continuous medium on account of instantaneous local energy liberation equal to the energy of the primarily ejected atom (PEA) was proposed in [1]. In the case of this approximate approach, DP evolution may be described by a standard system of gas-dynamic equations, which usually has a solution of spherical-shock-wave type with specified boundary and initial conditions [2]. A method of numerical modeling of DP in the gas-dynamic approach is described below, together with the results obtained. It is assumed in the calculation that the radiation damage is completely localized in the DP, and the losses in electronic excitation are extremely small. Both these conditions limit the maximum achievable PEA energy: in the case of light elements, the energy  $E_0$  must be below the characteristic energy of DP formation, amounting to approximately a few keV; in the case of heavy elements it must be below the excitation energy, approximately equal to a few tens of keV [3]; the minimum value of  $E_0$  is equal to the threshold displacement energy  $E_d$ .

The following variables are introduced for the construction of the mathematical model:  $u$  is the velocity of particles of the material;  $r$  is the ordinary Euler coordinate;  $p$ ,  $\rho$ ,

Translated from *Atomnaya Energiya*, Vol. 59, No. 1, pp. 29-33, July, 1985. Original article submitted May 24, 1984.

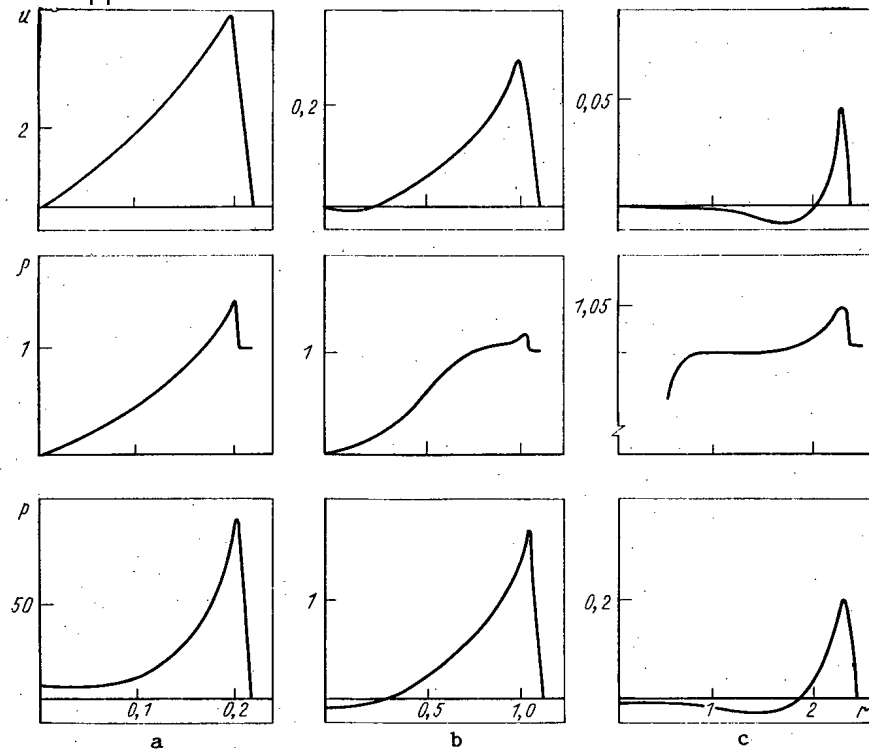


Fig. 1. Distribution of velocity, density, and pressure at various moments of DP evolution: a)  $t = 6 \cdot 10^{-3}$  (initial approximation); b) 0.3; c) 1.6.

and  $\tilde{\varepsilon}$  are the pressure, density, and energy, respectively; the time  $\tilde{t}$  and Lagrangian coordinate of the (initial) particle  $r_0$  are used as the independent variables (for convenience of calculation, these variables may be written in dimensionless form):

$$\begin{aligned} x &= \frac{\tilde{r}_0^3 \rho_1}{3E_0}; \quad t = \frac{\tilde{t} c_1 p_1^{1/3}}{E_0^{1/3}}; \quad p = \frac{\tilde{p}}{\rho_1}; \quad \rho = \frac{\tilde{\rho}}{\rho_1}; \quad u = \frac{\tilde{u}}{c_1}; \\ \tilde{r} &= \frac{r p_1^{1/3}}{E_0^{1/3}}; \quad \varepsilon = \frac{\tilde{\varepsilon}}{\varepsilon_1}, \end{aligned} \quad (1)$$

where  $c_1$  is the sound velocity in unperturbed material;  $\rho_1$  is the initial density;  $p_1 = B_0 / (2\Gamma + 1/3) = B_0 / \gamma$ ,  $\varepsilon_1 = p_1 / \rho_1$  are dimensional constants ( $B_0$  is the modulus of omnidirectional compression at 0 K;  $\Gamma$  is the Gruneisen parameter). In the given variables, the initial boundary problem takes the following form in spherical coordinates

$$\partial \rho / \partial t = -\rho (\partial u / \partial r + 2u/r); \quad (2)$$

$$\frac{\partial u}{\partial t} = -\frac{r^2}{\gamma} \frac{\partial p}{\partial x}; \quad (3)$$

$$\frac{\partial \varepsilon}{\partial t} = \frac{p}{\rho^2} \frac{\partial \rho}{\partial t}; \quad (4)$$

$$\frac{\partial r}{\partial t} = u; \quad (5)$$

$$\varepsilon = \frac{1}{\rho} \left( \frac{\rho^\gamma}{\gamma-1} + 1 \right) - \frac{\gamma}{\gamma-1} + \frac{p+1-\rho^\gamma}{\Gamma \rho}; \quad (6)$$

$$\begin{aligned} u(r, 0) &\equiv 0, \quad p(r, 0) \equiv 0, \quad \rho(r, 0) \equiv 1, \\ \varepsilon(r, 0) &\equiv 0; \end{aligned} \quad (7)$$

$$\begin{aligned} u(0, t) &\equiv 0; \\ 4\pi \int_0^{r'} \rho \left( \varepsilon + \gamma \frac{u^2}{2} \right) r^2 dr &= 1. \end{aligned} \quad (8)$$

$$p = \frac{B_0}{\gamma} \left[ \left( \frac{\rho}{\rho_1} \right)^\gamma - 1 \right] + \Gamma c_v T \rho \quad (9)$$

with subsequent elimination of T. The initial and boundary conditions in Eq. (7) reflect the homogeneity and isotropic behavior of the medium, which is initially at rest, taking account of spherical symmetry. The integral condition in Eq. (8) follows from the energy-conservation law.

In accordance with experience in solving gas-dynamic equations, numerical integration is performed by the difference-scheme method [5], which does not depend on the specific form of the equation of state and may be used, after slight modification, in introducing the real viscosity and heat conduction and also the empirical equation of state; see [6], for example. The essence of this method is finite-difference approximation of the initial system in Eqs. (2)-(6) by a scheme with a checkerboard grid; to insure continuous calculation, the pseudoviscosity  $q$  is used [5];  $q$  is taken into account in the initial scheme by replacing the gas-kinetic pressure  $p$  by the sum  $p + q$ . The difference-scheme equations take the following form after transformation to a form convenient for calculation and elimination of Eq. (6)

$$\begin{aligned} u_i^{n+1} &= u_i^n - \frac{\Delta t_n}{\gamma} \frac{p_{i+1/2}^n - p_{i-1/2}^n + q_{i+1/2}^n - q_{i-1/2}^n}{\Delta x_i} (r_i^n)^2; \\ r_i^{n+1} &= r_i^n + \Delta t_n u_i^{n+1}; \\ \rho_{i-1/2}^{n+1} &= \rho_{i-1/2}^n \frac{1-W}{1+W}, \quad W = \Delta t_n \left[ \frac{2(u_i^{n+1} + u_{i-1}^{n+1})}{r_i^{n+1} + r_i^n + r_{i-1}^{n+1} + r_{i-1}^n} + \frac{u_i^{n+1} - u_{i-1}^{n+1}}{r_i^{n+1} + r_i^n - r_{i-1}^{n+1} - r_{i-1}^n} \right]; \\ p_{i-1/2}^{n+1} &= \left\{ \left( \frac{2+\Gamma}{\Gamma} \rho_{i-1/2}^{n+1} - \rho_{i-1/2}^n \right) p_{i-1/2}^n + 2 \left( \frac{1+\Gamma}{\Gamma} + q_{i-1/2}^{n+1} \right) (\rho_{i-1/2}^{n+1} - \rho_{i-1/2}^n) + \right. \\ &\quad \left. + \left( \frac{2}{\Gamma} + \frac{2}{\gamma-1} \right) \rho_{i-1/2}^n \rho_{i-1/2}^{n+1} [(\rho_{i-1/2}^{n+1})^{\gamma-1} - (\rho_{i-1/2}^n)^{\gamma-1}] \right\} \times \frac{1}{\frac{2+\Gamma}{\Gamma} \rho_{i-1/2}^n - \rho_{i-1/2}^{n+1}}; \\ \Delta x_i &= 0,5 (\Delta x_{i+1/2} + \Delta x_{i-1/2}), \quad \Delta x_{i+1/2} = x_{i+1} - x_i, \end{aligned}$$

where  $\Delta t_n = t_{n+1} - t_n$ ;  $l \approx 5$  is a constant regulating the width of the front. In this scheme, for example,  $r_i^n$  denotes the Euler coordinate at the point  $(x_i, t_n)$ , while  $p_{i+1/2}^{n+1}$  is the pressure at the point  $(x_{i+1/2}, t_{n+1})$ . As usual, instead of  $u^{n-1/2}$  and  $u^{n+1/2}$ , the notation  $u^n$  and  $u^{n+1}$  is used. Note that in this form it is not necessary to use spatial interpolation of the grid functions, since the dynamic  $(r, u)$  and thermodynamic  $(p, \rho)$  functions are referred to different grid points. If this order of determining the unknowns is followed, an explicit solution of the scheme may be obtained. The local approximation of the differential equations with  $\Delta x = \text{const}$ ,  $\Delta t = \text{const}$  is  $O(\Delta x^2 + \Delta t^2)$ .

Stability of the difference scheme requires satisfaction of the following two conditions limiting the maximum time step [5, 7]

$$\begin{aligned} \Delta t &\leq \min [\Delta r_i^n (\rho_{i+1/2}^n / \rho_{i-1/2}^n)^{1/2}]; \\ \Delta t &\leq \frac{\pi^2}{2(\gamma+1)l^2} \min \left( \frac{\Delta r_i^n}{\Delta u_i^n} \right). \end{aligned}$$

The first of these is equivalent to the Courant condition in acoustics, while the second is taken from the theory of parabolic equations and acts at the front, where the pseudoviscosity changes the type of differential equation.

The initial approximation adopted is the self-similar solution of the problem of a strong point explosion in an ideal gas [8], modified to take account of the pseudoviscosity by "spreading" of the front. For a solid, this approximation is not completely correct, but the difference scheme ensures rapid reduction of the solution to the true form. A more cardinal solution would be the use of the results of dynamic modeling of the initial stage of cascade development as the initial approximation.

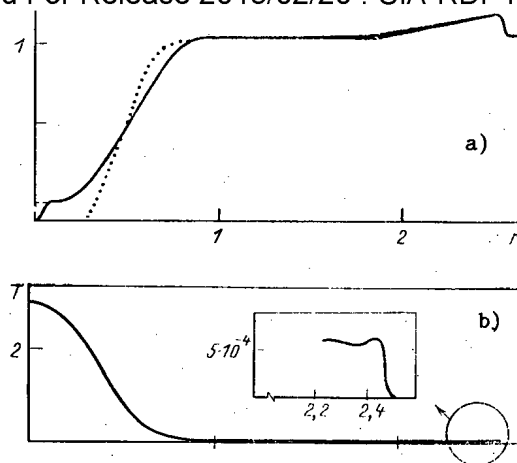


Fig. 2. Distribution of the density (a) and temperature in units of  $\epsilon_1/cv$  (b) in the concluding stages of DP. The corrected density profile is shown by a dashed curve; the dotted curve is the ideal-gas approximation.

As the wave propagates, an ever larger number of spatial points is involved in the calculation; therefore, to economize on machine time and to allow for the limited computer memory, successive adjustment of the grid with respect to the coordinate  $x$  on the basis of the cell-doubling principle is undertaken [7]; the resulting free cells are used to continue the calculation. The dynamic functions  $r$ ,  $u$  are simply renumbered here, and the new values of  $p$  and  $\rho$  are determined by linear interpolation.

To suppress parasitic oscillations of the grid functions  $f$  ( $=p, \rho, u$ ), the smoothing operator is used

$$f_i = \frac{\beta f_{i-1} \Delta x_{i+1} + (1-2\beta) f_i \Delta x_i + \beta f_{i+1} \Delta x_{i-1}}{(\Delta x_{i-1} + \Delta x_{i+1}) \beta + \Delta x_i (1-2\beta)},$$

where  $\beta \sim 10^{-3}$  is the smoothing parameter (particular to each function). However, in introducing the real viscosity of solids, there is no need for such smoothing.

Evolution of the shock wave is traced up to the moment of degeneration into an acoustic wave, when plastic flow of the material ceases. The pressure at the front must be reduced here [1, 2] to  $p_{cr} = 2(1-\mu)\sigma_{cr}/(1-\mu)$  where  $\sigma_{cr}$  is the critical shear stress for an ideal solid;  $\mu$  is Poisson's ratio.

Test calculation of an explosion in an ideal gas shows good agreement with the data of [9].

Modeling of DP evolution in a solid with the Gruneisen parameter  $\Gamma = 2$  characteristic of copper and aluminum, for example, is taken as the basic calculation. The spatial distributions of the density, pressure, and velocity at some characteristic moments of DP evolution are shown in Fig. 1. At the very beginning of the calculation, when  $t \approx 2 \cdot 10^{-2}$ , rapid adjustment of the solution is seen, accompanied by reduction in pressure and increase in density at the front. When  $t \approx 0.2$  the pressure at the DP center becomes equal to zero, and then takes negative values, which results in gradual outflow of material from the front. At the center, a cavern begins to form. The final stage is characterized by displacement of the region of motion of the material to the wavefront, which becomes steadily more similar to the usual acoustic wavefront. Except for the central cavern, the state of the material inside the DP (pressure, density, and velocity) is little different from its initial state,\*

\*The density distribution inside the cavern is shown by a dashed curve, since correction of the initial approximation in this region cannot be completed up to the end of the calculation.

Declassified and Approved For Release 2013/02/20 : CIA-RDP10-02196R000300070001-4  
and according to the results of [1] may be described by the model of a point explosion in an ideal gas with a counterpressure at  $\gamma = 2\Gamma + 1/3$ ; see the dashed curve in Fig. 2a. The non-zero density of the material obtained as a result of calculation corresponds more closely to the real state of solids and, even though the heat conduction has been neglected, leads to finite temperature values at the center of the DP (Fig. 2b).

Although, in contrast to dynamic modeling, the model of a continuous medium does not allow the formation of structural defects in DP to be traced at the microscopic level, analysis of the distribution of thermodynamic quantities (density, temperature, and pressure) gives important additional information on the action of irradiation on a solid.

#### Density Distribution

As noted in [1], the changing density distribution of the material after the completion of DP evolution may be identified with the formation of radiation defects: vacancies (in regions of reduced density) and interstitial atoms (in regions of increased density). In fact, the curves in Fig. 2a are very consistent with the classical ideas regarding DP structure: at the center, a vacancy aggregate forms (the Seeger depleted region [10]), followed by an intermediate layer, and then a layer enriched with interstitial atoms. However, whereas the DP dimension is usually taken to be approximately equal to the path length of dynamic kraudions [3], i.e., to be independent of the PEA energy, the density of radiation defects in DP must increase with increase in  $E_0$ . At the same time, according to calculations, the linear DP dimensions increase in proportion to  $E_0^{+1/3}$  [1], i.e., the defect density is independent of  $E_0$ . With increase in PEA energy, the layer of interstitial atoms will move away from the depleted zone and, for example, for the maximum value  $E_0 = 23$  keV [3], the intervening distance is more than 4 nm.\*

It is not yet possible to give a definite answer to the question of the stability of the vacancy aggregate, since the reduced density of the material and the sufficiently high temperature will favor structural rearrangements after the completion of DP evolution. Taking into account that the maximum size of the aggregation in copper is 2 nm, it is difficult to envisage complete resorption of the aggregate without the formation of a stable defect (pores or dislocation loops).

#### Temperature Distribution

In the view of numerous researchers (see [11], for example), the residual temperature rise (thermal peak) in the damaged region after the passage of the DP must play a large role in the formation of the final defect structure. The results of the present calculations make certain corrections to these ideas. First, since the volume of the DP (heated region) is proportional to  $E_0$ , the specific energy liberation must remain constant. Second, some of the PEA energy will be entrained by the acoustic wave, so that the resulting temperature rise is much less than that expected on the basis of simple estimates. If the dependence in Fig. 2b is averaged over the whole DP volume, the heating is 47°K for aluminum and 63°K for copper. A temperature above 1000°K is only characteristic for the region of the central cavern; the use of a more correct equation of state, taking account of irreversible energy consumption in the rupture of interatomic bonds evidently leads to even more considerable reduction in the temperature effect.

#### Pressure Distribution

The fairly considerable pressure (tens of GPa) at the shock wavefront is the most significant effect which is not directly described in atomistic models of radiation damage. This pressure must be taken into account in analyzing the possibility of phase transitions in DP [1]. In addition, in solid solutions, the displacement of the atoms will be determined by their mass: it is expected that the lighter components are shifted closer to the DP periphery under the action of the shock wave, and the central zone is hence enriched with the heavier components. This segregation of impurities, in turn, may initiate the decay of the solid solution and thereby influence the mechanical properties of alloys.

The generation of acoustic waves at the completion of DP evolution may also influence the mechanical properties. The possibility of additional plastic deformation of materials

\*This distance is equal to the maximum kraudion path length at 313°K and is more than eight times greater than the mean displacement of particles of the medium obtained by integrating the velocity.

Declassified and Approved For Release 2013/02/20 : CIA-RDP10-02196R000300070001-4  
with breakaway or dislocations from the stoppers under the action of the acoustic wave was noted in [12]; it is likely that the opposite effect, in which additional internal stress of the wave will result in the nucleation of microcracks in regions with weakened interatomic coupling, i.e., lead to brittle fracture of the material, is also possible.

The results of the calculation give a sufficiently good description of the peripheral regions of the DP. Correct consideration of the central depleted region requires, first, the use of a more realistic equation of state, valid in a broad range of density, pressure, and temperature values (in particular, describing phase transitions from the solid state to the liquid and gas states), and, second, taking account of the viscosity and heat conduction of the medium. At the same time, the model in its present form allows some important features of the dynamics of radiation damage to be elucidated. The possibility of using the experimental initial characteristics of the material significantly increases the reliability of the quantitative results, especially for disordered alloys and amorphous solids.

The great economy of computational work in comparison with atomistic calculations of cascades by the method of [13] is a definite advantage of the model. One calculation for specific values of the initial characteristics of the material occupying around 1 h of machine time on the EC-1033 computer allows the DP parameters to be obtained, by means of trivial scale change, for any PEA energy within the permissible range. This opens real prospects for the development of a universal DP catalog convenient for practical use.

#### LITERATURE CITED

1. V. Zhukov and A. Ryabenko, "The role of shock wave in low-energy recoil atom radiation damage," *Rad. Effects*, 82, 85-95 (1984).
2. Ya. B. Zel'dovich and Yu. V. Raizer, *Physics of Shock Waves and High-Temperature Hydrodynamic Phenomena* [in Russian], Nauka, Moscow (1966).
3. M. W. Thompson, *Defects and Radiation Damage in Metals*, Cambridge University Press, New York (1969).
4. *Explosion Physics* [in Russian], Nauka, Moscow (1975).
5. A. A. Samarskii and Yu. P. Popov, *Difference Methods of Solving Gas-Dynamic Problems* [in Russian], Nauka, Moscow (1980).
6. V. P. Zhukov, A. V. Demidov, and A. V. Ryabenko, "Simple semiempirical equation of state of metals for a wide range of pressure and temperature," *Fiz. Met. Metallov.*, 57, No. 2, 224-229 (1984).
7. H. Brode, *Computer Calculations of Explosions* [Russian translation], Mir, Moscow (1976).
8. L. I. Sedov, *Similarity and Dimensionality Methods in Mechanics* [in Russian], Nauka, Moscow (1972).
9. H. Brode, "Numerical solutions of spherical blast waves," *J. Appl. Phys.*, 26, No. 6, 766-775 (1955).
10. A. Seeger, "Radiation damage in solids," in: *Proceedings of the Second International PUAE Conference*, Vol. 6, OUN, Geneva (1958), p. 250.
11. S. T. Konobeevskii, *Action of Irradiation on Materials* [in Russian], Atomizdat, Moscow (1967).
12. V. L. Indenbom, "New hypothesis regarding the mechanism of radiation-stimulated processes," *Pis'ma Zh. Tekh. Fiz.*, 5, No. 8, 489-492 (1979).
13. Dzh. Vin'yard, "Dynamics of radiation damage," *Usp. Fiz. Nauk*, 74, No. 3, 435-459 (1961).

# EFFECT OF HELIUM BLISTERING ON THE HYDROGEN PERMEABILITY OF THE Kh18Ni10T STAINLESS STEEL

V. M. Sharapov, A. I. Pavlov, A. P. Zakharov,  
M. I. Guseva, and V. N. Kulagin

UDC 621.039.633

## INTRODUCTION

The recent calculations based on the model experiments [1] and computer simulation [2, 3] of the working conditions of the first wall of an INTOR thermonuclear reactor showed an excessively high level of hydrogen permeability (penetrance) in stainless steels. Although the temperature gradient across the wall thickness can considerably decrease the diffusion leakage of hydrogen [4], decreasing the hydrogen permeability of the first wall of the thermonuclear installations remains an acute problem.

The known methods of decreasing hydrogen permeability are based either on changing the surface-reaction rates using different coatings (or by modifying the surface condition) or on increasing the surface area available for reversible liberation of hydrogen without affecting the rate of the surface processes.

However, it is difficult to employ these methods because of the change in the given surface condition due to the action of electron, neutron, and ion bombardment, which invariably affects the hydrogen permeability of the wall material under the actual conditions. In particular, bombardment of stainless steels by helium ions leads to blistering and the formation of surface porosity and, consequently, to a change in hydrogen permeability.

## PROCEDURE AND EXPERIMENTAL RESULTS

In order to measure the hydrogen permeability of stainless steels in a glow-discharge plasma we followed the previously described procedure [5]. Tubular specimens having a wall thickness  $d = 0.5$  mm were used. Measurements were carried out in the 250-700°C temperature range at a hydrogen ion flux density  $j = 3 \cdot 10^{16} \text{ cm}^{-2} \cdot \text{sec}^{-1}$ ; the maximum energy of the ions amounted to 350 eV.

In order to create a surface network of blisters, the specimens were irradiated in advance with helium ions having an energy of 20 keV in an ILU-3 installation up to a dose of  $2.5 \times 10^{19} \text{ cm}^{-2}$ . The irradiated zone reached 100 mm at a beam width of 1 mm. Specimen rotation ensured uniform irradiation of the entire cylindrical surface. During irradiation, the specimen temperature did not exceed 100°C.

In order to monitor the surface condition after irradiating with helium ions and after the experiments on hydrogen permeability, we used an auxiliary (secondary) specimen in the form of a platelet (wafer) and fixed it to the experimental cylindrical specimen. The morphology of the irradiated surface was studied using a 'Camebax' scanning electron microscope.

Figure 1 is a microphotograph of the surface of the auxiliary specimen irradiated with helium ions. The radiation dose was slightly higher than the critical dose for blister formation, and the entire surface of the irradiated specimens was found to be covered with a network of opened up blisters. The blister density, evaluated from the micrographs, was found to be  $\sim 10^7 \text{ cm}^{-2}$ , and the average diameter was equal to 1-1.5  $\mu\text{m}$ .

The hydrogen permeability of the initial and the helium ion-irradiated specimens was determined under the usual conditions of interaction with molecular hydrogen as well as with glow-discharge plasma. Figure 2 shows the temperature dependence of hydrogen permeability of the initial specimen placed in molecular hydrogen at a pressure of 1.3 kPa. The penetrating hydrogen flux varies exponentially with temperature in the entire range under study

---

Translated from Atomnaya Energiya, Vol. 59, No. 1, pp. 33-35, July, 1985. Original article submitted September 14, 1984.



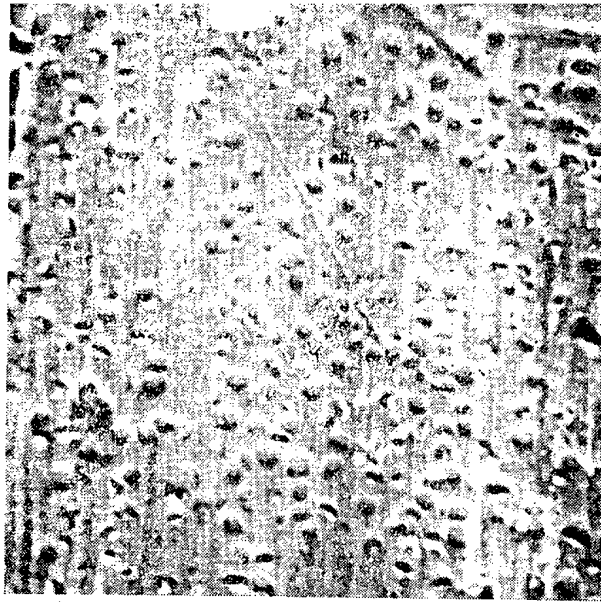


Fig. 1. Surface of the stainless steel after irradiating with  $\text{He}^+$  ions having an energy of 20 keV up to a dose of  $2.5 \times 10^{19} \text{ cm}^{-2}$  ( $\times 2 \cdot 10^3$ ).

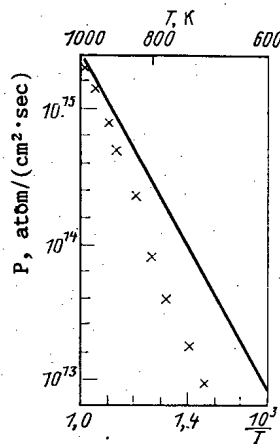


Fig. 2

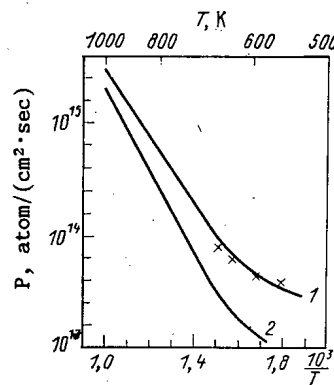


Fig. 3

Fig. 2. Temperature dependence of hydrogen permeability of the Kh18N10T stainless steel ( $d = 5 \cdot 10^{-2} \text{ cm}$ ,  $p = 1.3 \text{ kPa}$ ) in the atmosphere of molecular hydrogen: x) hydrogen permeability of the specimen irradiated in advance with  $\text{He}^+$  ions.

Fig. 3. Temperature dependence of the hydrogen permeability of the stainless steel in a glow-discharge plasma ( $d = 5 \cdot 10^{-2} \text{ cm}$ ,  $j = 3 \cdot 10^{16} \text{ cm}^{-2} \cdot \text{sec}^{-1}$ ); 1) original specimen; 2) specimen irradiated in advance with  $\text{He}^+$  ions.

according to the equation  $P = 8.3 \times 10^{18} \exp(-16,300 \text{ cal}/RT) \text{ atom}/(\text{cm}^2 \cdot \text{sec})$ , and the appearance of blisters after irradiating with helium ions leads to a marked reduction in hydrogen permeability, in particular, at low temperatures.

Hydrogen permeability of the initial specimens in the glow-discharge plasma (Fig. 3, curve 1) varies in a more complex manner: in the high-temperature region the activation

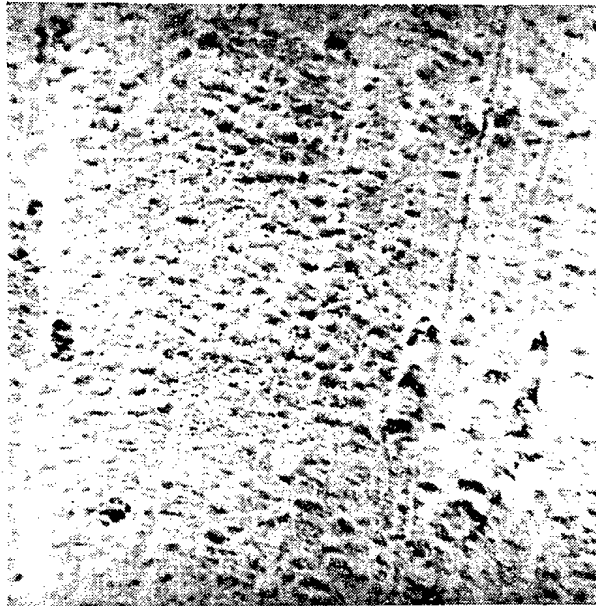


Fig. 4. Surface of steel after the experiments on determining hydrogen permeability in a glow-discharge plasma ( $\times 2 \cdot 10^3$ ).

energy amounts to 14.5 kcal/mole (60.3 kJ/mole), whereas in the low-temperature region there is a marked decrease in the activation energy. Hydrogen permeability is found to be greater than that in the atmosphere of molecular hydrogen: at high temperatures it is 1.5-2 times greater, and at low temperatures it is approximately 10 times greater. Surface blistering leads to a reduction in hydrogen permeability (Fig. 3, curve 2): by 2-2.5 times at high temperatures and by 3.5-4 times at low temperatures.

However, during longer duration of glow-discharge action (radiation dose  $\sim 10^{20} \text{ cm}^{-2}$ ) hydrogen permeability increases gradually up to the initial value (cross marks in Fig. 3). In this case, we observe a gradual smoothening of surface owing to ion sputtering and a reduction in the total number of blisters and their depth (Fig. 4).

#### DISCUSSION OF RESULTS

The aforementioned effect of prior irradiation with helium ions on hydrogen permeability is due to the morphological changes in the surface layer: the formation of blisters and the associated network of interconnected microchannels [6, 7].

Microporosity hinders diffusion of hydrogen into the metal because of the formation of shortened and easy migration paths towards the entrance surface. The hydrogen atoms reaching a microchannel would rather emerge out of the metal along these easy paths than diffuse into deeper layers. In the case of molecular hydrogen this can be considered to be the main reason for the reduced hydrogen permeability.

When hydrogen is introduced from the glow-discharge plasma, microporosity plays the same role as it does during penetration from the molecular phase. But, apart from this, the existing blisters also exert an effect on hydrogen permeability. During ion bombardment, a considerable portion of the introduced (interstitial) hydrogen diffuses to the side walls of the blisters and reenters the gas phase, because of which the total hydrogen flux through the membrane decreases. In this case, based on electron microscopy studies, we assume that at large radiation doses of helium ions, the blister walls are sufficiently steep (sharp), because of which hydrogen ions migrating in a direction perpendicular to the surface do not diffuse deep into the metal through the side surface of blisters.

It is evident that this effect is determined by the size, shape, and concentration of blisters, i.e., by the conditions of irradiation with helium ions, and it may be assumed that it will be significant at the radiation doses causing the formation of a number of blister generations. The formation of blisters cannot lead to a reduction in hydrogen per-

We note another consequence of helium ion irradiation which could lead to reduced hydrogen permeability. The surface layer at a depth corresponding to the mean free path of the helium ions is saturated with helium up to very high concentrations [7]. The radiation defects, gas-filled bubbles (in which the pressure may reach a few tens of megapascals [8]), and the development of high stress fields can hinder diffusion of hydrogen deep into the metal. Such an effect will also be observed at the radiation doses below the blister formation dose and, also, during simultaneous irradiation with hydrogen and helium ions.

Bombarding the metal surface with hydrogen ions under the glow-discharge conditions leads to gradual sputtering of the destructed layer containing blisters and micropores, because of which hydrogen permeability attains the initial value.

#### LITERATURE CITED

1. V. M. Sharapov, A. E. Gorodetskii, A. P. Zakharov, and A. I. Pavlov, "Hydrogen balance in an INTOR reactor," *At. Energ.*, 56, No. 1, 29-31 (1984).
2. M. Baskes, K. Wilson, and W. Bauer, USA Input to INTOR Workshop, Session III, Phase 2A, December (1981).
3. P. Wienhold, M. Profant, F. Waelbroeck, and J. Winter, *J. Nucl. Mater.*, 93-94, 866-870 (1980).
4. G. Casini and C. Ponti, Input to INTOR Workshop, Session IV, Phase 2A, March (1982).
5. V. M. Sharapov, A. P. Zakharov, and B. V. Matveev, "Effect of glow-discharge parameters on the penetration of hydrogen through molybdenum," *Zh. Tekh. Fiz.*, 45, 2002-2004 (1975).
6. G. Thomas and K. Wilson, *Trans. Am. Nucl. Soc.*, 27, 273 (1977).
7. W. Jäger and J. Roth, *J. Nucl. Mater.*, 93-94, 756-766 (1980).
8. W. Jäger, R. Manzke, H. Trinkaus, et al., *ibid.*, 111-112, 674-680 (1982).

#### GROWTH OF HELIUM PORES IN THE VICINITY OF AND AT THE GRAIN BOUNDARIES

A. I. Ryazanov, G. A. Arutyunova,  
V. A. Borodin, V. M. Manichev,  
Yu. N. Sokurskii, and V. I. Chuev

UDC 620.192.53

The buildup of helium in the structural materials of the present day nuclear and future thermonuclear reactors leads to a change of the microstructure and, consequently, of the mechanical properties of irradiated materials. As a result of the appearance of helium pores at dislocations and grain boundaries (Fig. 1), the contribution from the pores at the dislocations to swelling of the material can exceed the contribution from the volume pores [1]. The phenomenon of high-temperature radiation embrittlement of materials depends significantly on the distribution and sizes of the gas (helium) pores at the boundaries and in the body of the grains.

It is usually supposed [2-3] that this phenomenon is related with weakening of the grain boundaries of the material as a result of the buildup in them of helium atoms, the generation and growth of helium pores, and also with increase of the strength of the body of the grain as a result of interaction of linear dislocations with the helium pores. The change of strength of the material depends significantly on the relation between the strength of the grain boundary and the strength of the grain volume, and also the distribution of the helium pores associated with the dislocations. As the dimensions and density of the pores vary significantly, depending on the distance up to the grain boundary (see Fig. 1), then a satisfactory model of helium embrittlement must take into consideration the kinetics of the generation and development of the spatially nonuniform helium porosity in the material.

---

Translated from *Atomnaya Energiya*, Vol. 59, No. 1, pp. 35-39, July, 1985. Original article submitted November 5, 1984.

We shall consider the kinetics of the development of helium porosity during annealing of a material in which a supersaturated solution of point defects and helium atoms is created. The theoretical results obtained should be compared with the experimental data concerning the kinetics of the development of gas porosity in nickel, in which by irradiation with  $\alpha$ -particles in an accelerator, a defined concentration of helium atoms and radiation point defects is created. The procedure and conditions of irradiation of nickel samples in the accelerators and also the corresponding electron-microscopic investigations were described earlier in detail in [1].

The grain boundaries play a special role in the absorption of helium atoms. They can be represented in the form of loosened regions in which the average distances between the atoms is somewhat greater than in the volume of the grain. In view of this, the energy of dissolution of helium atoms at the boundary  $E_B$  is less than the energy of dissolution in the volume of the grain  $E_V$ . Therefore, an atom of helium having reached the boundary of a grain, in order to again return to the volume of the grain, must surmount an energy barrier  $\epsilon_m = E_V - E_B + E_C$ , where  $E_C$  is the binding energy of the helium atom with the boundary of the grain. The entry of helium atoms at the grain boundary is determined by the corresponding diffusion flow, which for plane geometry can be written in the form

$$D_m \left. \frac{\partial C_m}{\partial x} \right|_{x=\frac{l_b}{2}} = 2B_m [C_m]_{x=\frac{l_b+\lambda}{2}} - C_m \Big|_{x=\frac{l_b-\lambda}{2}} e^{-\epsilon_m/T}. \quad (1)$$

Here  $C_m = C_m(x, t)$  and  $D_m$  are the concentration and coefficient of diffusion of helium atoms at the position of implantation ( $m = g$ ) and at the position of occupation ( $m = s$ ), respectively;  $l_b$ , size of the grain boundary;  $B_m \approx D_m/\lambda$ , velocity of transfer of helium atoms through the grain boundary;  $\lambda$ , average length of "skip" of the atom, similar to the interatomic distance ( $\lambda \approx a$ );  $T$ , temperature. In the future, for simplicity, we shall refer the given boundary condition to  $x = 0$ .

The distribution of helium atoms in the vicinity of the grain boundary can be found by solving the diffusion equation

$$\frac{\partial C_m}{\partial t} = D_m \frac{\partial^2 C_m}{\partial x^2} - S_m D_m C_m + G_m \quad (m = g, s), \quad (2)$$

where  $S_m$  and  $G_m$  are the density of collectors and the rate of generation of helium atoms.

The characteristic time of establishment of a quasisteady distribution of helium atoms in the volume of the grain is determined by their diffusion drift into the sink and is equal to  $\tau_m = (S_m D_m)^{-1}$ . In simulation experiments, conducted in charged particle accelerators, the characteristic time of irradiation amounts to  $t_{irr} \approx 10^3 - 10^5$  sec, which is significantly less than the characteristic time of establishment of a quasisteady distribution. (For example, for nickel, the migration energy of helium atoms in the position of substitution  $E_s = 2.5$  eV [4], while at an irradiation temperature of  $T_{irr} = 400^\circ K$  and a dislocation density of  $\rho_d = 10^8 - 10^{10} \text{ cm}^{-2}$ , the time  $\tau_s = 10^{18} - 10^{20}$  sec, i.e.,  $\tau_s \gg t_{irr}$ .) Therefore, the diffusion of helium atoms in positions of substitution is significant only at the stage of high-temperature post-radiation annealing, and in Eq. (2) for  $m = s$ , the term  $G_s$  is missing. (Similarly, also for the diffusion of vacancies in the volume of the grain, the migration energy of vacancies in nickel  $E_v = 1.3$  eV [4].)

A quite different situation arises for helium atoms in the implantation position, when the migration energy is small (for example, for helium atoms in nickel in the implantation position  $E_g \approx 0.15 - 0.3$  eV [4]). Therefore, with  $T_{irr} \approx 400^\circ K$ , we obtain  $\tau_g \ll t_{irr}$ . The migration energy of the inherent interphase atoms in nickel  $E_i \approx 0.1$  eV [4]; they diffuse during irradiation and form increasing dislocation loops.

This relation between the characteristic times of the diffusion processes allows the decay process of a supersaturated solution of point defects and helium atoms to be considered successively.

In the initial stage, the helium atoms diffuse to the implantation position (during irradiation or during post-radiation annealing, depending on the irradiation temperature), then post-radiation annihilation of vacancies takes place and, finally, after a sufficiently long time the helium atoms start to drift from the positions of substitution. As the rela-

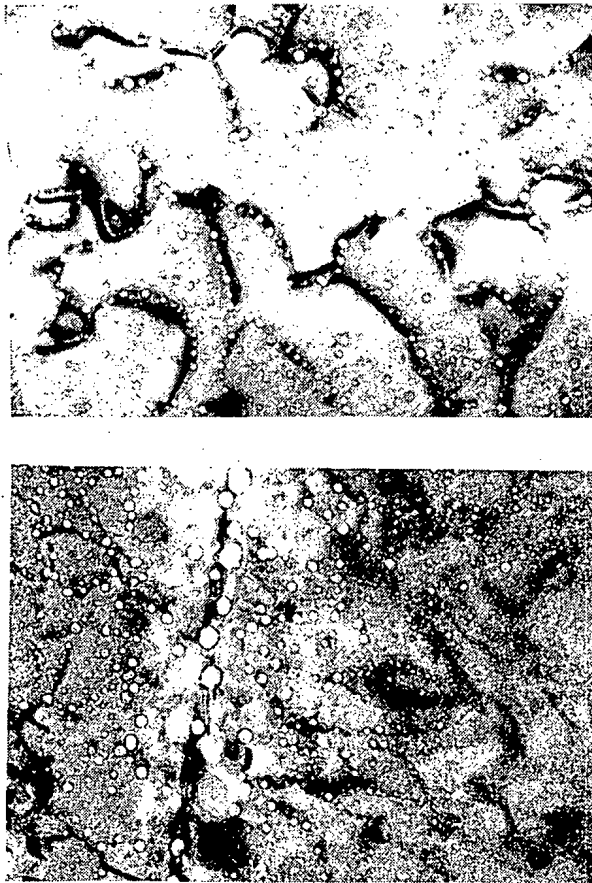


Fig. 1. Defect structure of nickel saturated with helium ions up to a concentration of 0.15%, in the vicinity of the grain boundaries: upper)  $T = 700^\circ\text{C}$ ,  $t = 1000$  h,  $\times 200,000$ ; lower)  $T = 800^\circ\text{C}$ ,  $t = 10$  min,  $\times 100,000$ .

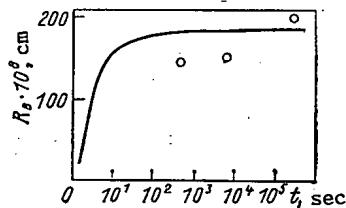


Fig. 2

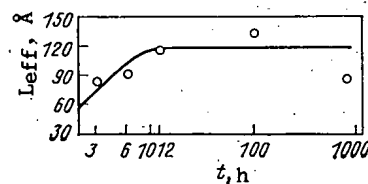


Fig. 3

Fig. 2. Dependence of the pore radius at the grain boundary  $R_b(t)$  on the time of annealing: —) theoretical curve; o) experimental data.

Fig. 3. Dependence of  $L_{\text{eff}}$  on the time of annealing at  $T = 700^\circ\text{C}$ .

tion  $E_i \leq E_g < E_v < E_s$  between the values of the energy of migration of point defects is quite general for a large part of metals [4-5], the model of the successive consideration of the decay kinetics of a supersaturated solution of point defects is applicable not only for nickel, but also for other metals. When considering the decay kinetics of a supersaturated system we shall suppose that the process of generation of helium pores occurs over a time less than the characteristic time of drift of helium from the positions of substitution, and with  $t \sim \tau_s$  a system of minute helium bubbles has formed already in the material.

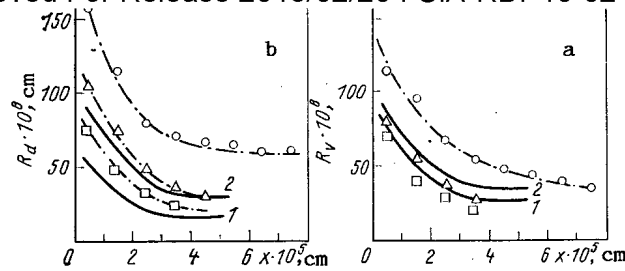


Fig. 4. Dependence of the average radius of the volume (a) and dislocation (b) pores on the distance to the grain boundary for a duration of annealing of 10 min ( $\square$ ), 100 min ( $\Delta$ ), and 100 h ( $\circ$ ).

We shall consider the first stage of the kinetics of the process, for which  $\tau_g \ll t_{irr}$ . In this case, for  $t_{irr} \geq t > \tau_{Dg}$  (where  $\tau_{Dg} \approx L^2/D_g$  and  $L$  is the size of the grain), Eq. (2) has a quasisteady form. Writing the boundary condition (1) for  $x=0$  and  $x=L$ , and assuming the capacity of the sinks  $S_g$  to be constant, we obtain Eq. (2) with  $\varepsilon_g/T \ll 1$ ,  $\lambda\sqrt{S_g} \ll 1$ , and  $L\sqrt{S_g} \gg 1$  in the following form:

$$C_g(x) = \frac{G_g}{S_g D_g} [1 - e^{-\sqrt{S_g}x} - e^{\sqrt{S_g}(x-L)}]. \quad (3)$$

It is clear that in this case the flow of helium at the grain boundary is small, and for  $t < \tau_{Dg}$  the concentration of helium in the material is still small.

With  $\tau_g \gg t_{irr}$ , a spatially uniform distribution of helium atoms is formed during irradiation, which then diffuses at a higher annealing temperature ( $T \gg T_{irr}$ ). With  $t > t_{irr}$  the generation of helium atoms is missing in Eq. (2) ( $G_g = 0$ ). As the diffusion in-leakage of helium atoms at the grain boundary takes place mainly over a time  $t \sim \tau_g$  ( $\tau_g$  is the time of propagation of the diffusion front to a characteristic distance  $S_g^{-1/2}$  from the grain boundary), then the second boundary condition for Eq. (2) can be substituted by the requirement of boundedness of the solution with  $x \rightarrow \infty$ . Taking into account the initial condition  $C_g|_{t=0} = C_{g0}$ , we obtain the following expression for the concentration of helium atoms at the position of implantation in the vicinity of the grain boundary:

$$C_g(x, t) = C_{g0} e^{-t/\tau_g} \left\{ \Phi(x/x_t) + e^{\frac{x}{\lambda} + \frac{x_t^2}{4\lambda^2}} \left[ 1 - \Phi\left(\frac{x}{x_t} + \frac{x_t}{2\lambda}\right) \right] \right\}, \quad (4)$$

where

$$x_t = 2\sqrt{D_g t}; \quad \Phi(z) = \frac{2}{\sqrt{\pi}} \int_0^z e^{-\xi^2} d\xi.$$

The concentration of helium atoms at the boundary is described by the relation

$$C_g^b(t) = C_{g0} + 2C_{g0} \frac{\lambda}{l_b} \left\{ e^{\frac{x_t^2}{4\lambda^2}} \left[ 1 - \Phi\left(\frac{x_t}{\lambda}\right) \right] + \frac{1}{\lambda\sqrt{S_g}} \Phi\left(\frac{x_t\sqrt{S_g}}{2}\right) \right\}. \quad (5)$$

As  $\lambda\sqrt{S_g} \ll 1$ , then when  $t \rightarrow \infty$  the concentration of helium at the boundary will be significantly greater than the volume concentration,  $C_g^b \approx C_{g0} 2/\lambda\sqrt{S_g} \gg C_{g0}$ . In order to estimate the density of the helium pores formed in the volume of the grain, we shall use the simplest model, according to which with a high concentration of helium in the material, the stable nucleus of helium pores is small and may consist of two atoms of helium and one-two vacancies. We shall assume, therefore, that the rate of formation of stable nuclei is determined by the collision frequency of helium atoms in the positions of implantation and substitution  $J(x) \approx \alpha_g C_g(x) C_s$ , where  $\alpha_g$  is the coefficient of recombination. In the next stage, stabilization of these nuclei is possible as a result of vacancies joining with them. The density

Declassified and Approved For Release 2013/02/20 : CIA-RDP10-02196R000300070001-4  
of the gas pores formed at the instant  $t \approx \tau_N$  (where  $\tau_N$  is the characteristic time of the course of the nucleation process), is equal to  $N(x) \approx J(x)\tau_N$ . In the case of high-temperature irradiation, using relation (3) and assuming that  $\tau_N \approx \tau_{irr}$ , we obtain the following relation for the density of the gas pores in the volume of the grain:

$$N_v(x) = N_{v0} [1 - e^{-x/L_v} - e^{-(L-x)/L_v}]. \quad (6)$$

Here  $L_v = S_g^{-1/2}$  is the scale of nonuniform distribution of helium pores in the volume;

$$N_{v0} \approx \frac{\alpha_g G_g C_s \tau_N}{S_g D_g}.$$

In the case of low-temperature irradiation, taking into account relation (4) and assuming that  $\tau_N \approx \tau_g$ , we obtain the following approximation for  $N_v(x)$ :

$$N_v(x) = \begin{cases} N_{v0} \frac{x}{L_v}, & 0 \leq x \leq L_v; \\ N_{v0}, & L_v \leq x \leq L/2, \end{cases} \quad (7)$$

where

$$L_v = 2 \sqrt{D_g \tau_g} = 2 S_g^{-1/2}.$$

Further, we assume that the density distribution of dislocation pores is determined by the concentration of helium in the nucleus of the dislocation, and therefore it is not difficult to see that the relations  $N_d = N_d(x)$  and  $N_v = N_v(x)$  are similar; hence the scale of the spatially nonuniform distribution of dislocation pores  $L_d = L_v$ .

We note that if the generation of helium pores in the volume of the grain is determined by the process of vacancy annihilation, then the investigation of the diffusion equation for vacancies, similar to Eq. (2), shows that in this case the characteristic scale of the spatially nonuniform distribution of the concentration of volume helium pores  $L_v = 2 S_v^{-1/2}$ , where  $S_v$  is the density of the sinks for the vacancies. If the principal sinks for the point defects are dislocations, then  $S_g \approx Z_{gpd}$  and  $S_v \approx Z_{vpd}$  and  $L_d/L_v = (Z_v/Z_g)^{1/2}$ , where  $Z_g$  and  $Z_v$  are coefficients taking account of the interaction of helium atoms in the positions of implantation and vacancies with dislocations.

After the stage of generation of helium pores, their intense growth starts. As experiments carried out show [1], the rate of growth of gas pores is quite small and is determined mainly by the slower moving atoms of gas found at positions of substitution.

We shall consider the growth kinetics of the gas pores at the boundaries, dislocations, and in the volume of the grains, in the conditions of nonsteady decay of a saturated solution of helium atoms in positions of substitution. The growth of the helium pores at the boundaries goes in two stages [6]: first of all the helium atoms diffuse to the grain boundary, then they diffuse along it to the grain-boundary pores.

The diffusion of the helium atoms existing at the boundary to the nucleus of the pore is described in cylindrical geometry by the equation

$$\frac{\partial C_s^b}{\partial t} = D_s^b \frac{1}{r} \frac{\partial}{\partial r} \left( r \frac{\partial C_s^b}{\partial r} \right) + \frac{2 D_s}{b \lambda} [C_s]_{x=\frac{\lambda}{2}} - C_s^b e^{-e_s/T}, \quad (8)$$

where  $C_s^b$  is the concentration of helium at the grain boundary, and  $D_s^b$  is the coefficient of diffusion of helium through the grain boundary.

The initial and boundary conditions for Eq. (8) have the form

$$\begin{aligned} C_s^b|_{t=0} &= C_{s0}^b, \quad C_s^b|_{r=R_b} = 0; \\ \frac{\partial C_s^b}{\partial r} \Big|_{r=L_b} &= 0. \end{aligned} \quad (9)$$

The change of quantity of gas in the pore at the grain boundary is determined by the relation

$$\frac{dn_g^b}{dt} = 2\pi\omega^{-1}l_b R_b D_s \left. \frac{\partial C_s^b}{\partial r} \right|_{r=R_b}, \quad (10)$$

where  $\omega$  is the atomic volume.

If we assume that the gas in the pores is ideal and its pressure is balanced by the surface tension forces, then the number of atoms of gas in the pore  $n = (4\pi/3)R_b^3/\omega$ , where  $R_b = 2\gamma\omega/T$ ;  $\gamma$  is the coefficient of surface tension of the material [1]. Neglecting in Eq. (8) the slow leakage of helium from the position of substitution at the grain boundary ( $D_s^b \gg D_s$ ), we obtain from relations (8)-(10) the following expression for the kinetics of growth of the pore radius at the grain boundary (Fig. 2)

$$R_b^2(t) = R_b^2(0) + R_{b0}^2(1 - e^{-t/\tau_b}), \quad (11)$$

where

$$R_{b0}^2 = \frac{3}{2} \frac{l_b \tau_b \kappa}{R_s} D_s^b C_{s0}^b; \quad \tau_b = \frac{2D_s^b}{l_b^2 \ln \frac{1}{\mu}}; \\ \kappa = \ln \frac{1}{\mu} / \ln^2 \chi; \quad \chi = L_b/R_b; \quad \mu = \sqrt{2}/\chi \ln^{1/2} \frac{1}{\mu}.$$

Remote from the grain boundaries, the growth kinetics of the volume  $R_v$  and dislocation pores  $R_d$  is equal to [1]

$$R_v(t) = R_\infty \frac{1 - e^{-t/\tau_s}}{1 + \eta e^{-t/\tau_s}}; \\ R_d(t) = [R_L R_v(t)]^{1/2}. \quad (12)$$

Here  $R_L = Z_s l_d / 2\pi$ ;  $l_d$  is the average distance between pores at the dislocations;  $\tau_s^{-1} = (4\pi N_v D_s R_\infty + Z_s D_s \rho_d)$ ;  $\eta^{-1} = 1 + 2\pi N_s R_\infty / Z_s \rho_d$ , and  $Z_s$  is a coefficient taking into account the interaction of a helium atom in the substitution position with a dislocation;  $R_\infty$  is the maximum radius of the volume pores, determined from the relation

$$C_{s0} = \frac{4\pi}{3} N_v R_s R_\infty^2 + \frac{2}{3} Z_s \rho_d R_s R_\infty; \\ C_{s0} = C_s|_{t=0}.$$

In accordance with the model developed,  $R_d/R_v = (Z_s l_d / 2\pi R_v)^{1/2} > 1$ . An experiment conducted in conjunction with electron-microscopic investigations of the irradiated samples showed that  $R_d/R_v \approx 1.5$ . Consequently, tubular diffusion of helium atoms along the dislocations toward the pores located at these dislocations is the principal mechanism determining the growth of the latter.

For a quantitative comparison of the theoretical results with the experimental data, we shall use the dependence of the parameter  $L_{eff}$  on the duration of annealing (Fig. 3). This parameter represents the average ratio of the total surface area of all pores lying on one dislocation to the length of this dislocation, and it is important to note that it is independent of the characteristics of the individual dislocation. In accordance with relations (12), the expression for  $L_{eff}$  has the form

$$L_{eff} = 2Z_s R_\infty \frac{1 - e^{-t/\tau_s}}{1 + \eta e^{-t/\tau_s}}. \quad (13)$$



An investigation of the system of equations (1) for the growth of the volume and dislocation pores in the vicinity of the grain boundary, taking account of the spatially nonuniform dislocation density and the spatially nonuniform density distribution of the volume and dislocation pores, shows that with the characteristic time of growth of the volume and dislocation helium pores  $\tau$  [ $\tau^{-1} = \tau_v^{-1} + \tau_d^{-1}$ ;  $\tau_d \approx (8\pi/3)(R_d^2 R_s)/(Z_s \ell_d D_s C_s)$ ;  $\tau_v \approx R_s R_v/(D_s C_s)$ ] less than the characteristic time of diffusion in the volume  $\tau_L$  ( $\tau_L \approx L^2/D_s$ ), the following spatially nonuniform distribution of the average dimensions of the dislocation and helium pores is formed (Fig. 4):

$$R_v(x) = \frac{Z_s \rho_d(x)}{4\pi N_n(x)} \left[ \sqrt{1 + \frac{12\pi C_{s0} N_v(x)}{Z_s^2 R_s \rho_d^2(x)}} - 1 \right];$$

$$R_d(x) = \sqrt{\frac{Z_s \ell_d(x)}{2\pi} R_n(x)}.$$
(14)

Thus, in the initial stage of generation of helium pores, in consequence of the diffusion drift of helium atoms at the grain boundary, a spatially nonuniform distribution of the volume and dislocation pores is formed, the concentration of which  $N_v(x)$  and  $N_d(x)$  increases in the direction from the surface of the grain. This density distribution of helium pore nuclei leads at the growth stage to the formation of bigger pores in the vicinity of the grain boundaries. The largest pores are observed at the grain boundaries, which is related with the higher mobility of the helium atoms along the boundaries by comparison with their mobility in the volume of the grains. The resulting distribution of helium pores can exert a significant effect on the mechanism of the high-temperature destruction of the material of the sample.

#### LITERATURE CITED

1. A. Ryazanov, G. Arutyunova, V. Borodin, Yu. Sokursky, and V. Chuev, J. Nucl. Mater., 110, No. 1, 65 (1982).
2. H. Trinkaus and H. Ullmaier, Philos. Mag., 39, No. 6, 563 (1979).
3. N. M. Kiryukhin and L. S. Ozhigov, "Role of the Evolution of Gas Bubbles in High-Temperature Radiation Embrittlement of Materials," Problems of Nuclear Science and Technology. Series Physics of Radiation Damage and Radiation Material Behavior [in Russian], No. 3(11) (1979), pp. 3-9.
4. A. Holland, "Recent study of point defects in metals. Selected problems," in: Point Defects in Solids [Russian translation] (1979), pp. 243-375.
5. A. N. Orlov and Yu. V. Trushin, Energy of Point Defects in Metals [in Russian], Énergoatomizdat, Moscow (1983).
6. V. V. Slezov, "Coalescence of a supersaturated solid solution in the case of diffusion through the boundaries of blocks or dislocation lines," Fiz. Tverd. Tela, 9, No. 4, 1187-1196 (1967).

# HYDROGEN PERMEABILITY IN STAINLESS STEEL INTERACTING WITH TM-4 TOKAMAK PLASMA

V. I. Bugarya, S. A. Grashin,  
A. V. Pereslavl'tsev, Yu. M. Pustovoi't,  
V. S. Svishchev, A. I. Livshits,  
and M. E. Notkin

UDC 621.039.616

One of the major criteria in choosing the material for the first wall in a fusion reactor is the hydrogen permeability  $\chi$ , which is related to the hydrogen accumulation  $N$ . Numerous experiments [1-3] have shown that the numerical values of  $\chi$  and  $N$  can vary by several orders of magnitude even for a single material in accordance with the state of the surface and the states in the gas (molecules, atoms, or ions). In a real fusion reactor, the gas is substantially out of equilibrium, while the state of the surface in the first wall is very much dependent on the physicochemical processes in the reactor.

The present study was designed to provide data by direct measurement of the deuterium flux penetrating a membrane made of Kh18N9T stainless steel when acted on by the TM-4 plasma. The instrument shown in Fig. 1 was used to measure the direct penetration of hydrogen (isotopes) through the stainless steel.

The metal tube 6 bears the membrane 2 at the end and is inserted via the tube 3 into the toroidal chamber 1 of the tokamak. The quartz lamp 5 allows the membrane to be heated to about 500°C; the temperature is monitored by the thermocouple 4. The pressure in the volume 7 is monitored by the PMI-3-2 gauge 8, while the gas composition is examined by the monopolar mass spectrometer 9. The pumping rate in volume 7 for hydrogen via the tube 10 is  $1.3 \text{ dm}^3 \cdot \text{sec}^{-1}$ .

The experiments were performed with a TM-4, whose major radius was 53 cm and the minor radius 10 cm, radius of diaphragm 8.5 cm. The chamber was made of stainless steel, while the diaphragm was made of molybdenum. Working parameters: toroidal magnetic field about 1.5 T, discharge current 23 kA, mean electron density  $2 \times 10^{13} \text{ cm}^{-3}$ , electron and ion temperatures at the axis 500-700 and 100-130 eV correspondingly,  $Z_{\text{ef}} = 2.0-2.5$ , discharge duration  $t_d = 30 \text{ msec}$ , and interval 80-200 sec. The initial deuterium pressure ahead of the discharge was  $1-3 \times 10^{-2} \text{ Pa}$ . The residual pressure before admitting the working gas was  $1-1.3 \times 10^{-4} \text{ Pa}$ . The residual-gas spectrum was monitored with an APDM-1 mass spectrometer. The penetration probability  $\chi$  was determined from the ratio of the transmitted flux  $Q_{\text{tr}}$  to the incident flux  $Q_{\text{inc}}$ , i.e.,  $\chi = Q_{\text{tr}}/Q_{\text{inc}}$ .

Before the experiments were performed, the necessary vacuum conditions were provided by heating the TM-4 chamber to 400°C and the instrument to 200°C. After the heating, the residual-gas spectrum in the measurement volume was determined by the components having  $M/e = 2$  and 28. To distinguish the signal reliably from the background, the experiments were performed with deuterium ( $M/e = 4$ ). The specific deuterium flux incident on the wall and on the membrane was estimated by absolute measurement of the intensity of the  $D\beta$  line and the plasma density distribution [4]. In the subsequent calculations, it was taken as

$$q_{\text{inc}} = (3 \pm 1) \cdot 10^{16} \text{ cm}^{-2} \cdot \text{sec}^{-1}.$$

The flux at the wall consists of ions and fast atoms. In the TM-4, the ion energy was  $E_i = 20-40 \text{ eV}$  and the energy of the atoms was  $E_0 = 10-30 \text{ eV}$ .

To eliminate passivating (contaminating) films, including oxide ones, the membrane was bombarded under the conditions of a running-in discharge, which was used to clean the wall of the discharge chamber. This discharge was produced by inducing an eddy voltage at 500 Hz with an amplitude of 300 V in the presence of a toroidal magnetic field of 0.05 T.

---

Translated from *Atomnaya Energiya*, Vol. 59, No. 1, pp. 40-42, July, 1985. Original article submitted December 26, 1984; revision submitted March 13, 1985.

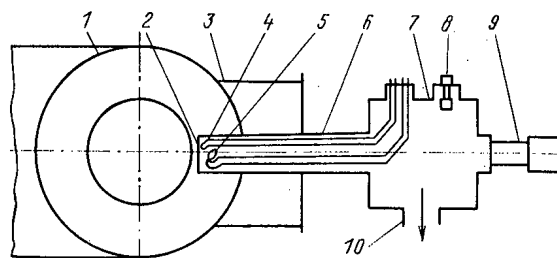


Fig. 1. Instrument for measuring the flux of hydrogen through a stainless-steel membrane.

TABLE 1. Probability of Deuterium Penetrating Stainless Steel and Rise Time  $\tau_{0.5}$  of the Signal to 0.5 of the Maximum

Parameter	Before purification		After purification	
	300°C	400°C	300°C	500°C
Penetration probability $\tau_{0.5}$	$1.9 \cdot 10^{-3}$ 65	$2.26 \cdot 10^{-3}$ 20	$1.7 \cdot 10^{-4}$ 18	$9.02 \cdot 10^{-4}$ 4

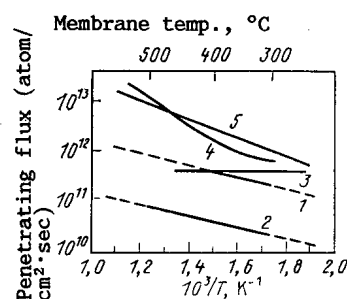


Fig. 2. Temperature dependence of the hydrogen permeability of stainless steel on interaction with a plasma at  $Q_{inc} \approx 10^{16}$  atoms per  $\text{cm}^2 \cdot \text{sec}^{-1}$ : 1) before the passivating films are removed; 2) after removal; 3) data of [3]; 4) data of [5]; 5) calculation of [6]. The permeability has been calculated for a membrane of thickness 0.5 cm in order to render the various data comparable.

No direct measurements were made on the particle flux and energy in the discharge. We use the data on the fast-atom flux and the electron concentration in this discharge to estimate the specific flux at the wall in the running-in discharge as  $1-3 \times 10^{16} \text{ cm}^{-2} \cdot \text{sec}^{-1}$ . The particle flux at the membrane in the running-in condition was about 3000 times higher than the time-averaged particle flux (with allowance for the duty cycle) under the working conditions. Spectral measurements were made on the luminosity of the ionized atoms of impurities in the running-in discharge, which enabled us to estimate the energy of the particles incident on the wall as 2-10 eV.

Therefore, under the working condition the average particle flux at the membrane in particles per second is

$$Q_{inc} = q_{inc} F_{td} n / t_e,$$

We measured  $Q_{tr}$  from the increase in the partial pressure of  $D_2$  in the measurement volume;  
the value of  $\chi$  was determined when the stationary permeability was attained, which gave a lower  
bound, since the flux of HD molecules accompanying the  $D_2$  flux was not allowed for because of  
the relatively high initial background. Estimates indicated that the increment in the HD pres-  
sure was comparable with that in the  $D_2$  one.

After the experiments, membrane temperatures of 300 and 400°C were used to examine the  
effects of surface contaminants on  $\chi$ . A running-in discharge was struck in the tokamak cham-  
ber, and for 1-1.5 h the particles emerging from the plasma etched (sputtered) the membrane.  
The membrane temperature in the running-in discharge condition was about 570°C. When the  
running-in discharge had been turned off and the membrane was outgassed, experiments were  
performed with membrane temperatures of 300, 400, and 500°C. The measured penetration coeffi-  
cients (probabilities) are given in Table 1 for the various temperatures and surface states, together  
with the characteristic time  $\tau_{0.5}$  for the penetrating flux to reach half the maximum.

Figure 2 shows the dependence of  $\chi$  on the reciprocal temperature, as well as values of  $\chi$   
obtained by calculation and by simulation, for comparison.

The experiments on the TM-4 were performed with Kh18N9T steel of thickness 20  $\mu$ m and gave  
the following results:

1) At 300°C, the initial permeability is extremely high:  $\chi \approx 2 \cdot 10^{-3}$ ;

2) treating the input surface with a discharge for 1-1.5 h with a sputtering flux of  
about  $10^{16}$  particles per cm $^2$  per second reduced the permeability at a given temperature by  
more than a factor 10. With this flux and a particle energy of 10 eV, the running-in process  
sputtered about 10 monolayers from the surface in 1-1.5 h (sputtering coefficient about  $10^{-5}$ ).

The permeability increased with temperature. The activation energy for the permeability  
given by these data is 12.6 kJ/mole.

The settling time for the stationary permeability is reduced by the etching.

The interaction model of [1] indicates that  $\tau_{0.5} \sim Q_{tr}^{-1/2}$  for a fixed surface state,  
i.e., the settling time should increase as the penetrating flux decreases. The observed  
reduction in  $\tau_{0.5}$  indicates change in the state of the input surface such as to favor the  
desorption of the absorbed particles, which reduces  $\chi$  and  $\tau_{0.5}$ .

Therefore, the experiments with the TM-4 and the data of [4] indicate relatively high  
hydrogen permeability for austenitic stainless steel interacting with particles of energy  
over 10 eV and also that the permeability is very much dependent on the surface state. At  
the same time, the experiments show that future fusion reactors with design particle fluxes  
and energies at the first wall of about  $10^{16}$  cm $^{-2}$ ·sec $^{-1}$  and about 100 eV will have fuel per-  
meability that can be brought to acceptable levels from the safety viewpoint quite rapidly.  
Also, etching the first wall facilitates absorbed-particle desorption and tends to reduce  
the fuel concentration in the material.

#### LITERATURE CITED

1. A. I. Livshits, "The interaction of a baffle with a nonequilibrium gas in the case of  
absorption accompanied by dissociation," Zh. Tekh. Fiz., 46, Issue 2, 328-338 (1976).
2. A. I. Livshits, M. E. Notkin, Yu. M. Pustovoit, and A. A. Samartsev, The Interaction  
of Thermal Hydrogen Atoms and Molecules with Metallic Membranes [in Russian], Preprint  
IAÉ-3517/8, Moscow (1981).
3. A. I. Livshits, M. E. Notkin, Yu. M. Pustovoit, and S. V. Yakovlev, "The transmission  
and absorption of hydrogen atoms and ions by 1Kh18N9T stainless steel," Aspects of Nu-  
clear Science and Engineering, Fusion Synthesis Series [in Russian], Issue 2(10) (1982),  
pp. 73-76.
4. S. A. Grashin, Yu. A. Sokolov, L. E. Gorodetskii, et al., The Interaction of Hydrogen  
with Metal in the Discharge Chamber of the TM-4 Tokamak [in Russian], Preprint IAÉ  
3622/7, Moscow (1982), 24 pp.
5. V. M. Sharapov, A. E. Gorodetskii, A. P. Zakharov, and A. I. Pavlov, "The hydrogen  
balance in the INTOR reactor," At. Energ., 56, Issue 1, 29-31 (1984).
6. M. Baskes, Report SAND80-8201, Sandia National Laboratories, Livermore (1980).

## MICROWAVE BEAM INSTABILITY IN PROTON SYNCHROTRONS

V. I. Balbekov and S. V. Ivanov

UDC 621.384.634

1. Introduction

A systematic approach to the longitudinal instability of bunched beams was first developed by Lebedev [1]. The problem reduces to an infinite system of equations for the harmonics of the beam current or to an equivalent integral equation for the charge density.

Most later work actually represents an attempt to solve this system under some simplifying assumptions. The following assumptions are most often used: 1) All bunches are the same and are located at equal distances from one another; 2) the impedance of the chamber is determined by a narrow-band resonant element; 3) the instability appears in the form of multipole oscillations of the bunches (dipolar, quadrupolar, etc.), and there is no coupling between different multipoles (see, for example, [2]).

The first two assumptions in many cases are consistent with the real situation, while the third is less obviously so. The difference in the frequency of the oscillations of two neighboring multipoles is equal to the synchrotron frequency. It is usually small, so that even comparatively small perturbations, for example, the nonlinearity of the accelerating field, can produce a strong coupling between the multipoles and change the nature of the instability. There are two points of view regarding this. According to the first one, the instability at the beginning always has a multipolar character, and a significant coupling between different multipoles appears only with a quite large increment [3]. Other authors prefer in the case of the high-frequency impedance the model of an azimuthally uniform beam [4]. This instability is called the microwave instability and it may have been observed in a number of accelerators [5, 6].

Neither of the viewpoints given above is convincing, since the question of the limits of applicability of one or another model can be solved only by analyzing the general system of equations for a bunched beam. In this paper this question is examined in application to the resonance impedance. It is shown that the nature of the instability near threshold is determined by two parameters: the ratio of the length of a bunch to the wavelength of the resonator and the relative spread in the values of the synchrotron frequency. If both parameters are small, then the multipole instability appears; if their product is very large, then the instability has a microwave character. In addition, there exists an intermediate zone, where the existing formulas are inapplicable. A criterion for instability that is convenient for numerical calculations is formulated for this zone.

2. Dispersion Equation

To describe the synchrotron oscillations of the particles we shall use two pairs of canonical variables:  $\{x, u\}$  and  $\{\mathcal{E}, \Psi\}$ . where  $x = \varphi_s - \varphi$  is the difference of the phases of the synchrotron and of an arbitrary particle relative to the accelerating field;  $u = p - p_s$  is the deviation of the particle momentum  $p$  from the synchrotron value  $p_s$ ;  $\mathcal{E}$  is the energy; and,  $\Psi$  is the phase of the synchrotron oscillations. In these variables the equations of motion have the following form [7]:

$$\begin{aligned} \dot{x} &= \frac{q\eta\omega_s}{p_s} u; \quad \dot{u} = -\frac{\Omega_0^2 p_s}{2q\eta\omega_s} U'(x); \\ \dot{\mathcal{E}} &= 0; \quad \dot{\Psi} = \Omega_c(\mathcal{E}), \end{aligned} \quad (1)$$

where  $\omega_s$  is the angular velocity of the synchrotron particles;  $q$  is the acceleration multiple;  $\eta = \alpha - \gamma^{-2}$ ;  $\alpha$  is the coefficient of expansion of the orbits;  $\gamma$  is the relativistic factor;  $\Omega_c(\mathcal{E})$  is the frequency of synchrotron oscillations; and,  $U(x)$  is the normalized potential.  $\Omega_0$  is equal to the frequency of the synchrotron oscillations of some characteristic particle

Translated from *Atomnaya Energiya*, Vol. 59, No. 1, pp. 42-48, July, 1985. Original article submitted February 9, 1984.

Declassified and Approved For Release 2013/02/20 : CIA-RDP10-02196R000300070001-4  
in a bunch. This factor is introduced for convenience and does not appear in the final formulas, since the function  $U(x)$  changes depending on its choice. If  $U(x) \rightarrow x^2$  when  $x \rightarrow 0$ , then  $\Omega_0$  coincides with the frequency of small synchrotron oscillations. The relationship between the variables is expressed with the help of the following formulas:

$$\mathcal{E}(x, u) = U(x) + (q\eta\omega_s u / \Omega_0 p_s)^2; \quad (2a)$$

$$\Psi(\mathcal{E}, x) = -\operatorname{sgn}(\eta u) \frac{\Omega_c(\mathcal{E})}{\Omega_0} \int_x^{x_{\max}} \frac{dx'}{\sqrt{\mathcal{E} - U(x')}}; \quad (2b)$$

$$|\Psi(\mathcal{E}, x_{\min})| = \pi, \quad (2c)$$

where  $x_{\max}(\mathcal{E})$  and  $x_{\min}(\mathcal{E})$  are the turning points of the phase trajectory of a particle with energy  $\mathcal{E}$ .

The electrodynamic properties of the vacuum chamber are characterized by the impedance matrix  $Z_{kj}(\omega)$ , which is introduced with the help of the relation

$$E_k(\omega) = -\frac{1}{L} \sum_{j=-\infty}^{\infty} Z_{kj}(\omega) J_j(\omega), \quad (3)$$

where  $E_k(\omega)$  are the corresponding amplitudes of the harmonics of the electric-field intensity; the beam current is represented as a sum of traveling waves of the form  $J_j(\omega) e^{i(j\theta - \omega t)}$  (here  $\theta$  is the generalized azimuth, and  $t$  is the time); and,  $L$  is the length of the accelerator. In solving stability problems, it is sufficient to include in the sum (3) the single term  $j = k$  [1]. If after this the notation  $\omega = k\omega_s + \Omega$ ;  $Z_{kk}(\omega) = Z_k(\Omega)$ ;  $J_k(\omega) = J_k(\Omega)$ , etc. is introduced, then instead of (3) we obtain

$$\tilde{E}_k(\Omega) = -\frac{1}{L} Z_k(\Omega) \tilde{J}_k(\Omega), \quad (4)$$

and  $\Omega$  is the frequency of oscillations of the current and field of the beam in the intrinsic coordinate system.

We shall study a beam consisting of  $M$  identical equidistant bunches. The starting distribution is stationary in the coordinate system of the beam, but the field  $\tilde{E}_k(\Omega)$  can generate nonstationary corrections to the current. Following [1], we obtain an infinite system of equations for these corrections:

$$R \tilde{J}_k(\Omega) = \sum_{l'=-\infty}^{\infty} Y_{kk'}(\Omega) \frac{Z_{k'}(\Omega)}{k'} \tilde{J}_{k'}(\Omega), \quad (5)$$

where  $k = n + \ell M$ ;  $\ell = 0, \pm 1, \dots$ ;  $k' = n + \ell' M \neq 0$ . The index  $n = 0, 1, \dots, M-1$  determines the difference in the phases of the oscillations of two neighboring bunches:  $\Delta\varphi = 2\pi n/M$ . The coefficient  $R$  has the dimensions of resistance:

$$R = \frac{\beta^2 \eta E}{e J_0} \left( \frac{\Delta p}{p_s} \right)^2, \quad (6)$$

where  $E$  is the total energy of the particles;  $\beta$  is the reduced velocity of the particles;  $J_0$  is the average beam current; and,  $\Delta p/p_s$  is the maximum spread of the momentum in the bunch. The quantities  $Y_{kk'}(\Omega)$  are the so-called dispersion integrals:

$$Y_{kk'}(\Omega) = -i \frac{\Omega_0}{\pi} \sum_{m=-\infty}^{\infty} m \int_0^\pi F'(\mathcal{E}) \frac{I_{mk}(\mathcal{E}) I_{mk'}^*(\mathcal{E})}{\Omega - m\Omega_c(\mathcal{E})} d\mathcal{E}; \quad (7)$$

$$I_{mk}(\mathcal{E}) = \frac{1}{2\pi} \int_{-\pi}^\pi e^{im\Psi + i\frac{h}{q}x(\mathcal{E}, \Psi)} d\Psi. \quad (8)$$

$$\int_0^{\infty} \frac{F(\mathcal{E})}{\Omega_c(\mathcal{E})} d\mathcal{E} = \frac{\mathcal{E}_0}{\Omega_0}, \quad (9)$$

where  $\mathcal{E}_0 = \left( \frac{q\eta\omega_s \Delta p}{\Omega_0 p_s} \right)^2$  is the maximum energy of the oscillations.

The values of  $\Omega$  for which the system (5) has a nontrivial solution are the possible frequency of the coherent oscillations of the beam. The oscillations are unstable for  $\text{Im } \Omega > 0$ .

Let us assume that the impedance of the chamber is determined by the narrow-band resonance element with a characteristic frequency  $\omega_{\text{res}}$  and a bandwidth  $\Delta\omega_{\text{res}} \ll M\omega_s$ . In addition, for the time being, we shall assume that

$$\omega_{\text{res}} - \frac{j}{2} M\omega_s \left| \gg \Delta\omega_{\text{res}}, \quad (10)$$

where  $j$  is an arbitrary integer. In reality (see the Appendix), the basic conclusions of this work also remain in force when the condition (10) is violated, as well as in the case when the impedance has somewhat narrower resonance bands.

Under the indicated assumptions, only term for which  $|k\omega_s| \approx \omega_{\text{res}}$  remains on the right side of (5), which leads to the dispersion equation

$$Y_{kh}(\Omega) = \frac{kR}{Z_h(\Omega)}, \quad k = n + Ml \approx \pm \frac{\omega_{\text{res}}}{\omega_s} \quad (11)$$

### 3. Fast Instability

The index  $m$  in the formula (7) is the multiple order number of the oscillations of the bunches:  $m = \pm 1$  are dipolar oscillations,  $m = \pm 2$  are quadrupolar oscillations, etc. In most published works, such oscillations were considered to be independent, i.e., only one term was taken into account in the series (7). The condition of applicability of this approximation is that the following inequalities must be satisfied simultaneously

$$|\text{Im } \Omega| \ll \Omega_0, \quad \frac{\Delta\Omega_c}{\Omega_0} \ll \left| \frac{\Omega_0}{\Omega} \right|, \quad (12)$$

where  $\Delta\Omega_c$  is the spread in the synchrotron frequencies.

We are interested in the opposite case, when a large number of multipoles is excited simultaneously in each bunch, for which one of the conditions (12) must be strongly violated. In this section, we shall examine oscillations with very large increment:

$$\text{Im } \Omega \gg \Omega_0. \quad (13)$$

We shall first put the formula (7) into a more convenient form. Using the relation

$$\sum_{m=-\infty}^{\infty} \frac{e^{im\varphi}}{m-x} = 2\pi i \frac{e^{ix\varphi}}{1-e^{2\pi i x}}, \quad 0 < \varphi < 2\pi, \quad (14)$$

from (7) and (8) we obtain

$$Y_{kh'}(\Omega) = \frac{k\eta\omega_s\Omega_0}{2\pi^2 p_s} \int_0^{\infty} \frac{F'(\mathcal{E})}{\Omega_c^2(\mathcal{E})} d\mathcal{E} \int_{-\pi}^{\pi} u(\mathcal{E}, \Psi) \times e^{i \frac{h}{\eta} x(\mathcal{E}, \Psi)} d\Psi \int_0^{\infty} e^{i \frac{\Omega\varphi}{\Omega_c(\mathcal{E})} - i \frac{h'}{\eta} x(\mathcal{E}, \Psi - \varphi)} d\varphi. \quad (15)$$

$$Y_{kh}(\Omega) \approx i \frac{k\eta\omega_s \Delta p}{\pi p_s} \int_{-\infty}^{\infty} \frac{G'(u) du}{\Omega + \frac{k\eta\omega_s}{p_s} u}, \quad (16)$$

where  $G(u)$  is the effective momentum distribution function:

$$G(u) = \frac{1}{2\pi \sqrt{\mathcal{E}_0}} \int_{-\infty}^{\infty} F[\mathcal{E}(x, u)] dx. \quad (17)$$

It satisfies the following normalization condition:

$$\int_{-\infty}^{\infty} G(u) du = \frac{\Delta p}{2}. \quad (18)$$

The dispersion equation describing the fast stability of a bunched beam follows from (6), (11), and (16):

$$1 = \frac{2ieJ_0 Z_h(\Omega)}{L \Delta p} \int_{-\infty}^{\infty} \frac{G'(u) du}{\Omega + \frac{k\eta\omega_s}{p_s} u}. \quad (19)$$

It coincides exactly with the dispersion equation of a uniform beam, which is formed with a uniform distribution of particles in the starting beam over the perimeter of the accelerator. Practically the same distribution can be obtained by switching off the accelerating field.

Equation (19) describes the propagation of charge-density waves  $\sim e^{i(k\theta - \omega t)}$ . The existence of such waves in a bunched beam is characteristic for the microwave instability. From here it follows that the fast instability, whose increment satisfies the condition (13), has a microwave character.

A similar result was obtained previously by a different method in [3]. It is asserted there, however, that the multipole instability transforms into the microwave instability only when

$$\text{Im } \Omega \gtrsim \Omega_0 \frac{|k|}{q} \sqrt{\mathcal{E}_0}.$$

As will be shown below, this assertion is incorrect and when the resonator frequency is high enough the oscillations can have a microwave character already at the threshold of instability.

#### 4. Instability near Threshold

We shall now study the case when a large number of multipoles are coupled by a strong violation of the second of the inequalities (12), i.e.,

$$\frac{\Delta\Omega_c}{\Omega_0} \gg \left| \frac{\Omega_0}{\Omega} \right|. \quad (20)$$

In addition, for the time being, we shall assume that

$$\frac{\beta\lambda}{\pi l_b} \ll 1, \quad (21)$$

where  $l_b$  is the length of a bunch;  $\lambda = 2\pi c/\omega_{\text{res}}$  is the wavelength of the radiation at the resonator frequency. Actually, it will be shown below that the conditions (20)-(21) follow from a single restriction on the frequency of the resonant element and the spread of the synchrotron frequencies.



Because of (21) the asymptotic estimate of the integrals (8) with large value of the argument can be used. Using for this purpose the method of stationary phase [8], it can be shown that the integrals become vanishingly small when  $\ell < \ell_m - \delta\ell_m$ , where  $\ell_m$  is the solution of the equation

$$\ell_m \frac{\Omega_0^2}{\Omega_c^2(\ell_m)} = \frac{q^2 m^2}{k^2}. \quad (22)$$

The quantity  $\delta\ell_m$  depends on the form of the potential well in the limit  $x \rightarrow 0$ , and for a well of the form  $C_{2n}x^{2n}$

$$\frac{\delta\ell_m}{\ell_m} \sim \left( \frac{C_{2n}q^{2n}}{k^{2n}\ell_m^{2n}} \right)^{\frac{1}{2n+1}} \left| 1 - 2 \frac{\ell_m \Omega_c'(\ell_m)}{\Omega_c(\ell_m)} \right|. \quad (23)$$

When  $\ell > \ell_m + \delta\ell_m$ , the same method gives

$$|I_{mh}(\ell)|^2 \approx \frac{q\Omega_c^2(\ell)}{\pi\Omega_0^2|k|} \left[ \frac{1}{|U_1'|} + \frac{1}{|U_2'|} + \frac{2 \sin \varphi_{mh}}{\sqrt{|U_1'| \cdot |U_2'|}} \right]; \quad (24)$$

$$\varphi_{mh} = \left| \frac{k}{q} (x_2 - x_1) \right| - |m(\psi_2 - \psi_1)|, \quad (25)$$

where  $\psi_i$  are the solutions of the equation

$$u(\ell, \psi_i) \pm \frac{p_s m \Omega_c(\ell)}{k \eta \omega_s} = 0 \quad (26)$$

and the notation  $x_i = x(\ell, \psi_i)$ ,  $U_i' = U'(x_i)$  is used. The meaning of these quantities is explained in Fig. 1.

For any potential well except a square well,  $\delta\ell_m$  approaches zero as the resonator frequency increases. Assuming that this frequency is very high, the definition (24) can be extended into the entire region  $\ell > \ell_m$  and it may be assumed that  $|I_{mh}(\ell)|^2 = 0$  when  $\ell < \ell_m$ . The error appearing in the final frequency of the resonator will be evaluated below.

We substitute (24) into (7), replace the lower limit of integration by  $\ell_m$ , and note that because of the presence of the resonant denominator, terms with numbers satisfying the inequality

$$\left| m - \frac{\Omega}{\Omega_0} \right| \ll \frac{\Omega \Delta \Omega_c}{2\Omega_0^2} \quad (27)$$

make a significant contribution to the sum. Under the condition (20) the number of terms is large, and each term is much smaller than the sum of the series. Therefore, in (24) the correction  $\sim \sin \varphi_{mh}$  can be dropped, since it is a rapidly oscillating function of  $m$ . The remaining quantities are virtually independent of  $m$ , which enables replacing the sum by an integral over  $dm$ . Next we change the order of integration and make the substitution

$$m = - \frac{k \eta \omega_s \tilde{u}}{p_s \Omega_c(\ell)}. \quad (28)$$

Changing the order of integration again, we obtain

$$Y_{kh}(\Omega) \approx \frac{iqk\omega_s^2 \eta | \eta |}{\pi^2 \Omega_0 p_s^2} \int_{-\infty}^{\infty} \frac{\tilde{u} d\tilde{u}}{\Omega_0 \frac{k \eta \omega_s}{p_s} \tilde{u}} \int_{\ell_0 \frac{\tilde{u}^2}{\Delta p^2}}^{\infty} F'(\ell) \left[ \frac{1}{|U_1'|} + \frac{1}{|U_2'|} \right] (\ell, \tilde{u}) d\ell. \quad (29)$$

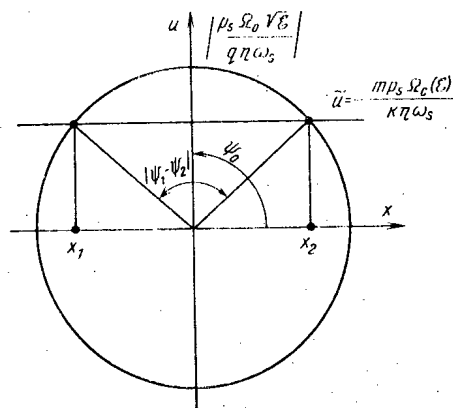


Fig. 1. The phase plane of synchrotron oscillations.

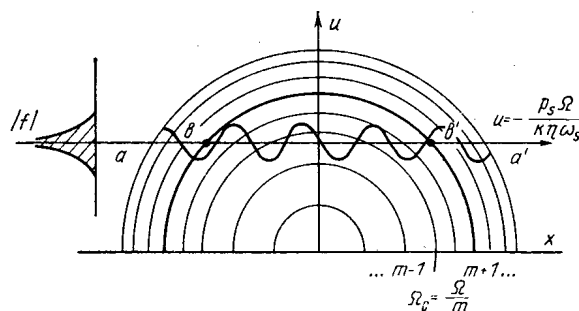


Fig. 2. Diagram clarifying the mechanism of the appearance of the microwave instability.

We note that the variable  $\tilde{u}$  can be interpreted as the momentum of a particle. The next natural step is to transform from integration over  $\mathcal{E}$  to integration over the variable  $x$ , which is determined with the help of (2a). Ultimately we again arrive at the formulas (16)-(17) and the microwave dispersion equation (19).

To clarify the physical meaning of the transformations performed above, we examine Fig. 2, which shows part of the phase plane of synchrotron oscillations. A systematic interaction of the particles with the electromagnetic wave occurs only along phase trajectories for which the resonance condition  $\Omega_c = \Omega/m$  holds. A formal reflection of this fact is the presence of resonant denominators in the dispersion integral (7). In this case the momentum of each particle changes primarily at the point of intersection of the straight line  $aa'$ , on which the particle velocity equal to  $\eta\omega_s u/p_s$  coincides with the phase velocity of the wave  $\Omega/k$ . This circumstance is reflected in the formula (24). The total change in the particle momentum over the period of synchrotron oscillations depends on the increase in the phase of the wave between the intersections  $b$  and  $b'$ . This quantity can differ substantially even for neighboring phase trajectories, which leads to the appearance of an oscillating term  $\sim \sin \varphi_{mh}$  in the formula (24). When averaged over several neighboring phase trajectories, however, these oscillations vanish. Ultimately, a disturbance of the phase density of the plane-wave type, repeating the structure of the electromagnetic wave, appears along the line  $aa'$ . Away from the line  $aa'$  the structure gradually breaks down, since the disturbance moves along different phase trajectories with different velocities.

## 5. Stability Criterion for Microwave Oscillations

To determine the threshold of the microwave instability with the help of the dispersion equation (19), we shall use the well-known method of threshold diagrams.

The function  $Y_{kk}(\Omega)$ , defined by (16), maps the upper half-plane of the complex variable  $\Omega$  onto part of the complex  $Y$  plane, bounded by the threshold curve  $C$ . The threshold curve is a mapping of the line  $\text{Im } \Omega \rightarrow +0$ , and its parametric equation has the form

$$\begin{aligned} \operatorname{Re} Y^{(c)} &= -\operatorname{sgn} \Omega \Delta p G'(u_\Omega), \\ \operatorname{Im} Y^{(c)} &= -p.v. \frac{\Delta p}{\pi} \int_{-\infty}^{\infty} \frac{G'(u) du}{u_\Omega - u}, \end{aligned} \quad (30)$$

where  $u_\Omega = |\Omega p_s / k \eta \omega_s|$  and p. v. is the principal value of the integral.

We draw on this plane the point  $Y^{(k)} = kR/Z_k$ . The stability of the system requires that this point be located outside the region bounded by the line C.

As an example we shall study the momentum distribution:

$$G(u) = \frac{4}{3\pi} \left(1 - \frac{u^2}{\Delta p^2}\right)^{3/2}, \quad |u| < \Delta p. \quad (31)$$

In the case of linear synchrotron oscillations it corresponds to a linearly decreasing distribution function over  $\mathcal{E}$ . Using (30), we obtain the result shown in Fig. 3. The threshold curve is a circle with radius  $2/\pi$  cut along the positive part of the imaginary axis. In the case A the system is stable, while in the case B it is unstable. Therefore, for the distribution (31) the stability condition has the form

$$\left| \frac{kR}{Z_k} \right| > \frac{2}{\pi}. \quad (32)$$

The method examined above assumes that  $Z_k$  is essentially independent of  $\Omega$ , in order to avoid uncertainty of the left side of (32). In order to make this condition more precise, we note that the diagram in Fig. 3 is circumvented with the variable  $|\Omega|$  varying in the limits of  $|\eta \omega_{\text{res}} \Delta p / p_s|$ . The displacement of the point  $Y^{(k)}$  can be neglected if  $|\Omega| \ll \Delta \omega_{\text{res}}$ , which gives

$$\frac{\Delta \omega_{\text{res}}}{\omega_{\text{res}}} \gg \left| \eta \frac{\Delta p}{p_s} \right| \quad \text{or} \quad Q \ll \left| \eta \frac{\Delta p}{p_s} \right|^{-1}, \quad (33)$$

where  $Q$  is the quality factor. In practice, this restriction can be significant only for the interaction of a beam with the accelerating resonator at its fundamental frequency [1].

The criterion (32) can be simplified by making use of the resonant character of the impedance. For this we note that  $Z_k^{-1}(\Omega)$  is the conductivity of the resonator at the frequency  $k\omega_s + \Omega$ . When the index  $k$  varies, the real part of the conductivity remains virtually constant, i.e., the point  $Y^{(k)}$  moves parallel to the imaginary axis (the lines  $aa'$ ,  $bb'$  in Fig. 3). The distance from this line to the imaginary axis can be expressed in terms of the coupling resistance of the resonator  $R_c = |\operatorname{Re} Z_k^{-1}|^{-1}$ , which leads to the following stability condition:

$$\frac{\omega_{\text{res}}}{\omega_s} \frac{|R|}{R_c} > \Lambda, \quad (34)$$

$$\Lambda = \max |\Delta p G'(u_\Omega)|. \quad (35)$$

For all distributions of practical interest, the factor  $\Lambda$  is close to 1. Thus in the case (31)  $\Lambda = 2/\pi \approx 0.64$ . As a second example, we study the distribution over the energy of the synchrotron oscillations consisting of two conjugate parabolas and shown schematically in Fig. 4. Using the definition (17) and the approximation of linear synchrotron oscillations, we construct the function  $G(u)$  and then find the dependence  $\Lambda(a)$ , also shown in Fig. 4, from the formula (35). It is evident that the factor  $\Lambda$  falls in the range 0.7-0.9.

Using the criteria (32) and (34), one must keep in mind the resonant condition  $\omega_{\text{res}} \approx |k\omega_s|$ , without which the starting dispersion equation (11) breaks down. This restriction becomes insignificant when the band width of the resonator satisfies the inequalities

$$\omega_s \ll \Delta \omega_{\text{res}} \ll M \omega_s, \quad (36)$$

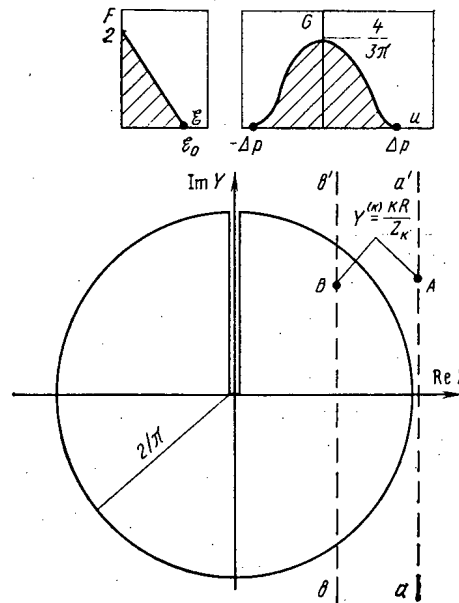


Fig. 3. Threshold diagram for a "triangular" distribution over the energy of synchrotron oscillations.

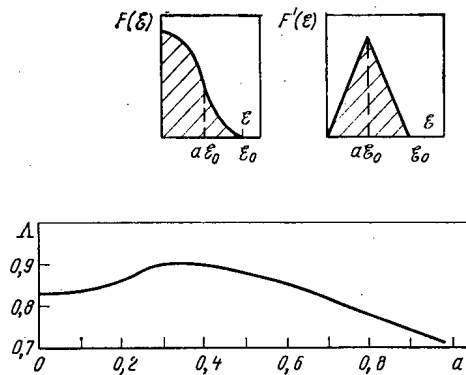


Fig. 4. The parameter  $\Lambda$  for the "parabolic" distribution over the energy of synchrotron oscillations.

since in this case the mode of oscillations for which the resonant condition holds will necessarily be found. For large accelerators with a large number of bunches, the inequalities (36) are entirely realistic. If the left part of the inequality is still violated, then the stability of the beam can in principle be guaranteed by a substantial detuning of the resonator. In this case, the criterion (34) remains in force as a sufficient condition for stability.

#### 6. Conclusions. Limits of Applicability of Different Models

In this section we shall restrict our attention to the most important practical case of weak nonlinearity:  $\Delta\Omega_c/\Omega_0 \leq 0.2-0.3$ .

From the formulas (6) and (34) we can obtain the criterion of beam stability in the explicit form:

$$R_c J_0 \frac{\omega_s}{\omega_{\text{res}}} < \frac{\beta^2 E |\eta|}{\Lambda e} \left( \frac{\Delta p}{p_s} \right)^2. \quad (37)$$

It is important to underscore that for resonance impedance, satisfying the conditions (10) and (36), the formula (37) holds independently of the other assumptions, if the exact dispersion integral (7) is used to find  $\Lambda$ :

$$\Lambda = \max |\operatorname{Re} Y_{kh}(\Omega)| = \max \left| \Omega_0 \sum_m \frac{F'(\tilde{\varepsilon}_m)}{|\Omega_c'(\tilde{\varepsilon}_m)|} |I_{mh}(\tilde{\varepsilon}_m)|^2 \right|, \quad (38)$$

where  $\tilde{\varepsilon}_m$  is the solution of the equation

$$m\Omega_c(\tilde{\varepsilon}_m) = \Omega. \quad (39)$$

It is evident that terms with the same sign of  $m$  contribute to the sum. For definiteness, we assume below that  $m > 0$ . The approximate value of  $\Lambda$  which is found from the formula (35) differs from the exact value for two reasons: because of the use of the asymptotic formula (24) without the oscillating term and because of the replacement of the sum over  $m$  by an integral. We shall evaluate the corresponding errors.

We shall first evaluate more accurately the integral (8) at  $\varepsilon \approx \tilde{\varepsilon}_m$ , for which we expand the exponent of the exponential in a series in powers of  $\Psi$  near the point  $\Psi_0$  (see Fig. 1), retaining the linear and the first nonvanishing terms. The result will depend on the form of the potential well in the limit  $x \rightarrow 0$ . If  $U(x) \rightarrow x^2$ , then the integral is expressed in terms of the Airy function [8]:

$$|I_{mh}(\varepsilon)|^2 \approx \left| \frac{4q^2}{k^2\varepsilon} \right|^{1/3} \frac{\Omega_c^2(\varepsilon)}{\Omega_0^2} \operatorname{Ai}^2 \left[ \left( \frac{2k^2\varepsilon}{q^2} \right)^{1/3} \left( \frac{\Omega_c(\varepsilon)}{\Omega_c(\tilde{\varepsilon}_m)} \frac{\sqrt{\varepsilon_m}}{\sqrt{\varepsilon}} - 1 \right) \right]. \quad (40)$$

Using the fact that  $\max \operatorname{Ai}^2(z) \approx \operatorname{Ai}^2(-1) \approx 0.29$ , we find maximum contribution of the  $m$ -th term to the series (38):

$$\Lambda_m \leq 0.5 \frac{\Omega_0}{\Delta\Omega_c} |\varepsilon_0 F'(\tilde{\varepsilon}_m)| \left( \frac{q^2}{k^2\varepsilon_m} \right)^{1/3}, \quad (41)$$

and in addition the maximum is reached if

$$\varepsilon_m \approx \tilde{\varepsilon}_m \approx \frac{q^2 m^2}{k^2}. \quad (42)$$

With the help of (41) and (42) we can find the index of the multipole making the maximum contribution to  $\Lambda$ . For definiteness, we shall make use of the quite realistic parabolic distribution shown in Fig. 4 with  $a = 0.5$ . As a result, we obtain

$$m_0 \approx 0.7 \frac{\pi l_{cr}}{\beta\lambda}; \quad \Lambda_{m_0} \approx 2.5 \frac{\Omega_0}{\Delta\Omega_c} \left( \frac{\beta\lambda}{\pi l_{cr}} \right)^{2/3}. \quad (43)$$

Therefore, the sum (38) reaches its maximum value for  $|\Omega| \approx m_0 \Omega_0$ , the term with index  $m_0$  makes the maximum contribution, and the total number of terms is equal to

$$\Delta m \approx m_0 \frac{\Delta\Omega_c}{\Omega_0} \approx 0.7 \frac{\pi l_{cr}}{\beta\lambda} \frac{\Delta\Omega_c}{\Omega_0}. \quad (44)$$

Starting from this, we can construct the overall picture of the oscillations of the beam near the threshold of instability. If

$$\frac{\Delta\Omega_c}{\Omega_0} \leq 3 \frac{\beta\lambda}{\pi l_{cr}}, \quad (45)$$

then an instability of a separate multipole appears. In this case, the series (38) contains one term, which must be substituted into the stability criterion (37). If  $\beta\lambda/\pi l_{cr} \leq 0.7$ ,

ther. Declassified and Approved For Release 2013/02/20 : CIA-RDP10-02196R000300070001-4 (45)  
refines the second of the inequalities (12), which was used above as the condition of applicability of the approximation of separated multipoles.

We note that in the region of separated multipoles the representation  $|I_{mk}(\xi)| = |J_m \frac{k}{q} V \bar{\xi}|$ , where  $J_m$  is a Bessel function, is admissible. This leads to the following result:

$$\Lambda = \max_{m>0, \xi>0} \frac{\Omega_0 |F'(\xi)|}{|\Omega_c'(\xi)|} J_m^2 \left( \frac{|k|}{q} V \bar{\xi} \right). \quad (46)$$

However, when several multipoles are excited simultaneously this representation can strongly distort the result. If

$$\frac{\Delta\Omega_c}{\Omega_0} \gg \frac{\beta\lambda}{\pi l_{cr}}, \quad (47)$$

then the series (38) contains a large number of terms, and the sum can be replaced by an integral, which leads to the microwave dispersion equation and the formula (35) for  $\Lambda$ . In this case, the expression (43) determines the maximum value of a separate term and thus gives an estimate of the error of the result:

$$\delta\Lambda \sim \frac{\Omega_0}{\Delta\Omega_c} \left( \frac{\beta\lambda}{\pi l_{cr}} \right)^{2/3}. \quad (48)$$

Formula (47) refines the microwave condition (20), which was used above. Inequality (21) follows from it automatically also.

If neither of the inequalities (45) and (47) holds, then the series (38) contains a relatively small number of terms, i.e., coupled oscillations of several multipoles with indices close to  $m_0$  appear. The calculation of the threshold requires the general formula (38), which in this case cannot be simplified.

The study of other representations leads to analogous results, though the number of coefficients can change somewhat. In this case, it is significant that all real distribution functions satisfy the condition  $F'(0) = 0$ . The role of this condition can be clarified for the example of the distribution  $F'(\xi) = -\frac{2}{\xi_0}$ , for which the formulas (41)-(42) give

$$\max \Lambda_m \approx \frac{1}{m^{2/3}} \frac{\Omega_0}{\Delta\Omega_c}. \quad (49)$$

Therefore, the term  $m = 1$  dominates in the sum (38), and the maximum is reached at  $|\Omega| = \Omega_0$ , which gives  $\Lambda = \Omega_0/\Delta\Omega_c$ . Thus the instability begins with dipolar oscillations of the bunch. Microwave oscillations cannot appear, because the condition (20) does not hold. Increasing the resonator frequency leads to the fact that the excitation of the bunch, remaining dipolar, is pulled toward its center. At very high frequencies, only the central core oscillates, while the periphery of the bunch remains almost stationary.

It is evident from the formula (43) and the subsequent analysis that when the frequency of the resonator is increased the factor  $\Lambda$  decreases and approaches the microwave limit (35), if  $\beta\lambda/\pi l_{cr} \ll 1$ . In other words, the beam is most stable in the microwave zone. This assertion follows in a more general form from the results examined in Secs. 3 and 5. We present the main idea of the proof without details. The threshold curve C [see (30)], generally speaking, encompasses the region of strong instability, since the latter is described by Eq. (19). The full region of instability, of course, is wider and both regions coincide only in the microwave limit.

In conclusion, we shall evaluate the error in the calculation of the microwave value of  $\Lambda$  associated with the use of the formula (24) near the resonance point (see Fig. 2). At this point the conditions (22) and (39) must be satisfied simultaneously. Taking into account (23) also, it is evident that in calculating  $\Lambda$  with the help of (24) terms lying in the interval  $|m - m_0| < \delta m_0$ , where

$$\Omega = \frac{|k|}{q} \Omega_c(\xi_\Omega) \sqrt{\xi_\Omega}, \quad m_\Omega \approx \frac{|k|}{q} \sqrt{\xi_\Omega},$$

$$\delta m_\Omega \sim \frac{|\Omega'_c(\xi_\Omega)| \xi_\Omega}{\Omega_0} \left| \frac{k}{q} \sqrt{\xi_\Omega} \right|^{1/3}, \quad (50)$$

give the largest error. Now, using the formulas (24) and (40), we can find the correction to  $\Lambda$ :

$$\delta \Lambda \approx \frac{\Omega_0 |F'(\xi_\Omega)|}{|\Omega'_c(\xi_\Omega)|} \left[ 2 |I_{m\Omega k}(\xi_\Omega)|^2_{(30)} \delta m_\Omega - \int_{m_\Omega}^{m_\Omega + \delta m_\Omega} |I_{mk}(\tilde{\xi}_m)|^2_{(24)} dm \right], \quad (51)$$

where  $m$  and  $\tilde{\xi}_m$  are related by the relation (39). A calculation leads to

$$\delta \Lambda \sim \left( \frac{\beta \lambda}{\pi l_{cr}} \right)^{1/3}. \quad (52)$$

In the microwave zone, where the condition (47) holds, this error is, for all practical purposes, negligible.

#### APPENDIX

We shall study a chamber whose impedance is determined by several narrow-band resonant elements with approximately the same coupling resistances. First of all, it is clear that there is no mutual effect of elements if their resonant frequencies satisfy the conditions

$$|\omega_i - \omega_j - l M \omega_s| \gg \Delta \omega_i + \Delta \omega_j, \quad (A1)$$

where  $l$  is an arbitrary integer. The resonant terms not satisfying (A1) must be examined simultaneously. In this case, the dispersion equation has the form

$$\det \left\| R \delta_{kk'} - \frac{Z_{kk'}(\Omega)}{k'} Y_{kk'}(\Omega) \right\| = 0. \quad (A2)$$

A calculation of the matrix elements using the procedure described in Sec. 3 leads to the following result:

$$Y_{kk'}(\Omega) \approx i \frac{k \eta \omega_s \Delta p}{\pi p_s} \int_{-\infty}^{\infty} \frac{G'_{k-k'}(u) du}{\Omega + \frac{k' \eta \omega_s}{p_s} u}; \quad (A3)$$

$$G_k(u) = \frac{1}{2\pi \sqrt{\xi_0}} \int_{-\infty}^{\infty} F[\xi(x, u)] \exp\left(i \frac{k}{q} x\right) dx. \quad (A4)$$

This gives an estimate of the relative value of the matrix elements:

$$\left| \frac{Y_{kk'}}{Y_{kk}} \right| \sim \frac{q}{|k-k'| x_{\max}}, \quad k \neq k'. \quad (A5)$$

If this value is small, then the nondiagonal matrix elements can be neglected, which reduces (A2) to dispersion equation in the text (10). A calculation in the near threshold region using the procedure examined in Sec. 4 leads to the same conclusion.

Next, we take into account the fact that only the matrix elements with indices  $k_j \approx \pm \omega_j / \omega_s$  are actually different from zero. This leads to the following condition of applicability of the results obtained: for each resonant frequency and for each pair of frequencies the relations

$$\omega_j \gg \frac{v}{l_{cr}}, \quad |\omega_i - \omega_j| \gg \frac{v}{l_{cr}},$$

(A6)

the first of which coincides with the microwave condition (21), must hold.

## LITERATURE CITED

1. A. N. Lebedev, "Coherent synchrotron oscillations in the presence of space charge," *At. Energ.*, **25**, No. 2, 100-104 (1968).
2. F. Sacherer, *IEEE Trans. Nucl. Sci.*, **NS-20**, 825 (1973).
3. P. T. Pashkov and A. V. Smirnov, "Longitudinal short-wavelength instability of proton bunches interacting with the resonator," *At. Energ.*, **50**, No. 6, 480-412 (1981).
4. D. Boussard, CERN LAB II/RF/Int 75-2 (1975).
5. G. G. Gurov, Preprint No. 80-109, Institute of High Energy Physics (1980).
6. D. Boussard et al., *IEEE Trans. Nucl. Sci.*, **NS-24**, 1399 (1977).
7. A. A. Kolomenskii and A. N. Lebedev, *Theory of Cyclical Accelerators* [in Russian], Fizmatgiz, Moscow (1962).
8. E. T. Copson, *Asymptotic Expansions*, Cambridge Univ., Press (1965).

# CALCULATION OF THE EFFECTS OF NEUTRON ACTIVATION OF NUCLEI FOR CASES OF SUPERPOSITION OF THE SIGNAL IN GAMMA ACTIVATION ANALYSIS

A. P. Ganzha, M. G. Davydov,  
É. M. Davydov, and É. M. Shomurodov

UDC 543.0

When a sample is activated by bremsstrahlung from an electron accelerator, the photonuclear  $[{}_ZA(\gamma, x)C]$  and neutron  $[{}_ZB(n, y)C]$  reactions on isotopes of a single element  $Z$  can form the same radionuclides  $C$ . The analytical signal in the spectrum of the gamma radiation of the activated sample will be formed by the superposition of signals from the radiation of radionuclides - products of  $\gamma$  and neutron activation. This signal amplification effect must be taken into account in  $\gamma$  activation analysis when selecting the optimum energy of the bremsstrahlung spectrum  $E_{\gamma m}$ . In calculating the effect, the activation from both the background photoneutrons of the accelerator ("external") and from photoneutrons formed inside the sample itself ("internal") must be taken into account. The calculation for different pairs of reactions  $(\gamma, \gamma')-(n, n')$ ,  $(\gamma, n)-(n, 2n)$ ,  $(\gamma, n)-(n, \gamma)$  and others is similar, though in each case it has peculiarities which are determined by the energy dependence of the reaction cross sections.

For definiteness, we shall study the proposed method for calculating the contribution of neutron activation to the analytical signal for the pair of reactions  $(\gamma, \gamma')$ , which is of special interest for  $\gamma$  activation analysis. In spite of the relatively small cross sections of the reactions  $(\gamma, \gamma')$ , they in many cases make it possible to develop exceedingly selective and fast methods for experimentally determining commercially valuable elements in samples with a complicated composition [1, 2]. The prospects for the exploitation of the reactions  $(\gamma, \gamma')$  in  $\gamma$  activation analysis is demonstrated, for example, in [3-8]. In addition, the neutron activation effect under study must be especially significant in this case because of the peculiarities of the cross sections of the reactions  $(\gamma, \gamma')$  and  $(n, n')$ .

The yield of nuclei in the isomeric state with activation of a sample in a real bremsstrahlung beam from an electron accelerator (with an admixture of internal and external photoneutrons) will contain three components which depend differently on  $E_{\gamma m}$ .

The first component is determined by the cross section  $\sigma_{\gamma, \gamma'}$  of the reaction  $(\gamma, \gamma')$  on nuclei of the sample under study. If the bremsstrahlung spectrum is described by the product of the integrated spectrum  $W(E_{\gamma}, E_{\gamma m})$  [9] and the angular distribution of the bremsstrahlung [10], then the expression for the yield of the photonuclear reaction can be written in the form [11]

Translated from *Atomnaya Énergiya*, Vol. 59, No. 1, pp. 49-52, July, 1985. Original article submitted February 13, 1984.



$$Y_{\gamma, \gamma'}(E_{\gamma m}) = \alpha_1 D(E_{\gamma m}) Q(E_{\gamma m}, 0) \times \int_{E_n^{\gamma, \gamma'}} \sigma_{\gamma, \gamma'}(E_{\gamma}) W(E_{\gamma}, E_{\gamma m}) dE_{\gamma}, \quad (1)$$

where  $\alpha_1$  is the coefficient of proportionality;  $D(E_{\gamma m})$  is a function describing the dependence of the bremsstrahlung dose on  $E_{\gamma m}$ ;  $Q$  is a function determining the relative fraction of the average intensity of the bremsstrahlung on the sample, subtending an angle  $2\theta$ , relative to the intensity at the center of the sample; and,  $E_n^{\gamma, \gamma'}$  is the threshold of the reaction  $(\gamma, \gamma')$ .

The second component depends on the cross section  $\sigma_{n, n'}$  of the reaction  $(n, n')$  on the nuclei of the sample under study, the normalized spectrum of the background photoneutrons of the accelerator  $f_p(E_n, E_{\gamma m})$ , and their flux  $Y_p$  and is proportional to the yield of the reaction  $(n, n')$  from the sample, owing to the background photoneutrons:

$$Y_{n, n'}^p(E_{\gamma m}) = \alpha_2 Y_p(E_{\gamma m}) \int_{E_n^{n, n'}}^{E_n \max} f_p(E_n, E_{\gamma m}) \sigma_{n, n'}(E_n) dE_n, \quad (2)$$

where  $\alpha_2$  is the coefficient of proportionality;  $E_n$  is the energy of the neutrons,  $E_n \max$  is the maximum energy of the background-photoneutron spectrum; and,  $E_n^{n, n'}$  is the threshold of the reaction  $(n, n')$ . A Maxwellian spectrum with an effective temperature  $\bar{T}(E_{\gamma m})$  is adopted for the spectrum of the fast background photoneutrons:

$$f_p(E_n, E_{\gamma m}) = k E_n \exp[-E_n / \bar{T}(E_{\gamma m})] / \bar{T}^2(E_{\gamma m}). \quad (3)$$

The third component is determined by the cross section  $\sigma_{n, n'}$  of the reaction  $(n, n')$  on nuclei of the sample under study, the normalized spectrum of the photoneutrons  $f_i(E_n, E_{\gamma m})$  of nuclei of the  $i$ -th type in the sample, and their yields  $Y_i(E_{\gamma m})$ , and is proportional to the yield of the reaction  $(n, n')$  from the sample owing to photoneutrons formed in the sample itself:

$$Y_{n, n'}^o(E_{\gamma m}) = \alpha_3 \int_{E_n^{n, n'}}^{E_n \max} \sigma_{n, n'}(E_n) \sum_{i=1}^h Y_i(E_{\gamma m}) f_i(E_n, E_{\gamma m}) dE_n \int_V \int_{V'} \frac{\vartheta(x', y')}{r^2} dV dV', \quad (4)$$

where  $\alpha_3$  is the coefficient of proportionality;  $V$  and  $V'$  are the volumes of integration over the sample;  $\vartheta(x', y')$  is a function describing the distribution of the intensity of the bremsstrahlung over the surface of the sample;  $r^2 = (x - x')^2 + (y - y')^2 + (z - z')^2$  is the square of the distance between the elementary volumes  $dV$  and  $dV'$  with the coordinates  $(x, y, z)$  and  $(x', y', z')$ , respectively. Writing  $r'^2 = x'^2 + y'^2$  and using  $\vartheta(\theta)$  from [12], we obtain

$$\vartheta(r') = 2\pi r' G / \left[ 1 + \left( \frac{E_{\gamma m} + m_0 c^2}{m_0 c^2} \operatorname{arctg} \frac{r'}{L} \right)^2 \right]^2, \quad (5)$$

where  $G$  is a normalization constant and  $L$  is the distance from the bremsstrahlung target to the sample. The yields of photoneutrons on the nuclei of the sample  $Y_i(E_{\gamma m})$  are calculated in a manner analogous to the calculation of the yield  $Y_{\gamma, \gamma'}(E_{\gamma m})$  from relation (1).

The internal photoneutron spectra  $f_i(E_n, E_{\gamma m})$  were calculated using the method described in the monograph [12]. We assumed that this spectrum consists of two parts: the evaporative Maxwellian part  $f_{iM}$  with the corresponding value  $\bar{T}(E_{\gamma m})$  and a part corresponding to the contribution of direct processes  $f_{in}$ ; in addition, the relative fraction of neutrons from the direct processes  $\alpha_i$  was assumed to be independent of  $E_{\gamma m}$ . The values of  $\alpha_i$  are taken from [12]. The form of the photoneutron spectrum from direct processes, as in [12], was approximated in accordance with Wilkinson's model

$$f_{in}(E_n) = \beta_i W(B_i + E_n, E_{ym}) \sigma_{i\gamma, n}(B_i + E_n),$$

(6)

where  $\beta_i$  is a normalization constant;  $B_i$  is the binding energy of the first neutron in the  $i$ -th nucleus; and,  $E_n$  is the instantaneous neutron energy. The full spectrum of internal photoneutrons of nuclei of the  $i$ -th type in the sample is

$$f_i(E_n, E_{ym}) = \left\{ \frac{1}{1+\alpha_i} \frac{E_n}{\bar{T}_i^2(E_{ym})} \exp[-E_n/\bar{T}_i(E_{ym})] + \frac{\alpha_i}{1+\alpha_i} f_{in} \right\}. \quad (7)$$

With an energy  $E_{ym} > 18$ -20 MeV neutrons formed in the reactions  $(n, n')$  on nuclei in the sample will make increasingly larger contributions to the yield of the reaction  $(\gamma, 2n)$  from the internal photoneutrons. Including the contribution of this reaction, the yield of the reaction  $(n, n')$  is

$$Y_{n, n'}^0 = \alpha_3 \int_{E_n^{n, n'}}^{E_{n, \max}} \sigma_{n, n'}(E_n) \sum_{i=1}^k [Y_i^{\gamma, n} f_{in}(E_n, E_{ym}) + 2Y_i^{\gamma, 2n} f_{i2n}(E_n, E_{ym})] dE_n \int_V \int_{V'} \delta(x', y')/r^2 dV dV'. \quad (8)$$

The calculation of the yield  $Y_i^{\gamma, 2n}$  is analogous to the calculation of  $Y_{\gamma, \gamma'}$  and  $Y_i^{\gamma, n}$ , and the spectra of photoneutrons  $f_{i2n}(E_n, E_{ym})$  from the reaction  $(\gamma, 2n)$  are calculated by the method described in [12].

It is obvious that the contributions of the second and third components of the yield of the isomeric state, i.e., the contribution of the activation of these states, owing to the reaction  $(n, n')$  from external and internal photoneutrons, will grow rapidly with  $E_{ym}$  when  $E_{ym} > E_{n, n'}^{\gamma, n}$ . Since the thresholds  $E_{n, n'}^{\gamma, n}$  of the reactions  $(n, n')$  are low, the cross sections  $\sigma_{n, n'}$ , as a rule, are substantially higher than  $\sigma_{\gamma, \gamma'}$ , and the photoneutron (internal and external) spectra become increasingly "harder" as  $E_{ym}$  increases, the contribution of neutron activation with respect to photoactivation of the isomer will increase rapidly with  $E_{ym}$  and can be very substantial at an energy of  $E_{ym} = 20$ -25 MeV.

To check the validity of the proposed method for calculating the  $E_{ym}$  dependence of the contributions of neutron activation of isomeric states of nuclei to photoactivation of these states by bremsstrahlung from electron accelerators, as a model variant we selected activation of the isomeric state of the  $^{115}\text{In}$  nucleus in the bremsstrahlung beam from the B-25/30 betatron. For this case,  $Y_{n, n'}^p$ ,  $Y_{n, n'}^0$ , and  $Y_{\gamma, n}$  were calculated numerically for values of  $E_{ym}$  equal to 10, 13, 16, 19, and 22 MeV. The quantity  $Y_{n, n'}^p$  was calculated using the relations (1) and (2) for  $L = 25$  cm, a sample radius  $r_0 = 1.5$  cm, and sample thickness  $t = 0.2$  cm. The data on the dependence of the cross section of the reaction  $(n, n')$  on the energy of the neutrons  $\sigma_{n, n'}(E_n)$  are taken from the handbook [13] and were supplemented by new data provided by the Center of Neutron Data of FÉI.

The dependence of the effective temperature of the nucleus  $\bar{T}$  on  $E_{ym}$ , required for calculating the background photoneutron spectrum using the formula (3), is obtained as follows. According to the data of [14], the experimentally determined spectra of the background photoneutrons of the betatron have a form which is typical for the spectrum of photoneutrons of a separate nucleus. The form of the spectrum is close to Maxwellian with  $\bar{T} = 1.3$  MeV at  $E_{ym} = 25$  MeV (if the presence of fast-neutron peaks on the high-energy side of the spectrum is ignored). Keeping in mind the monotonic dependences of the effective temperature in the photoneutron spectra of separate nuclei  $\bar{T}(A)$  for fixed  $E_{ym}$  (see the calculations in [15]) as well as the low sensitivity of the spectra to a change in the cross sections of photoneutron reactions, it may be assumed that the spectrum of the background photoneutrons of the accelerator will be similar (equivalent) to the spectrum of photoneutrons for nuclei with a value of  $A$  for which with fixed  $E_{ym}$  the value of  $\bar{T}$  will be equal to the experimental value. The experimentally obtained value  $\bar{T} = 1.3$  MeV for  $E_{ym} = 25$  MeV is close to  $\bar{T}$  obtained by the calculation in [15] for the  $^{59}\text{Co}$  nucleus. It may therefore be assumed that  $^{59}\text{Co}$  is an acceptable equivalent for describing the dependence  $\bar{T}(E_{ym})$  of background fast photoneutrons of the betatron, and the dependence  $\bar{T}(E_{ym})$  obtained in [15] for this nucleus can be used in our calculations.

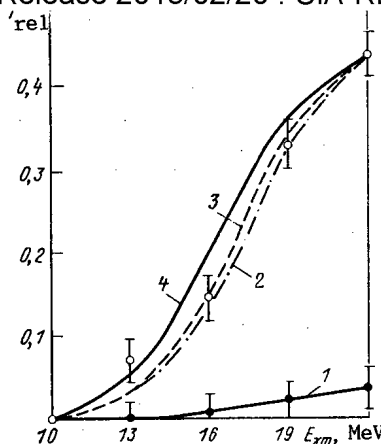


Fig. 1. Dependence of the relative yield of the isomer  $^{115m}\text{In}$  formed in the reactions  $(n, n')$  on the maximum energy of the bremsstrahlung  $E_{\gamma m}$ . The yield  $Y_{n,n}^p$ , owing to the background photoneutrons of the accelerator (external): 1) the calculation; 2) the experimental values. The yield  $Y_{n,n}^0$  owing to photoneutrons formed in the sample itself (internal): 2) calculation taking into account the spectra of photoneutrons from the reactions  $(\gamma, n)$  and  $(\gamma, 2n)$ ; 3) calculation taking into account the spectra of photoneutrons from the reaction  $(\gamma, n)$ ; 4) calculation ignoring the photoneutron spectra; o) the experimental points.

The yield of fast background photoneutrons  $Y_p(E_{\gamma m})$  for the B-25/30 betatron as a function of  $E_{\gamma m}$  was obtained previously in separate measurements for  $L = 25$  cm with  $E_{\gamma m} = 25$  MeV (the dosage was 0.7 A/kg). The yield of background photoneutrons of the electron accelerator in the expression (2) was assumed to be independent of the angle, since within the range of angles  $\theta \leq 30^\circ$  relative to the orientation of the axis of the bremsstrahlung beam the yield of background photoneutrons may be assumed to be isotropic [16].

The yield  $Y_{n,n}^0(E_{\gamma m})$  for the activation of  $^{115m}\text{In}$  from internal photoneutrons of indium was calculated using the relations (1), (4), and (8) for the same geometry. The yield of internal neutrons of the indium sample  $Y_n(E_{\gamma m})$  was obtained from the relation (1) using data on the cross sections of photoneutron reactions  $\sigma_{\gamma,n}$  and  $\sigma_{\gamma,2n}$  for  $^{115}\text{In}$  [17]. In calculating the internal photoneutron spectra it was assumed that the contribution of the direct processes  $\alpha = 0.11 \pm 0.01$  [12]. The dependence  $\bar{T}(E_{\gamma m})$  for the evaporative part of the photoneutron spectrum in  $(\gamma, n)$  and  $(\gamma, 2n)$  reactions on  $^{115}\text{In}$  was calculated by the method described in [12].

The final results of the calculation of the yields  $Y_{n,n}^0$  and  $Y_{n,n}^p$ , normalized at  $E_{\gamma m} = 22$  MeV, of neutron-activated  $^{115m}\text{In}$  are presented in Fig. 1. The figure also shows the experimentally obtained results. In the calculation of  $Y_{n,n}^0$ , the spectra included photoneutrons from the reactions  $(\gamma, n)$  and  $(\gamma, 2n)$ , i.e.,  $Y_{n,n}^p$ ,  $(\gamma, 2n)$ , and only the reactions  $(\gamma, n)$ , i.e.,  $Y_{n,n}^p$ ,  $(\gamma, n)$ . In addition, to compare the energy dependence of the neutron-activation yields, the curve of the yield of photoneutrons  $Y_{\gamma,n}^p$  from  $^{115}\text{In}$  was also calculated.

The yields  $Y_{\gamma,\gamma'}$ ,  $Y_{n,n}^p$ , and  $Y_{n,n}^0$  were determined experimentally for five values of  $E_{\gamma m}$  from 10 to 22 MeV using a procedure analogous to that described in [18].

The results of the calculation of  $Y_{n,n}^0$ , taking into account photoneutrons from the reaction  $(\gamma, 2n)$  on  $^{115}\text{In}$  (see Fig. 1, curve 2) and neglecting these photoneutrons (see curve 3) do not differ very much.

As follows from the relation (8), the growth of the yield  $Y_{n,n'}^0$  with  $E_{\gamma m}$  taking into account the contribution to the yield by photoneutrons formed in reactions  $(\gamma, 2n)$  must be more rapid for  $E_{\gamma m} > E_{n,2n}^{\gamma}$ . Indeed, the curve of the yield  $Y_{n,n'}^0$ , calculated taking into account the contribution of neutrons from the  $(\gamma, 2n)$  reaction to the yield (see curve 2), is steeper for high  $E_{\gamma m}$  than the yield curve calculated without this reaction (see curve 3).

The experimental values for  $Y_{n,n'}^{oe}$ , within the limits of error of the measurements are in agreement with both computed curves, though they lie closer to the curve  $Y_{n,n'}^{oc}(\gamma, 2n)$ .

The computed and measured values of the yields  $Y_{\gamma,\gamma'}$ ,  $Y_{n,n'}^p$  and  $Y_{n,n'}^0$ , which agree within the limits of error of the measurements, were used to estimate the relative increase in the yields of the isomer  $^{115m}\text{In}$  due to the reaction  $(n, n')$  generated by the external ( $Y_{n,n'}^p/Y_{\gamma,\gamma'}$ ) and internal ( $Y_{n,n'}^0/Y_{\gamma,\gamma'}$ ) photoneutrons. For the experimental conditions described above, the relative increase for  $Y_{n,n'}^p/Y_{\gamma,\gamma'}$  was equal to 0.4, 0.7, 1.5, and 2.1% for  $E_{\gamma m}$  equal to 13, 16, 19, and 22 MeV, respectively, and 5, 10, 20, and 25% for  $Y_{n,n'}^0/Y_{\gamma,\gamma'}$  for the same values of  $E_{\gamma m}$ , respectively. It should be underscored that these estimates are meaningful only for the accelerator and the specific experimental conditions used in this work and are presented only as an illustration of the possibility of making a quantitative evaluation of the contribution of the reaction  $(n, n')$  to the yield of the isomeric state from the reaction  $(\gamma, \gamma')$ .

The experimental value of  $Y_{n,n'}^{oe}$  for  $E_{\gamma m} = 13$  MeV is higher than the computed values  $Y_{n,n'}^{oc}$ . It should be noted that for low  $E_{\gamma m}$  the experimental determination of different contributions to the yield of activation of isomeric states using the procedure in [18] is unreliable. The calculation of  $Y_{n,n'}$  neglecting the photoneutron spectra of indium  $Y_{\gamma,n}^c$  gives a dependence  $Y_{n,n'}(E_{\gamma m})$  differing appreciably from the values  $Y_{n,n'}^{oc}(E_{\gamma m})$ , calculated taking into account the photoneutron spectra and from the experimental values  $Y_{n,n'}^{oe}$ .

The computed dependences of  $Y_{n,n'}^p$  on  $E_{\gamma m}$  agree with the experimental dependences within the limits of error.

Thus the proposed method for calculating the contributions of neutron activation of isomeric states of nuclei for the model case of activation of indium samples studied here in a real bremsstrahlung beam from an electron accelerator gives reasonable agreement for both the relative contributions  $Y_{n,n'}^0/Y$  and  $Y_{n,n'}^p/Y$  and the energy dependence of these contributions.

Using the proposed scheme with the appropriate data on the cross sections of the reactions  $(\gamma, x)$  and  $(n, y)$ , it is possible to calculate the contributions of neutron activation of nuclei on external and internal photoneutrons to the activation of a finite sample in a bremsstrahlung beam from an electron accelerator. Such a calculation of the energy dependence of the activation effects from the reactions  $(n, \gamma)$  makes it possible to avoid performing a large number of measurements of these contributions for different values of the bremsstrahlung energy. The experimental measurement can be performed at one quite high value of the bremsstrahlung energy on the basis of the measurements of activation yields in two geometries for three identical samples using the procedure described in [18]. For the remaining values of the bremsstrahlung energy, the required contributions of the neutron activation are found by calculating the energy dependence using the absolute experimental data for one value of  $E_{\gamma m}$ .

The foregoing computational method can be used both in formulating experiments for determining the yields of photoactivation of nuclei by electron accelerators and for optimizing the conditions for determining elements in  $\gamma$  activation analysis.

#### LITERATURE CITED

1. R. A. Kuznetsov, Activation Analysis [in Russian], Atomizdat, Moscow (1974), p. 126.
2. A. L. Yakubovich, E. I. Zaitsev, and S. M. Przhivalgovskii, Nuclear-Physical Methods of Analysis of Minerals [in Russian], Énergoizdat, Moscow (1982), pp. 102-106.
3. A. K. Berzin, Yu. A. Gruzdev, and V. V. Sulin, in: Nuclear Physical Methods of Analysis of Matter [in Russian], Atomizdat, Moscow (1971), pp. 236-244.
4. O. Abbosov, S. Kodiri, and L. P. Starchik, in: *ibid.*, pp. 244-255.
5. Yu. N. Burmistenko, E. N. Gordeeva, and Yu. V. Feoktistov, in: Radiation Techniques [in Russian], No. 11, Atomizdat, Moscow (1975), pp. 225-235.

6. Yu. N. Burmistenko, B. N. Ryvkin, and Yu. V. Feoktistov, in: *ibid.* (1976), No. 13, pp. 219-227.
7. B. M. Yakovlev and V. I. Lomonosov, in: *Proceedings of the Scientific-Research Institute of Nuclear Physics at the Tomsk Polytechnical Institute* [in Russian], No. 6, Atomizdat, Moscow (1976), p. 37.
8. Ph. Breban et al., *Nucl Instrum. Methods*, **158**, 205-215 (1979).
9. L. Schiff, *Phys. Rev.*, **83**, 252 (1951).
10. L. Lanzl and A. Hanson, *Phys. Rev.*, **83**, 959 (1951).
11. M. G. Davydov and V. A. Shcherbachenko, "Calculation of the yield of photonuclear reactions," *At. Energ.*, **39**, No. 3, 210 (1975).
12. V. P. Kovalev, *Secondary Emission of Electron Accelerators* [in Russian], Atomizdat, Moscow (1979).
13. I. V. Gordeev, D. A. Kardashev, and A. V. Malyshev, *Nuclear-Physical Constants (Handbook)* [in Russian], Atomizdat, Moscow (1963).
14. A. K. Berzin, B. M. Yakovlev, and A. A. Yatis, in: *Electron Accelerators* [in Russian], Vysshaya Shkola, Moscow (1964), p. 435.
15. V. Emma et al., *Nuovo Cimento*, **21**, No. 1, 135 (1961).
16. B. M. Yakovlev and R. P. Meshcheryakov, in: *Electron Accelerators* [in Russian], Vysshaya Shkola, Moscow (1964), p. 430.
17. B. Berman, *At. Data Nucl. Data Tables*, **15**, 313-390 (1975).
18. L. Meyer-Shutzmeister and V. Telegdi, *Phys. Rev.*, **104**, No. 1, 185 (1956).

EXCITATION CROSS SECTION OF THE CHARACTERISTIC X RADIATION BY  
PROTONS AND  $^4\text{He}$  IONS FOR ELEMENTS WITH  $Z$  IN THE RANGE  $22 \leq Z \leq 83$

É. Brazevich, Ya. Brazevich, V. F. Volkov,  
S. A. Gerasimov, Lyu Zai Ik, G. M. Osetinskii,  
and A. Purév

UDC 539.17.012

The paper is devoted to the determination of the excitation cross section of the characteristic x radiation (CXR)  $\sigma_s$  during the bombardment of a number of elements with a beam of protons and  $^4\text{He}$  ions with energy 1.5-3.8 MeV. The cross sections were determined for elements for which, in this range of energies, data about  $\sigma_s$  either are lacking or require refining.

Thin targets were used for the measurements. In this case,  $\sigma_s$  is found by the formula

$$\sigma_s = \frac{Y}{N_p N_M}, \quad (1)$$

where  $N_p$  is the number of protons or  $^4\text{He}$  ions incident on the target;  $N_M$  is the number of atoms of the sample being investigated per  $\text{cm}^2$ ;  $Y = \frac{Y_\alpha}{\varepsilon_\alpha} + \frac{Y_\beta}{\varepsilon_\beta}$  is the yield of characteristic

x radiation for the  $\alpha$ - and  $\beta$ -lines of the K-series of the element being studied;  $Y = \frac{Y_\alpha}{\varepsilon_\alpha} + \frac{Y_{\beta_1}}{\varepsilon_{\beta_1}} +$

$\frac{Y_{\beta_3}}{\varepsilon_{\beta_3}} + \frac{Y_{\gamma_1}}{\varepsilon_{\gamma_1}} + \frac{Y_{\gamma_3}}{\varepsilon_{\gamma_3}}$  is the same yield for the  $\alpha$ -series;  $\varepsilon_\alpha$ ,  $\varepsilon_\beta$ , etc. is the recording efficiency

of the CXR for the  $\alpha$ -,  $\beta$ -,  $\beta_1$ -, etc. lines of the K- or L-series, and  $\varepsilon_{i,S}$  is the recording efficiency of the  $i$ -th line of the S-series. The recording efficiency of the CXR is determined as  $\varepsilon_{i,S} = \text{cabc} \varepsilon_\lambda (\Delta\Omega/4\pi)$ , where  $\text{cabc}$  is a coefficient taking into account the absorption of radiation on the path from the target to the detector (absorption in peepholes of the detector chamber, in the air, and in the filters);  $\varepsilon_\lambda$  is the recording efficiency by the detector of the radiation with a wavelength  $\lambda$ ;  $\Delta\Omega$  is the solid detection angle. With con-

Translated from *Atomnaya Energiya*, Vol. 59, No. 1, 52-57, July, 1985. Original article submitted July 4, 1984.

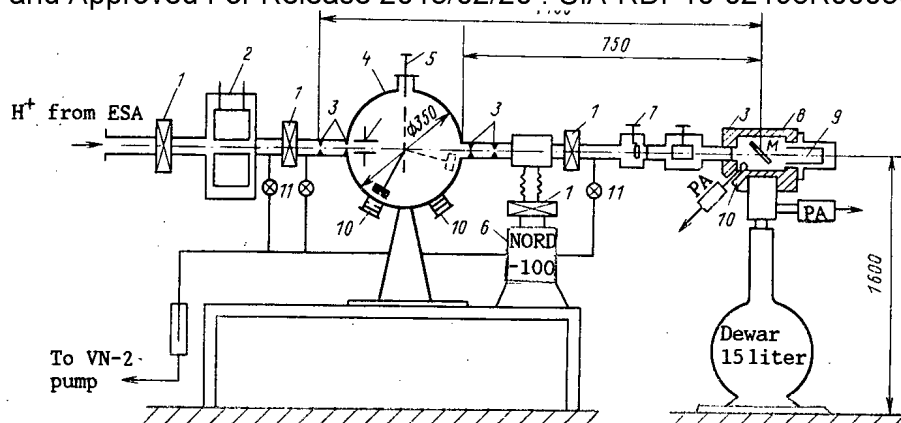


Fig. 1. Layout of experiment: 1) vacuum seals; 2) nitrogen trap; 3) collimators; 4) intermediate chamber; 5) plates for modulation of the beam; 6) high-vacuum pump; 7) device for tracking the beam; 8) CXR chamber; 9) Faraday cylinder; 10) Si-detector; 11) valve; D) CXR detector; PA) preamplifier; M) target; ESA) electrostatic accelerator.

stant geometry of the experiment, the product  $\text{cabc}(\Delta\Omega/4\pi)\epsilon_\lambda$  is the magnitude of the constant determined by calibration changes.

The characteristic features of the experiment being described are:

1. The CXR yield of the  $i$ -line ( $\alpha$ ,  $\beta$ , etc.) of the S-series (K or L), denoted by us in future as  $Y_{i,S}$ , was determined from the area of the CXR energy spectrum obtained on a multichannel pulse analyzer using the ACTIV program of JINR on the BESM-6 computer.
2. The number of particles incident on the target ( $N_p$ ) was found from the beam charge, measured by the integral of the current. The error in the determination of the charge in the working range of the beam current of  $10^{-8}$ - $10^{-9}$  A is not greater than 1-1.5%.
3. The number of atoms of the target ( $N_M$ ) was determined by measuring the elastic scattering of the  $^4\text{He}$  ions at an angle of  $135^\circ$  in the laboratory system of coordinates, in the same geometry and for the same energy of the accelerated ions for which the CXR yield was determined. Scattering was assumed to be Rutherford scattering. This assumption is completely valid in the range of energies investigated.
4. The detection efficiency  $\epsilon_{i,S}$  was determined by measuring the yield  $Y_{i,S}^{\text{st}}$  of CXR from standard targets, for which the number of atoms is known. The calculation was performed by the formula

$$\epsilon_{i,S} = \frac{Y_{i,S}^{\text{st}}}{N_p^{\text{st}} N_M^{\text{st}} \sigma_{i,S}^{\text{st}}}, \quad (2)$$

where the number of atoms in the target-standards (per  $\text{cm}^2$ ) was found by measuring the inelastic scattering of  $^4\text{He}$  ions with energy 2-3 MeV in the same target geometry in which the cross section was measured. The value of  $\sigma_S^{\text{st}}$  was calculated from special tables compiled by us [2] as a result of averaging all the known data on  $\sigma = f(E)|_Z$ . The necessity for these averaged tables originates because the discrepancies in the published data for one and the same elements and energy, but obtained by different authors, sometimes exceed the experimental errors by a factor of two to three or more, and because of this it is difficult to give preference to some or other method for their determination. The data were averaged by the method of least squares on the SDS-6500 computer by the FUMILI program of JINR, using the polynomial form

$$\sigma(E) = \sum_{n=1}^m A_n E^{n-1},$$

where A is the coefficient of the polynomial of  $(n-1)$ -power. The construction of these tables is described in more detail in [2].

TABLE 1. CXR Excitation Cross Sections for the K- and L-Series, during the Bombardment of Elements with Protons in the Energy Range 1.46-3.8 MeV

Element	Z	Proton energy, MeV																	
		1,46		2,055		2,5		2,985		3,205		3,527		3,6		3,7		3,8	
		expt.	[2]	expt.	[2]	expt.	[2]	expt.	[2]	expt.	[2]	expt.	[2]	expt.	[2]	expt.	[2]	expt.	[2]
CXR K-series																			
Ti	22	89,95	117,9	213,9	219,9	285,6	298,8	364,5	387,3			440,5							
Se	34	4,85	5,53		13,7	14,61		23,6		26,85		30,44				35,89			
Rb	37	2,67	2,63	7,41	5,73	12,31	10,4	18,9	15,6			24,50							
Zr	40	1,15	1,77	3,20	3,45	5,39	4,61	8,67	5,77			11,36							
Nb	41	0,94	0,85	2,59	2,52	4,50	4,20	7,18				10,43				11,18			
Mo	42	0,71	0,80	1,97	2,31	3,40	3,98	5,55	5,52			4,96							
Pd	46	0,30	0,29	0,86		1,69		2,43				4,11		4,46					
Ag	47	0,20	0,27	0,52	0,81	0,82	1,41	1,53	2,18	1,93	2,51	2,40	2,94		3,02	2,28	3,13		3,24
CXR L-series																			
Sb	51	307,0		506,12		676,8		802,8		892,4									
Te	52	272,7		387,0		637,6		804,0		847,3		925,7							
Ta	73	25,92	23,9	52,43	52,2	83,4	76,9	99,4	105,3		118,6	144,6	138,8		143,6		150,6	168,3	157,9
W	74	26,2		53,9		81,3		105,7				122,2						161,7	
Bi	83	7,53	7,15	15,68	16,9	29,46	26,3	39,7	37,9		43,6	49,00	52,2		54,2		57,0		59,8

The mean square error in the determination of  $\epsilon_{i,S}$  does not exceed 7%. It comprises the error in the determination of  $Y_{i,S}$  (not more than 2%), the number of target atoms ( $\sim 4\%$ ), in the measurement of  $N_p$  (1.5%), and the error in  $\sigma_S^{st}$  from the table of averaged values for  $\sigma_S = f(Z)|E \approx 5\%$ . We note that the method chosen by us for obtaining the recording efficiency of the CXR, based on the averaging of known tabular values of  $\sigma_S$ , although it leads to slightly overestimated errors in  $\epsilon$ , to a considerable degree eliminates the appearance of unaccounted errors, which may arise in the determination of this quantity by other methods.

The scheme of the experiment is shown in Fig. 1. It can be seen from the figure that the beam of protons or "He ions from the JINR electrostatic accelerator of the Van de Graaf type, on traversing the section of the ion-conductor, falls on the multiposition target located at the center of the measurement chamber. The beam, on this section, is shaped by four diaphragms. A uniform distribution of the current at the target is provided by debunching the beam in two mutually perpendicular directions by means of electrostatic lenses. The target is insulated from the housing and is connected with the current integrator. At an angle of  $90^\circ$  relative to the incident beam and at a distance of 50 mm from the center of the target the chamber has an opening covered with milar foil with a thickness of 25  $\mu\text{m}$ . Beyond the milar window is installed a Si(Li)-detector, the pulses from which via a preamplifier and an amplifier are recorded by a DIDAC multichannel pulse analyzer. The amplifier provides the stability of the zero level at the output and an indication of self-pileup of pulses. The structural scheme for recording the CXR has a "real time" counter, which sums the "dead" time of detection in the preamplifier, amplifier, and multichannel pulse analyzer, and automatically projects the real time count on the luminous light panel of this instrument. The energy resolution of the spectrometer, measured on the 6.4-keV line of  $^{57}\text{Co}$ , amounts to 220 eV. At an angle of  $135^\circ$  in the chamber, a silicon surface-barrier detector is installed, used for the simultaneous measurement of the elastic scattering of "He ions and the yield of CXR.

#### Experimental Results

Table 1 shows the excitation cross sections for the CXR of the K- and L-series during the bombardment of the elements being investigated by a beam of protons with energy 1.46-3.8 MeV. The excitation cross sections for the K-series were measured for a number of elements in the range  $22 \leq Z \leq 47$ , and for the L-series in the range  $51 \leq Z \leq 83$ . For the purpose of verifying the validity of the measurement procedure, in the table are included our data for Ag, Ti, and Bi, the CXR excitation cross sections for which in the range of energies investigated were determined previously by other authors and coincide well with one another. For comparison, the averaged values of the curves  $\sigma_S = f(E)|Z$  from [2] are given in the same table. It can be seen from the table that in the energy range where a comparison is possible, the CXR excitation cross sections coincide, within the limits of error, with the averaged literature data.

Element	Z	Energy of <sup>4</sup> He ions, MeV																	
		1,5		2,009		2,477		2,987		3,2		3,491		3,6		3,7		3,8	
		expt.	[3]	expt.	[3]	expt.	[3]	expt.	[3]	expt.	[3]	expt.	[3]	expt.	[3]	expt.	[3]	expt.	[3]
CXR K-series																			
Ti	22	4,71	8,12	18,9	21,5	32,6	41,6	55,9	73,2		89,6	90,5	115,0		126,0		136,3		147,1
Cr	24	4,17	4,45	10,7	11,4	23,1	26,3	41,1	63,6		83,4	69,05	109,0		119,0		127,4		137,5
Co	27	1,16	1,39	3,28	3,81	6,75	7,63	12,31	13,2	15,5	16,1	19,91	20,8		22,9		24,9		27,1
Cu	29	0,962	0,810	3,15	2,25	6,55	4,48	12,29	8,12		10,1	20,3	13,1		14,4		15,7		17,0
Se	34	0,133	0,127	0,397	0,438	0,827	0,914	1,58	1,67	2,00	2,15	2,68	3,00	2,86	3,36	3,05	3,68		3,98
Rb	37	0,555		0,185		0,41		0,816				1,48							
Zr	40	0,0224		0,082		0,19		0,367				0,643							
Nb	41		0,0282	0,062	0,092	0,146	0,196	0,301				0,503						0,626	
Mo	42		0,0191	0,049	0,066	0,113	0,15	0,232	0,303	0,135	0,388	0,4	0,531		0,593		0,656	0,552	0,725
Pd	46	0,0040		0,0196		0,05		0,104		0,113		0,191		0,211					
Ag	47	0,0027	0,0035	0,019	0,019	0,039	0,038	0,082	0,063		0,081	0,143	0,120	0,165	0,132	0,186	0,147		0,157
Sn	50		0,0002		0,0087	0,019	0,019	0,039	0,025		0,035	0,072	0,049		0,054		0,058		0,063
CXR L-series																			
Pd	46	88,8		189,2		262,4		497,7		585,9									
Ag	47	60,4		128,6						467,0				629			637,8		
Sn	50	39,12				196,3		313,8				452,7							
Sb	51	43,7		90,7		158,7		238,8		271,8		325,0							
Te	52	38,3		79,6		135,8		214,0		261,0		316,2							
Ta	73		1,75	5,27	5,38	9,73	10,0	15,7	16,5		19,7	21,3	24,4		26,3		28,1	27,53	30,0
W	74			3,93		6,71		11,3				16,5						21,39	
Pt	78	0,893		2,60		4,82		8,46		10,4		12,4							
Bi	83	0,429	0,504	1,22	1,93	2,43	2,69	3,11	3,88		4,82	6,80	6,56		7,30	14,8	7,97		8,60

The CXR excitation cross sections for the K- and L-series as a result of the bombardment of a number of elements with a beam of  $^4\text{He}$  ions in the energy range 1.5-3.8 MeV are given in Table 2, and also the data of [3] averaged in the energy range of interest to us by the method stated earlier.

The values of  $\sigma$  from the bombardment of Co, Se, Ag, and Ta are considered by us to be confirmation of the validity of the assumed method of measurement. The measurements were repeated for a number of elements, as the data on the CXR cross sections published by different authors disagree strongly. Thus, for example, in the tables of [3] for the excitation of the CXR K-series by the bombardment of Cu with  $^4\text{He}$  ions with energy 2.6 MeV, two values are given for the cross sections: 8.68 and 4.7 b, for the excitation of the K-series in the case of the bombardment of Cr ( $E_{\text{He}} = 2.1$  MeV) 1.35 and 21.0 b, and for excitation of the L-series of Bi ( $E_{\text{He}} = 3.0$  MeV) 5.1 and 16.1 b, etc.

The mean square error in the determination of the cross sections in all the measurements does not exceed 10%. It comprises the errors in the determination of the CXR yield ( $\pm 2\%$ ),  $\epsilon$  (5-7%), the number of target atoms (4%), the number of particles incident on the target (1.5%), and also the error in the determination of  $\sigma$  (1%) due to the errors in the energy measurement [determined from the curve of  $\sigma = f(E)$ ].

#### Discussion of the Results Obtained

The CXR excitation cross sections as a result of the bombardment of the elements investigated, with a beam of protons and  $^4\text{He}$  ions, were compared with the results of theoretical calculations performed in Born approximation of plane waves (BAPW) and on a model of binary collisions (MBC). The calculations give the ionization cross section, and conversion to the excitation cross sections was effected by multiplying these values by the fluorescence yield and the probability of a Coster-Kronig transition [4]. It should be noted that the experimental data on the ionization cross sections of the K- and L-shells in the MBC-approximation, known at the present time, have been given by a number of authors using the wave function only of the 1s-state for all subshells [5, 6].



For the calculations of the cross sections in BAPW, the tabular data of [7, 8] usually have been used, containing the function  $f(\eta\theta)$ , related with the ionization cross section  $\sigma$  by the equation

$$\sigma = 8\pi Z_1^2 a_0^2 Z_2^{-4} \eta_s^{-1} f(\eta_s \theta_s); \quad \eta_s = \frac{m_e E_1}{M_1 Z_2^2 R_\infty};$$

$$\theta_s = \frac{n^2 E_{eb}}{Z_2^2 R_\infty},$$

where  $Z_1$ ,  $M_1$ , and  $E$  are the atomic number, mass, and energy of the incident particle;  $m_e$  and  $E_{eb}$  are the mass and energy of the electron bond in the shell;  $a_0$  and  $R_\infty$  are the Born radius and Rydberg constant;  $n$  is the principal quantum number of the shell;  $Z_2$  is the atomic number of the target atom, and  $\theta_s$  is the screening constant,  $\theta < 1$ .

It was assumed in the calculations that screening of the charge of the nucleus by electrons of the atom can be taken into account by the introduction of the screened charge in accordance with Sletten's rule:  $Z_{2s} = Z_2 - 0.3$  for the K-shell, and  $Z_{2s} = Z_2 - 4.15$  for the L-shell.

We note that this method of calculation has definite drawbacks as, in the first place, the choice of  $\theta < 1$  corresponds to negative values of the kinetic energy of the electron knocked out, for the consideration of which there are no convincing reasons, and, secondly, the determination of the effective charge  $Z_{2s}$  according to Sletten's rule leads to very large errors. In contrast from the stated method of calculation, in our case for the calculations by MBC and BAPW the 1s-, 2s-, and 2p-wave functions of a hydrogenlike atom were used, and screening of the charge of the nucleus of the target atom was taken into account by the introduction of the effective charge  $Z_{2s}$ , obtained from the relation

$$E_{eb} = \frac{Z_{2s}^2}{n^2} R_\infty,$$

where  $n$  is the principal quantum number;  $E_{eb}$  is the experimental value of the binding energy of the electron in the shell.

As the consideration was conducted for a hydrogenlike atom, the results of the theoretical calculations for each individual subshell both in MBC as well as in BAPW were presented in the form of a scaling law

$$\frac{\sigma (n^2 E_{eb})^2}{Z_1} = F_{n,e} \left( \frac{E_1}{\lambda n^2 E_{eb}} \right).$$

The energy dependencies of the ratios of the calculated and experimental CXR excitation cross sections ( $\sigma_T/\sigma_E$ ) for the K-shell of some of the atoms investigated by their excitation with a beam of protons with energy 1.5-3.8 MeV are shown in Fig. 2. The values of  $\sigma_T$ , used in the calculation of  $\sigma_T/\sigma_E$ , were calculated in MBC approximation since, as analysis of the results of the present paper and the numerous publications showed, the accuracy of the experimental determination of  $\sigma_E$  is inadequate for establishing which of the approximations - MBC, BAPW, or their various modifications, including those proposed in the present paper - more correctly describes the ionization process of the atoms by protons. It can be seen from Fig. 2 that the calculations of  $\sigma_T$  within the limits of error coincide with the experimental data ( $\sigma_T/\sigma_E \approx 1$ ). Similar calculations of  $\sigma_T/\sigma_E$  for the ionization of the L-shell of the atoms investigated by protons, independently of the method of calculation (by MBC or BAPW), also give values close to 1 (these results are not shown in the figure).

A more contradictory pattern is observed with the calculation of  $\sigma_T$  for the ionization of the K-shell as a result of excitation by  $^4\text{He}$  ions. In this case, if for the CXR excitation of the L-series by protons and  $^4\text{He}$  ions the calculated values of  $\sigma_T$  coincide with the experimental values, then in the case of ionization of the K-shell by  $^4\text{He}$  ions the ratio  $\sigma_T/\sigma_E$  is significantly different from unity (Fig. 3). These mechanisms can be traced in Figs. 4 and 5 where, in order to exclude the effect of the individual features of the target atoms during their interaction with the incident particles, averaging of  $\sigma_T/\sigma_E = f(E)$  with respect to the atomic numbers  $Z_2$  is carried out. The curves of  $(\sigma_T/\sigma_E)_a = f(E)$  are shown in Fig.

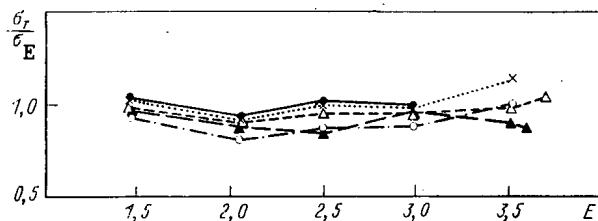


Fig. 2

Fig. 2. Dependence of  $\sigma_T/\sigma_E$  on the proton energy for the K-series (MeV):  $\times$ —) calculation performed in MBC approximation;  $\bullet$ ) Mo;  $\times$ ) Zr;  $\circ$ ) Rb;  $\Delta$ ) Nb;  $\blacktriangle$ ) Pd.

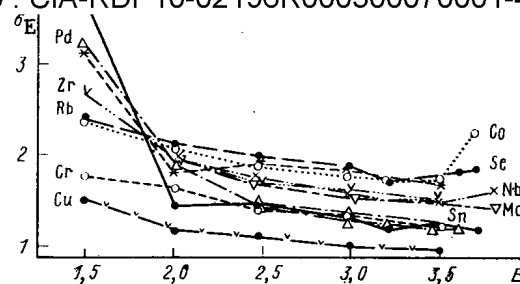


Fig. 3

Fig. 3. Dependence of  $\sigma_T/\sigma_E$  on the energy of the  $^4\text{He}$  ion for the CXR of the K-series (calculation performed in MBC approximation).

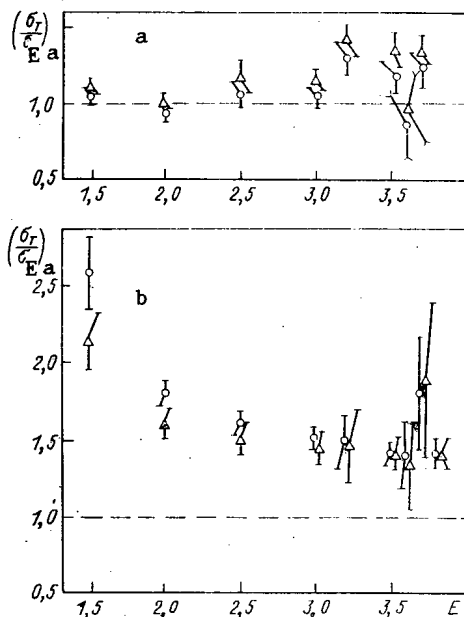


Fig. 4

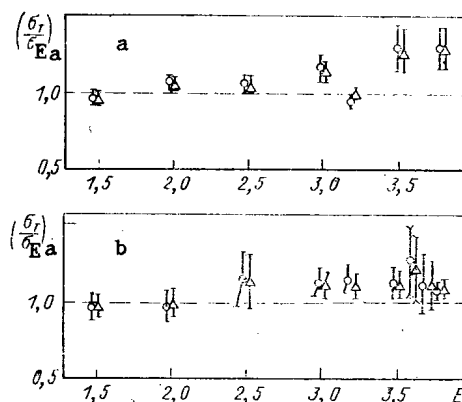


Fig. 5

Fig. 4. Dependence of  $(\sigma_T/\sigma_E)_a$  on the energy of the incident ion for ionization of the K-shell: a) ionization by proton; b) ionization by  $^4\text{He}$ ;  $\circ$ ) calculation in MBC-approximation;  $\Delta$ ) calculation in BAPW.

Fig. 5. Dependence of  $(\sigma_T/\sigma_E)_a$  on the energy of the incident ion for ionization of the L-shell: a) ionization by proton; b) ionization by  $^4\text{He}$ ;  $\circ$ ) calculation in MBC approximation;  $\Delta$ ) calculation in BAPW.

4 in the case of ionization of the K-shell of the atoms investigated by protons and  $^4\text{He}$  ions. The upper part of Fig. 4 (a) is related to ionization by protons, and the lower part (b) to ionization by  $^4\text{He}$  ions. In Fig. 5 (a, b) these same curves are for ionization of the L-shell. It can be seen from Figs. 4a and 5a, b that in the case of ionization of the K- and L-shells by protons, and ionization of the L-shell by  $^4\text{He}$  ions, the averaged values of  $(\sigma_T/\sigma_E)_a$  are considerably greater than unity and increase with reduction of the energy. The reason for this discrepancy of the theoretical and experimental cross section values in the case of ionization of the K-shell by  $^4\text{He}$  ions is not altogether clear, and its explanation will require further investigations. It can be understood qualitatively if the deviation of the trajectory of the incident particles from rectilinear (assumed in the BAPW theory) in the Coulomb field of the nucleus is taken into consideration. As a result of this deviation, the distance of maximum convergence (d) of the incident ion with the target atom is increased, and which for the  $^4\text{He}$  ion will be greater than for the proton. And as the radius of the L-shell is four times greater than the radius of the K-shell, the ionization cross section with

increase of the distance of closest approach is reduced for the K-shell more considerably than for the L-shell (in the discussion, it is supposed that ionization of the atom takes place mainly by ions approaching the nucleus of the target at a distance  $d < a_2$ , where  $a_2 = n^2 a_0 / Z_2$ , and  $a_0$  is the Bohr radius). By comparison with the distance according to the BAPW, the ionization cross section in this case is reduced with decrease of the energy of the incident ion and with increase of  $Z_2$ , which can be tracked by considering the relation connecting the parameter of maximum approach  $d$  of the ion with the target atom and the impact parameter ( $b$ ):

$$d(b) = d_{\min} \left[ 1 + \sqrt{1 + \left( \frac{b}{d_{\min}} \right)^2} \right],$$

where  $d_{\min} = Z_1 Z_2 e^2 / 2E_1$  is one-half of the distance of the maximum approach for a central collision; and  $E$  is the energy of the ion. The discussion conducted is confirmed by the results shown in Figs. 3 and 4b, from which it can be seen that  $\sigma_T / \sigma_E$  increases with increase of  $Z_2$  and with reduction of the energy of the incident ion.

In conclusion, the authors thank M. Paiek of the Joint Institute of Nuclear Research (JINR) for useful discussions.

#### LITERATURE CITED

1. É. Brazevich et al., Preprint JINR 18-81-503, Dubna (1981).
2. É. Brazevich et al., Preprint JINR B1-81-320, Dubna (1981).
3. At. Data Nucl. Data Tables, 17, No. 2 (1976); At. Data Nucl. Data Tables, 21, No. 6 (1978).
4. M. Krause, J. Phys. Chem. Ref. Data, 8, 307 (1979).
5. J. Garcia, R. Fortner, and T. Kavanagh, Rev. Mod. Phys., 45, 111 (1973).
6. F. McDaniel, T. Gray, and R. Gardner, Phys. Rev., 11, 1607 (1975).
7. R. Rece, G. Basbas, and F. McDaniel, At. Data Nucl. Data Tables, 20, 503 (1977).
8. B. Choi, E. Merzbacher, and G. Khandelwal, At. Data, 5, 291 (1973).

# INFLUENCE OF REACTOR IRRADIATION UPON THE ELECTROPHYSICAL CHARACTERISTICS OF HETEROEPITAXIAL p-SILICON-ON-SAPPHIRE LAYERS

B. V. Koba, V. L. Litvinov,  
A. L. Ocheretyanskii, V. M. Stuchebnikov,  
I. B. Fedotov, N. A. Ukhin,  
V. V. Khasikov, and V. N. Chernitsyn

UDC 537.311.33,315.59:621.315.59

Strongly alloyed silicon-on-sapphire structures with p-type conductivity are promising for highly sensitive strain transducers of mechanical quantities in automatic control systems; these transducers have excellent metrological characteristics and can work reliably under the strenuous operational conditions of atomic power stations [1-5].

We report in this paper on the results of an investigation of the influence of n- $\gamma$  reactor radiation upon the electrophysical properties and the coefficients  $m_{44}$  of elastoresistivity of highly alloyed p-silicon-on-sapphire structures with concentrations of  $5.3 \cdot 10^{18}$ - $1.8 \cdot 10^{20}$  cm $^{-3}$  of the alloying admixture; these elements were used as strain transducers of mechanical quantities.

In order to measure the temperature dependencies of the specific resistivity  $\rho$ , the concentration  $p$  of the holes, and their mobility  $\mu$ , we used silicon-on-sapphire structures on which Hall samples were produced by photolithography. In order to measure the coefficient  $m_{44}$  of elastoresistivity, which determines the sensitivity of the strain transducer, we used beam-shaped test samples which were cantileverwise attached by welding with rigid PSR-72 solder and which had silicon resistors arranged parallel or perpendicular to the axis of the beam.  $m_{44}$  was measured with the technique which is the analog to that described in [6]. We assumed in the calculation of the parameter  $m_{44}$  that the elastic characteristics of silicon and sapphire do not change during the irradiation [7].

Our samples were irradiated in a VVR-2000 reactor under normal conditions ( $T_{\text{irrad}} \leq 70^\circ\text{C}$ , normal atmospheric pressure). The neutron-flux dosimetry was made with sulfuric threshold indicators ( $E_{\text{thresh}} = 2.9$  MeV); the darkening of SGD-9 glass was used for the dosimetry of the gamma radiation. Stepwise irradiation was used until a certain flux  $\phi$  between  $10^{14}$  and  $4.5 \cdot 10^{16}$  cm $^{-2}$  had been reached ( $E_n \geq 2.9$  MeV). The neutron flux intensity was  $10^9$ - $10^{10}$  cm $^{-2}$ ·sec $^{-1}$ ; the intensity of the accompanying  $\gamma$  radiation amounted to several hundred R/sec (1 R =  $2.58 \cdot 10^{-4}$  C/kg). In order to reduce the activation, the samples were inserted into 0.5-mm-thick cadmium jackets during the irradiation. Before and after each of the irradiation steps, the parameters under inspection were measured.

Figure 1 depicts the dose dependence of the specific resistivity, the concentration of the holes, and their mobility in silicon-on-sapphire structures with an initial charge carrier concentration  $p_0 = 6 \cdot 10^{19}$  cm $^{-3}$ . It follows from Fig. 1 that, by contrast to weakly alloyed bulk silicon [8], the relative change in the mobility in strongly alloyed p-silicon-on-sapphire structures becomes comparable with the relative change of the concentration due to the irradiation. The maximum is at the temperature of liquid nitrogen. The resulting dose dependencies of the parameters under inspection are logarithmic and therefore differ from the dependencies of the same parameters in weakly alloyed bulk silicon.

Figure 2 depicts the temperature dependence of the mobility of holes in silicon-on-sapphire structures with various degrees of doping and refers to various irradiation doses. The form of the temperature dependence of the mobility is not affected by the irradiation in all samples examined. A similar behavior is observed in the temperature dependencies of the charge carrier concentration.

Table 1 lists the initial rate of change of the specific resistivity, the concentration, and the mobility of the charge carriers in dependence upon the irradiation dose. It follows

---

Translated from Atomnaya Energiya, Vol. 59, No. 1, pp. 58-59, July, 1985. Original article submitted April 16, 1984.

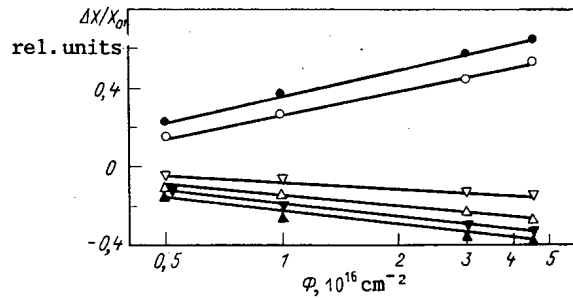


Fig. 1. Radiation-induced change of the specific resistivity (o, ●), of the concentration ( $\Delta$ ,  $\blacktriangle$ ), and of the mobility of holes ( $\nabla$ ,  $\blacktriangledown$ ) in silicon-on-sapphire structures at 77 (●,  $\blacktriangle$ ,  $\blacktriangledown$ ) and 300°K (o,  $\Delta$ ,  $\nabla$ ).

TABLE 1. Initial Rate of Change of the Parameters\*

Initial concn. (cm <sup>-3</sup> ) of the holes	$\frac{\Delta \rho}{\rho_0 \Delta \phi} \cdot 10^{16}, \text{ cm}^2$	$\frac{\Delta N_A}{N_{A0} \Delta \phi} \cdot 10^{16}, \text{ cm}^2$	$\frac{\Delta \mu}{\mu_0 \Delta \phi} \cdot 10^{16}, \text{ cm}^2$	$\frac{\Delta \mu_h}{\mu_{h0} \Delta \phi} \cdot 10^{16}, \text{ cm}^2$	$\frac{\Delta \mu_v}{\mu_{v0} \Delta \phi} \cdot 10^{16}, \text{ cm}^2$	$\frac{\Delta \mu}{\Delta \phi} \cdot 10^{16}, \text{ cm}^2/\text{V} \cdot \text{sec}$	$\frac{\Delta \mu}{\Delta \phi} \cdot 10^{16}, \text{ cm}^2/\text{V} \cdot \text{sec}$
BKDB-10							
$2 \cdot 10^{16}$	40	3,2	25	400	990	5	
KDB-7.5							
$3,1 \cdot 10^{15}$	45	2,4	9,7	338	600	3	
silicon-on-sapphire							
$5,3 \cdot 10^{18}$	0,0170	0,080	0,019	$29,8 \cdot 10^{-1}$	5,33	10	
$2,9 \cdot 10^{19}$	0,066	0,045	0,017	$3,0 \cdot 10^{-4}$	2,12	48	
$6,1 \cdot 10^{19}$	0,032	0,020	0,015	$0,80 \cdot 10^{-4}$	0,86	92	
$1,8 \cdot 10^{20}$	0,030	0,017	0,011	$0,26 \cdot 10^{-4}$	0,68	198	

\* $E_n \geq 0.1 \text{ MeV}$ .

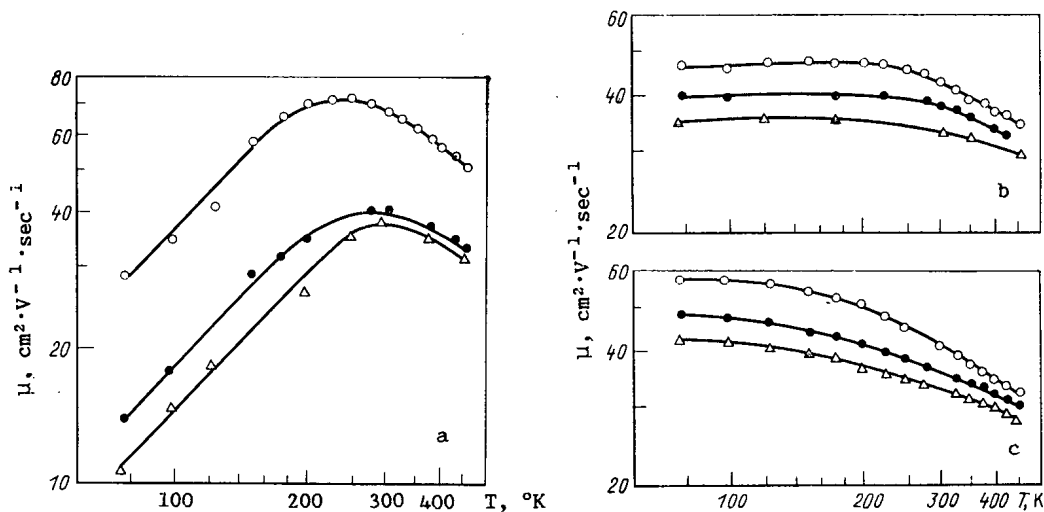


Fig. 2. Temperature dependence of the Hall mobility of the holes in silicon-on-sapphire structures after various irradiation doses: a)  $p_0 = 5.3 \cdot 10^{18} \text{ cm}^{-3}$ ;  $\phi = 0$  (o),  $1.6 \cdot 10^{16}$  (●), and  $3 \cdot 10^{16}$  ( $\Delta$ )  $\text{cm}^{-2}$ ; b)  $p_0 = 6.1 \cdot 10^{19} \text{ cm}^{-3}$ ;  $\phi = 0$  (o),  $5 \cdot 10^{15}$  (●), and  $4.5 \cdot 10^{16}$  ( $\Delta$ )  $\text{cm}^{-2}$ ; c)  $p_0 = 1.8 \cdot 10^{20} \text{ cm}^{-3}$ ,  $\phi = 0$  (o),  $1 \cdot 10^{16}$  (●), and  $3 \cdot 10^{16}$  ( $\Delta$ )  $\text{cm}^{-2}$ .

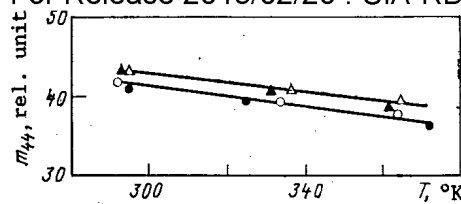


Fig. 3. Temperature dependence of  $m_{44}$  in silicon-on-sapphire structures ( $p_0 = 6 \cdot 10^{19} \text{ cm}^{-3}$ ) after various irradiation doses:  $\Phi = 0$  (o,  $\Delta$ ),  $5 \cdot 10^{15}$  ( $\Delta$ ), and  $4.5 \cdot 10^{16}$  ( $\bullet$ )  $\text{cm}^{-2}$ .

from the data that when the degree of doping increases, the relative rates of change in all the parameters examined decrease.

The absolute rate of the change of the hole concentration in silicon-on-sapphire structures is much greater than in weakly alloyed bulk silicon and depends more strongly upon the degree of doping. On the other hand, the absolute rate of the change of the mobility is much smaller and depends only weakly upon the degree of doping of the same materials.

Figure 3 illustrates the experimental temperature dependence of  $m_{44}$  in a test sample of silicon on sapphire with a hole concentration of  $6 \cdot 10^{19} \text{ cm}^{-3}$  before and after irradiation. Obviously, within the experimental error limits,  $m_{44}$  does not depend upon the flux up to  $\Phi = 4.5 \cdot 10^{16} \text{ cm}^{-2}$ .

Since the specific resistivity of the silicon film in silicon-on-sapphire structures is significantly affected by the irradiation, the output signal of the strain transducer in a strain-sensitive bridge circuit supplied with the current  $i_0$  from a generator is

$$U^i \simeq i_0 m_{44} R \varepsilon$$

( $R$  denotes the resistance of the strain transducer and  $\varepsilon$ , the deformation of the elastic element [1]) and must also depend upon the time during the irradiation. Therefore, in such strain transducers one cannot employ silicon-on-sapphire structures providing self-compensation of the temperature-dependent error of the sensitivity of the instrument [1]. Since  $m_{44}$  does not change upon irradiation, the output signal of the strain transducer in a strain-sensitive bridge circuit supplied by a generator with the voltage  $U_0$  is

$$U^U = U_0 m_{44} \varepsilon$$

and will not change, too. Based on the physical concepts of the coefficient of elastic resistivity [9], there is no reason to expect its change upon irradiation in structures with a high degree of doping. Accordingly, in order to reduce the temperature-dependent error of the transducer, one conveniently uses silicon-on-sapphire structures with a degree of doping  $p \geq 2 \cdot 10^{20} \text{ cm}^{-3}$  for which  $m_{44}$  depends only slightly upon the temperature [1]. The simultaneous decrease in the relative change of the specific resistivity by irradiation improves the stability of the initial output signal of the strain transducer.

It follows from the results of these investigations that highly alloyed silicon-on-sapphire structures with a degree of doping  $\geq 6 \cdot 10^{19} \text{ cm}^{-3}$  can be used to build strain-sensitive elements capable of working under the conditions of reactor irradiation without changing their sensitivity by more than 2-4%, at least at  $\Phi < 4.5 \cdot 10^{16} \text{ cm}^{-2}$ .

#### LITERATURE CITED

1. V. M. Stuchebnikov, "Strain-Resistor Transducers on the Basis of Heteroepitaxial 'Silicon-on-Sapphire' Structures," *Izmereniya, Kontrol', Avtomatizatsiya*, No. 4(44), 15 (1982).
2. N. A. Trofimov and V. V. Lappo, *Measurement of the Parameters of Thermophysical Processes in Nuclear Power Engineering* [in Russian], Atomizdat, Moscow (1979).
3. V. I. Vaganov, *Integral Strain Transducers* [in Russian], Énergoatomizdat, Moscow (1983).
4. V. M. Stuchebnikov, "Integral Semiconductor Strain-Resistor Transducers of Mechanical Quantities," *Izmereniya, Kontrol', Avtomatizatsiya*, No. 1(45), 30 (1983).

5. A. V. Beloglazov, V. M. Stuchebnikov, V. V. Khasikov, et al., "Semiconductor strain converters of pressure and force on the basis of heteroepitaxial 'silicon-on-sapphire' structures," Prib. Sistemy Upr., No. 5, 21, 22, 27 (1982).
6. J. Hyncek, "Elastoresistance in n-type silicon-on-sapphire," J. Appl. Phys., 45, No. 6, 2631 (1974).
7. P. Mayer and M. Leconte, "Energie interne et constantes elastiques due silicon irradie aux neutrons rapides," J. Phys. Rad., 21, 242 (1960).
8. V. S. Vavilov and N. A. Ukhin, Radiation Effects in Semiconductors and Semiconductor Instruments [in Russian], Atomizdat, Moscow (1960).
9. G. L. Bir and G. E. Pikus, Symmetry and Deformation-Induced Defects in Semiconductors [in Russian], Nauka, Moscow (1972).

## CALCULATION AND EXPERIMENTAL INVESTIGATION OF THE HEAT REMOVAL

## MODES OF A SHUTDOWN BN-600 REACTOR OF THE BELOYARSK

## NUCLEAR POWER STATION

A. I. Karpenko, A. A. Lyzhin,  
and A. G. Sheinkman

UDC 621.039.58

Heat removal from the core of the BN-600 reactor is secured by three independent loops, each consisting of a first and second circuit with sodium coolant and a third circuit with water-steam as a working medium. It is essential to know the speed of the heating up of the power plant in order to ensure its safe operation in case normal cooling of the core is disrupted, i.e., if circulation stops in part of the circuits or loops during overload or repair work. This speed is determined by the afterheat of the reactor  $N_0$ , by the effective heat capacity of the circuits  $C_{eff}$ , by their heat losses  $N_s$  into the environment, and by the specifications of the equipment involved in the shut-down cooling.

Calculation and experimental investigation of heat removal modes from the core of the shutdown BN-600 reactor were based on the thermal balance formula of the plant with "dry" steam generators of the third circuit:

$$\frac{\Delta t}{\Delta \tau} = \frac{N_0 + N_c + N_e - N_s - N_t}{C_{eff}}, \quad (1)$$

where  $N_0$  is determined by the duration of the operation of the reactor at the rated power and by the time passed after the shutdown, kW [1];  $N_c$  and  $N_e$  stand for the total powers carried into the circuits by all the working main circulators (MC) and by the electric heating of the main zones of the circuits, respectively, kW;  $N_s$  and  $N_t$  stand for the total power of the heat losses from the surface of the equipment of the first and second circuits and the power removed by all the working absorption traps, respectively, kW;  $C_{eff}$  is the effective heat capacity of the loops of the first and second circuits involved in heat removal from the core, kWh/°C;  $\theta_h = \Delta t / \Delta \tau$  is the speed of the heat-up (the shut-down cooling) of the installation, deg C/h.

The circulation of feed water was stopped before the experiments in which the speed of the heat-up of the plant was determined. Steam generators were dried up in the third circuit. At 2-3 h later, a series of temperature measurements were carried out in the first and second circuits during 8-16 h at 15-min intervals. The measurements were made according to the readings of 20 standard thermocouples with the help of an information-computer system "Complex-Uran". Five to ten measurements were carried out in each series in order to reduce the errors, including those due to the fluctuation of temperature. Afterwards, changes in the readings of all the thermocouples in relation to the initial ones were averaged out for every moment of time. In the course of the experiment, the reactor plant was heated up by

---

Translated from Atomnaya Energiya, Vol. 59, No. 1, pp. 60-61, July, 1985. Original article submitted April 16, 1984.

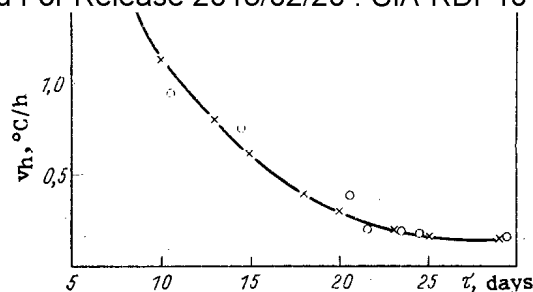


Fig. 1. Speed of the heat-up of the reactor installation when it was shut down in March, 1983;  $\tau$  is the time after the reactor shutdown ( $\times$  designates the calculated values;  $o$  designates the experimental data).

10 to 20°C. With such a measurement technique, systematic errors hardly affected the results. Since the temperature of sodium in the circuits was maintained in the narrow range of 220-240°C, maximum changes of heat losses in the environment did not exceed  $\pm 5\%$  of the average value. The flow rate of sodium in the loops and through the absorption traps was recorded during the experiments, as well as the state of the major equipment involved in heat removal from the core. Experimental speed of the heat-up of the plant was calculated according to the data obtained by the measurements with the use of the equation

$$v_h = \frac{\sum_{i=1}^k (t_{i,m} - t_{i,n})}{k (\tau_m - \tau_n)}, \quad (2)$$

where  $i = [1, 20]$  and  $k$  are the ordinal number and the number of points where temperature was measured respectively;  $t_m$  and  $t_n$ , °C, are the temperature of sodium at times  $\tau_m$  and  $\tau_n$ .

The values contained in expression (1) were determined in order to calculate the speed of the heat-up (the shut-down cooling) of the plant. In order to determine  $N_0$  at any moment of time after the shutdown, all the reactor charge was subdivided into  $m$  groups of fuel assemblies (FA), according to their enrichment and burn-up. Both the last and the preceding operating microperiods were considered, with due regard for the time of the reactor shutdown for recharging in between them. Then

$$N_0 = \sum_{i=1}^n \sum_{j=1}^m N_i g_{ij} A_{ij}, \quad (3)$$

where  $j$  and  $i$  are the ordinal numbers of the group ( $m \leq 6$ ) and of the operating microperiod ( $n \leq 4$ ), respectively;  $A_{ij}$  is the relative power of the  $j$ -th group of FA in the  $i$ -th operating microperiod;  $g_{ij}$  is the relative afterheat of the  $j$ -th group of FA after the  $i$ -th operating microperiod;  $N_i$  is the mean reactor power in the  $i$ -th operating microperiod, MW.

In the calculations,  $N_0$  was taken to be zero, since the main zones of electric heating on the equipment of the sodium circuits were switched off before the experiments in order to increase the accuracy of the calculations. The total amount of heat carried into the circuits by the working MC was determined by the dependence of the flow rate produced by these pumps on the power consumed by them. The contribution of the working absorption traps to the removal of heat  $N_t$  was calculated by their thermal balance, with the use of the known values of coolant flow rate through the absorption traps and of their inlet and outlet temperatures. Recuperators were switched off before the experiments for increasing the difference in the coolant temperature at the absorption traps.

After these parameters of the thermal balance equation (1) are determined, two unknown values remain:  $N_s$  and  $C_{eff}$ . They were determined with the use of the experimental speed of the heat-up for such operating modes of the plant when the equipment was working under identical conditions. Twelve thermal balance equations for different moments of time were obtained (12 experiments). When they were joined in pairs and all the other parameters were



averaged out, the following values of  $N_S$  and  $C_{eff}$  were obtained:  $N_S = 1580$  kW;  $C_{eff} = 1080$  kWh/deg C. The total effective heat capacity is made up of the effective heat capacity of the first circuit and the effective heat capacities of the working loops of the second circuit. In order to subdivide  $C_{eff}$  into separate components, the effective heat capacity of the first circuit and those of each loop of the second circuit were determined according to the design data with the use of the mass of the coolant and of the metal in the constructions. The relation obtained was considered valid to a first approximation and for the conditions of the experiments. In this case, the effective heat capacity of the first circuit  $C_{eff}^I = 620$  kWh/deg C, and that of one loop of the second circuit  $C_{eff}^{II} = 230$  kWh/deg C.

When the distribution of heat losses corresponds to the external surfaces of heat exchange of the circuits, the following heat losses were obtained:  $N_S^I = 540$  kW;  $N_S^{II} = 520$  kW.

Figure 1 shows the experimental and calculated variation of the speed of heat-up of the plant; the maximum deviation of the experimental points from the predicted dependence does not exceed  $\pm 20\%$ .

The effective heat capacity of the circuits depends on the speed of the heat-up as well, since then different amounts of the metal of the equipment can take part in the process of heat exchange, i.e., it can be heated to different depths. Therefore, only the quasistationary mode of heat removal with a speed of the heat-up not greater than 1 deg C/h was considered in the experiments. The process of heat transfer from the core can be somewhat affected by the dead zones of the coolant in the reactor tank and by a leak of the coolant through the closed check valve of the MC of the nonworking loop of the first circuit. The process of the coolant flow over the reactor core has not yet been studied sufficiently [2]; the existing monitoring system of the coolant temperature of the first circuit does not allow us to define such dead zones. Consequently, it was assumed that possible dead areas do not affect the process of the heat-up (the shut-down cooling) of the plant. Due to a low flow rate of coolant through the closed check valve (less than 2% than the total flow rate), its effect on determining the speed of the heat-up was also neglected.

The results obtained were used for evaluating tentatively the speed of the heat-up of the BN-600 plant during subsequent shutdowns for repairing the equipment of the first and third circuits, i.e., when there is no circulation of feed water in the steam generators. The calculated values of the speed of the heat-up again agreed well with the experimental ones, which shows that the method of calculating  $v_h$  was chosen correctly.

The results of the investigation of heat-removal modes of a shut-down reactor made it possible to find the maximum acceptable time of stopping the circulation of feed water in the third circuit for carrying out repair depending on the operating conditions of the equipment involved in the shut-down cooling and on the time elapsed since the moment of the reactor shutdown.

An analysis of the results obtained made it possible to regulate the conditions and to recommend shut-down cooling schemes for removing afterheat from the core of the BN-600 reactor depending on the state of the main equipment of the power unit. It also enables us to plan safely the time of the repair of the equipment with a stopping of forced circulation of sodium in separate loops and of feed water in the third circuit.

Calculations based on the experiments have shown that afterheat can be removed without a heat-up of the plant due to losses into the environment, without a supply of feed water into the steam generators. This is possible after MC of two loops have been working for 25 days, or after those of one loop have been working for 45 days.

#### LITERATURE CITED

1. A. A. Gribin and B. G. Pologikh, "Residual energy liberation of fission products of  $^{235}\text{U}$  by thermal neutrons," *At. Energ.*, 51, No. 1, 16-19 (1981).
2. A. N. Opanasenko and N. N. Shan'gin, "Hydrodynamics of mixing chambers of nuclear power plants," *At. Energ.*, 52, No. 6, 385-389 (1982).

INFLUENCE OF THE CHANGE IN MOISTURE CONTENT OF ATMOSPHERIC AIR ON  
THE DISTRIBUTION OF THE COSMIC-BACKGROUND NEUTRON  
FLUXES ABOVE A WATER SURFACE

E. M. Filippov

UDC 550.35:551.46.083

In [1], it was shown that the cosmic component of the neutron background reflected by a water surface may be used to study the change in salinity of sea water. The present work is an investigation of the influence of the variation in water content in atmospheric air on the cosmic-background neutron flux reflected by the water surface of the sea.

The moisture content of the air  $m$  may be determined from the relation

$$m = \frac{0,622E(t)}{p}, \quad (1)$$

where  $E(t)$  is the saturation buoyancy of water vapor;  $p$  is the atmospheric pressure [2].

The dependence of the moisture content of air on the atmospheric pressure at various temperatures is shown in Fig. 1, from which it follows that, with increase in atmospheric pressure, the moisture content of the air declines slightly in a linear manner. With increase in temperature, however, it sharply increases. The limiting moisture content of atmospheric air is shown in Table 1 for several values of  $p$  and  $t$ . On this basis, it may be concluded that the limiting moisture content depends more strongly on the air temperature than on its pressure. The diffusional parameters for neutrons in air are calculated from the well-known formulas; see [3], for example. From the results in Table 2 and Fig. 2, it follows that the macroscopic cross section increases with increase in moisture content of the air, while the mean neutron paths decrease. With increase in moisture content, the mean lifetime of the thermal neutrons, their diffusion length, and the diffusion coefficients decrease. The air temperature has little influence on the values of  $\tau$  and  $D$ . The dependence of  $L$  on the air temperature is even weaker. Therefore, its spread is not indicated on Fig. 2 at all. The composition of dry air in the calculations is taken to be as follows, %: nitrogen 78, oxygen 21, argon 1. The moisture content is taken into account by adding water in the indicated quantities (Figs. 1 and 2).

The flux density of thermal neutrons  $\varphi_{12}$  close to the water surface is shown in Fig. 3. In [1], it was shown that the function  $\varphi_{12}$  may be conveniently shown as the sum of two functions

$$\varphi_{12} = \varphi_1 + \varphi_2 = \varphi_{10} e^{-H/L} + \varphi_{20} e^{\dots} \quad (2)$$

TABLE 1. Limiting Moisture Content of Atmospheric Air at Various Pressures and Temperatures

Temp., °C	Pressure, mb		
	950	1000	1060
10	0,805	0,765	0,722
20	1,526	1,450	1,368
30	2,782	2,644	2,494

Translated from Atomnaya Energiya, Vol. 59, No. 1, pp. 61-63, July, 1985. Original article submitted June 1, 1984.

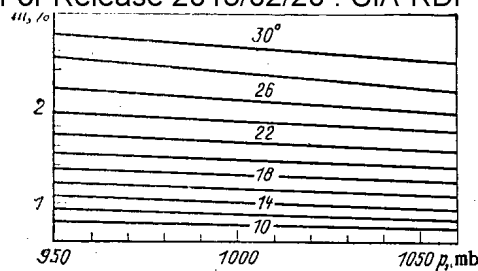


Fig. 1. Dependence of the moisture content of air on the atmospheric pressure at various temperatures.

TABLE 2. Diffusional Parameters for Thermal Neutrons in Air of Various Moisture Contents at a Pressure of 1000 mb and a Temperature of +20°C

Neutron parameters	Moisture content of air, mass %			
	0	0,5	1,0	1,5
$\Sigma_a, \text{cm}^{-1}$	0,0000813	0,0001914	0,0003015	0,0004111
$\Sigma_s, \text{cm}^{-1}$	0,0004754	0,019053	0,0376303	0,056208
$\Sigma, \text{cm}^{-1}$	0,0005567	0,019244	0,0379321	0,0566191
$\lambda_{ti}, \text{cm}$	12300,1	5224,66	3316,75	2432,5
$\lambda_s, \text{cm}$	2103,5	52,48	26,57	17,79
$\lambda, \text{cm}$	1796,3	51,96	26,36	17,66
$\tau, \text{sec}$	0,05591	0,023748	0,015076	0,011057
$D, \text{cm}^2/\text{sec}$	$1,542 \cdot 10^8$	$3,84853 \cdot 10^8$	$1,9265 \cdot 10^6$	$1,3046 \cdot 10^6$
$L, \text{cm}$	2936,75	302,32	170,42	120,1

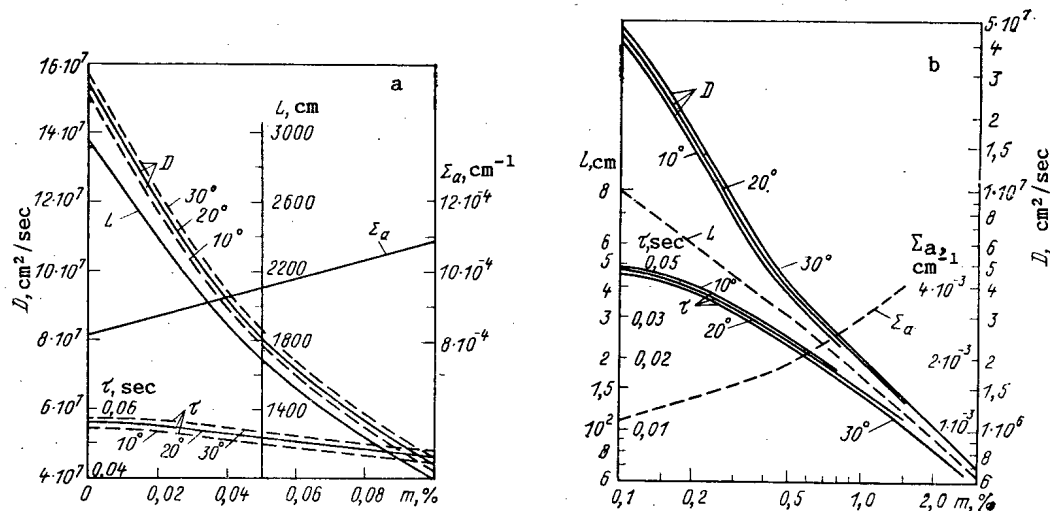


Fig. 2. Dependence of some diffusion parameters of thermal neutrons on the moisture content of air - 0-0.1% (a) and 0.1-0.3% (b) - at various temperatures and a pressure of 1000 mb.

where  $\varphi_{10} = 1.75 \cdot 10^{-3}$ ,  $\varphi_{20} = 2.4 \cdot 10^{-4} \text{ cm}^{-2} \cdot \text{sec}^{-1}$  are the neutron flux densities  $\varphi_1$  and  $\varphi_2$ , respectively, at the water surface ( $H = 0$ );  $b = 1.24 \cdot 10^{-5} \text{ cm}^{-1}$ .

The flux density of thermal neutrons reflected from the water surface is described by the relation

$$\varphi_{\text{re}} = \frac{\eta}{2\Sigma_a L} e^{-H/L}, \quad (3)$$

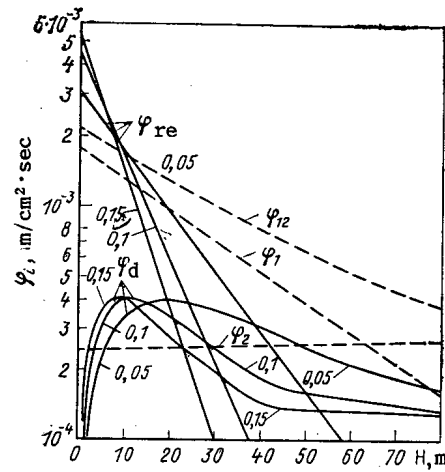


Fig. 3. Dependence of the flux density of thermal neutrons on the height above the water surface:  $\varphi_{12}$ , total flux density, and its components  $\varphi_1$  and  $\varphi_2$ ;  $\varphi_{re}$ , neutron flux density diffusing from the plane surface of sea water at an air moisture content of 0.05, 0.1, and 0.15%;  $\varphi_d$ , diffuse component of the neutron flux density at various air moisture contents.

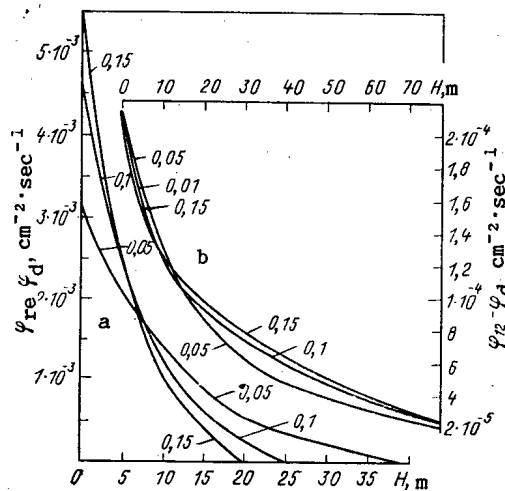


Fig. 4. Dependence of the difference in flux densities  $|\varphi_{re} - \varphi_d|$  of thermal neutrons on the height above the water surface with moisture contents of 0.05, 0.10, and 0.15%.

where  $\varphi = 10^{-3} \text{ cm}^{-2} \cdot \text{sec}^{-1}$  is the flux density of neutrons leaving unit area of the water surface. The form of this function at different air moisture contents is shown in Fig. 3, from which it follows that as the moisture content in air increases, so the decrease in neutron flux density with increase in height becomes more rapid. According to [1], it is advantageous to record the neutrons reflected from the water surface using neutron detectors screened by cadmium from neutrons from the upper halfspace. However, the readings of such screened detectors respond not only to the flux  $\varphi_{re}$  but also to the neutron flux due to diffusion associated with the components  $\varphi_{re}$  and  $\varphi_2$ . The flux density of such neutrons may be estimated from the following relation [1]

$$\varphi_d = \frac{1}{2} \left\{ \frac{\varphi_{10} H}{L} e^{-H/L} + \frac{\varphi_{20}}{1 + bL} (e^b - e^{-H/L}) \right\}. \quad (4)$$

The function  $\varphi_d$  is shown as a function of the height  $H$  for various air moisture contents in Fig. 3. With increase in moisture content of the air, the maximum of the function  $\varphi_d(H)$  moves closer to the water surface. However, the magnitude of the maximum of all these functions is approximately the same.

Useful information on the salinity of sea water may be obtained in determining the neutron flux due to the flux difference  $\varphi_{re} - \varphi_d$ . Its dependence on the height  $H$  (Fig. 4a) shows that, with decrease in the moisture content of the air, the height from the water surface at which information on the salinity of sea water must be obtained increases. The influence of the air moisture content on the recorded neutron flux is at its smallest when the detector is placed at a height of 7-8 m above the water surface.

An interfering factor here is the neutron flux from the upper halfspace which is incident on the detector from below on account of the diffusion process,  $\varphi_{12} - \varphi_d$ . This function is shown as a function of the height  $H$  and the air moisture content  $m$  in Fig. 4b. As is evident, at a height of no more than 12 m, it does not greatly depend on the variation in air moisture content.

The method of taking account of the measurement errors in the neutron flux reflected from the water surface was described in [1]. On the basis of this method, it is simple to show that, in determining the salinity of sea water at a height of 20 m using a detector of area 8 m<sup>2</sup> and efficiency 50%,  $\pm 0.5\%$  variation in a small moisture content (0.05%) does not lead to perceptible errors in measuring the salinity of the water, and may be neglected.

The effect of variation in air moisture content on the measurement of the thermal-neutron flux reflected from a water surface is least at a height of 7-8 m. In measuring the neutron flux at other heights, the air moisture content must be independently taken into account, by recording it psychrometrically, for example. The given data allow the necessary corrections to be calculated and introduced in this case. The method proposed for taking account of the influence of variation in moisture content of air is also useful in experimental investigations of neutron fluxes of cosmic (natural) and artificial origin for solving scientific and practical problems.

#### LITERATURE CITED

1. E. M. Filippov, "Prospects for using cosmic-background neutrons to study sea water," *At. Energ.*, 56, No. 4, 240-243 (1984).
2. V. A. Savich, *Psychrometric Tables* [in Russian], Gidrometeoizdat, Leningrad (1957).
3. E. M. Filippov, *Neutron Methods of Studying Sea Water* [in Russian], Paper No. 3180-83 Deposited at VINITI, Moscow (1983).

A PYROELECTRIC DETECTOR OF GAMMA RADIATION WITH COMPENSATION  
FOR THE COMPTON-ELECTRON CURRENT

V. A. Borisenok, E. Z. Novitskii,  
E. V. Vagin, S. A. Pimanikhin,  
and V. D. Sadunov

UDC 539.1.074:537.226/.227

The authors of [1-4] have shown that when the characteristics of high-energy  $\gamma$ -radiation are measured with a pyroelectric detector having a sensitive element in the form of a plate capacitor filled with a pyroactive material (pyrocapacitor), the output signal amplitude is given by the pyroeffect and, in addition, by the charging effect resulting from the transfer of Compton electrons. The latter develop in the interaction of the radiation with the detector and induce a charge on the plates of the pyrocapacitor. In the experiment of

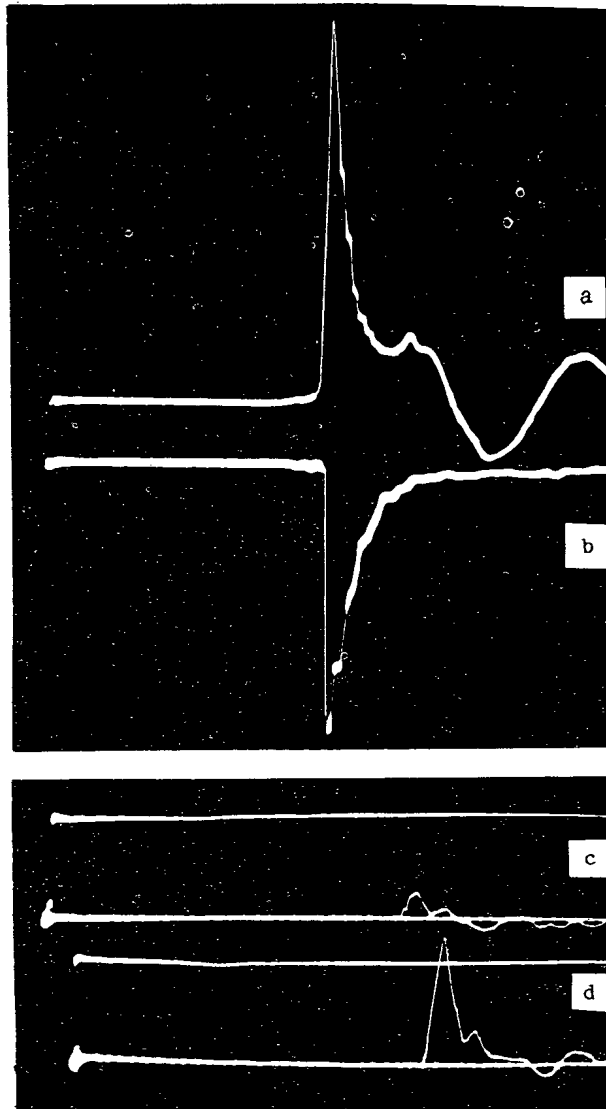


Fig. 1. Oscillograms of the detector signals.

Translated from Atomnaya Energiya, Vol. 59, No. 1, pp. 63-64, July, 1985. Original article submitted June 11, 1984.

Declassified and Approved For Release 2013/02/20 : CIA-RDP10-02196R000300070001-4  
[5] In a pulsed nuclear reactor, the signal contribution resulting from the Compton electron current amounted to ~20%. A higher contribution of this type must be expected in measurements made in fields of collimated radiation.

In order to reduce the contribution by the Compton electron current, the authors of [2] suggested for pyroelectric gamma detectors to use transverse sensitive elements, provided that the radiation propagates parallel to the plates of the pyrodetector and perpendicular to the vector of polarization of the material. But an experimental confirmation of the efficiency of operation of such a detector has not been described.

In order to eliminate the Compton component of the current, the authors of [4] have proposed to use a compensating double-element pyroelectric detector. The sensitive element of such a detector consists of two identical pyrocapacitors in which the directions of polarization are opposite. The pyrocapacitors can be connected in series or in parallel, depending upon the characteristics required (sensitivity, time resolution).

The theoretical analysis of the problem [4] has shown that under identical conditions of irradiation of pyrocapacitors, the compensation for the Compton-electron current takes place in the double-element detector because the polarity of the pyroelectric signal in the external circuit of each of the pyrocapacitors depends only upon the direction of polarization, whereas the signal generated by the Compton-electron current depends upon the direction of propagation of the radiation. But an experimental confirmation of the efficiency of operation of the compensated detector has not been outlined.

The goal of our work was to experimentally investigate the efficiency of operation of a compensating double-element detector in measurements of the characteristics of collimated gamma radiation.

We compared for this purpose the detector signals (see Fig. 1) with sensitive elements of PKR-1 piezoceramic material [6] without compensation (a) and with compensation (b) for the Compton-electron current. In each case the contribution of the Compton electrons was determined by comparing the readings of the operational (a and d) and background (b and c) detectors. The sensitive element of the detector without compensation was a disk with a diameter of  $20 \times 2$  mm. In the case of the detector with compensation, for the purpose of obtaining compactness the element was given the shape of a coaxially located disk (diameter  $20 \times 2$  mm) and a ring; the components of the element were connected in parallel. Silver electrodes were applied to the plane surfaces of the disk and the ring by burning the silver in. The area of the electrodes and the thickness of the disk and the ring were about the same. The sensitive elements of the background detectors were made from an unpolarized piezoceramic material. The electric constants of all detectors were the same as a consequence of an appropriate selection of the load resistors.

All detectors were simultaneously irradiated by a pulse of collimated gamma radiation. The oscillograms of the output signals are shown in Fig. 1. The structure of the signals is given by the contributions of the pyroeffect and the Compton-electron current; in the case of the operational detectors (Figs. 1a and d), the piezoelectric "response" is clearly visible on the structure of the signals. According to [7], the piezoelectric response manifests itself under irradiation conditions leading to a thermal shock in the material of the sensitive element; such a thermal shock was actually obtained in the experiment. The piezoelectric response is described by a periodic signal having a frequency equal to the frequency of the mechanical vibrations of the sensitive element.

A comparison of the signal amplitudes has shown that this design of the sensitive element makes it possible to reduce the Compton-electron current from 70% in the detector without compensation to 20% in the detector with compensation. The degree of compensation can be even higher when care is taken that the surface areas and the thicknesses of the components of the sensitive element are equal and that the properties of the piezoceramic material are extremely uniform.

Let us note, in conclusion, that a pyrodetector with a sensitive element of the design considered can also be used to record other types of radiation.

#### LITERATURE CITED

1. Z. A. Al'bikov, A. I. Veretennikov, and O. V. Kozlov, Detectors of Pulsed Ionizing Radiation [in Russian], Atomizdat, Moscow (1978).

- Declassified and Approved For Release 2013/02/20 : CIA-RDP10-02196R000300070001-4
2. A. Ya. Strakovskaya and L. G. Klemenchukskii, "Pyroelectric detectors of bremsstrahlung pulses," *At. Energ.*, 51, No. 1, 37 (1981).
  3. E. Z. Novitskii and V. A. Borisenok, "The Effect of Pulsed Ionizing Radiation upon Pyroelectric Materials and Pyrodetectors. I. The Pyroelectric Response" [in Russian], *Problems of Atomic Science and Technology, Series Nuclear Instrument Design*, No. 3(51), pp. 61-69 (1982).
  4. R. Ya. Strakovskaya, *Principles of Pyroelectric Dosimetry* [in Russian], Naukova Dumka, Kiev (1983).
  5. B. A. Levin, "Currents generated in pyroelectric materials under gamma irradiation," *At. Energ.*, 53, No. 6, 401 (1982).
  6. E. G. Fesenko, A. Ya. Dantsiger, and O. N. Razumovskaya, *New Piezoceramic Materials* [in Russian], Rostov-on-Don (1983).
  7. V. A. Borisenok, E. Z. Novitskii, V. D. Sadunov, and A. D. Feronov, "The piezoelectric response of pyroelectric materials to pulses of ionizing radiation," in: *Seignette-Electric and Piezoelectric Materials* [in Russian], Kalinin (1983), pp. 32-39.

POLYNOMIAL REPRESENTATION OF THE BREMSSTRAHLUNG SPECTRA OF A THICK TARGET FOR ELECTRONS OF ENERGY 10-22 MeV

V. E. Zhuchko and Zen Chan Uk

UDC 539.124.17

Analysis of most experiments in which bremsstrahlung is used requires a knowledge of the  $\gamma$ -ray spectrum for various energies of the incident electrons as a function of the thickness and material of the retarding target. In a series of experiments, it has been shown that the greatest yield of forward bremsstrahlung is observed using thick targets ( $\sim 0.3$ - $0.5$  radiational length). The radiation spectrum of these targets cannot be regarded as equivalent to the Schiff spectrum usually used for thin targets [1]; therefore, the method described in [2, 3] is used for the calculation.

Under the assumption that the "elementary" radiation spectrum is known, i.e., the radiation spectrum of an electron in a single scattering event, the bremsstrahlung spectra of all the target are added, taking account of the electron scattering, the absorption of radiation by the target material, the probability of photon emission at a specified angle, and the energy loss and absorption of the electrons. With an error of  $\sim 10$ - $15\%$ , over the whole of the energy range  $E_\gamma$  and the electron-energy range 1-30 MeV, the theoretical spectra coincide with the existing experimental data. To simplify the subsequent use of the calculation results, an attempt is made to represent in polynomial form the set of bremsstrahlung spectra for targets used on the MT-22 microtron of the Laboratory of Nuclear Reactions, JINR [4], which consist of 0.2 cm tungsten and 3 cm aluminum. The calculation is performed for electron energies  $10 \text{ MeV} \leq E_e \leq 22 \text{ MeV}$  and  $\gamma$ -quantum energies  $1 \text{ MeV} \leq k \leq 0.95 E_e$ . The bremsstrahlung yield values obtained are written in the form

$$d^2N/dk d\Omega = \sum_{i,j=0}^{i=5, j=4} A_{ij} E_e^i / k^j, \quad (1)$$

where  $d^2N/dk d\Omega$  is the yield of forward bremsstrahlung,  $\text{MeV}^{-1} \cdot \text{sr}^{-1} \cdot \text{electron}^{-1}$ ;  $A_{ij}$  are the coefficients of the expansion;  $E_e$ ,  $k$  are the electron and bremsstrahlung energies, respectively, MeV.

The PS11 program is used to calculate  $A_{ij}$  [5]. Values of the coefficients are shown in Table 1. To reduce the degree of the polynomial and increase the accuracy of the approximation,  $A_{ij}$  are calculated separately for the ranges  $1 \text{ MeV} \leq k \leq E_e/2$  and  $E_e/2 \leq k \leq 0.95 E_e$  which corresponds to the upper and lower values of the coefficient in Table 1. The error of the approximation is no worse than 1% for  $1 \text{ MeV} \leq k \leq E_e/2$  and 10% for  $E_e/2 \leq k \leq 0.95 E_e$ . In Fig. 1, as an example, bremsstrahlung spectra are shown for the electron energies, together

Translated from *Atomnaya Energiya*, Vol. 59, No. 1, pp. 65-66, July, 1985. Original article submitted October 1, 1984.



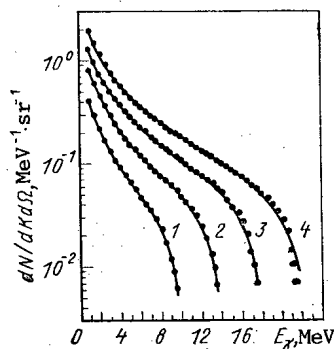


Fig. 1. Bremsstrahlung spectra calculated by the method of [2, 3] (dotted curves) and approximated by the polynomial in Eq. (1) (continuous curves) for electron energies of 10 (1), 14 (2), 18 (3), and 22 (4) MeV.

TABLE 1. Numerical Values of the Coefficients  $A_{ij}$

$j$	$i$					
	0	1	2	3	4	5
0	$1,58874866 \cdot 10^{-1}$	$-3,98508540 \cdot 10^{-2}$	$3,49350585 \cdot 10^{-3}$	$-1,82726063 \cdot 10^{-4}$	$4,98845764 \cdot 10^{-6}$	$-5,72913821 \cdot 10^{-8}$
1	$5,89004864 \cdot 10^{-1}$	$-1,83740867 \cdot 10^{-1}$	$1,27899598 \cdot 10^{-2}$	$-4,75428530 \cdot 10^{-4}$	$1,08518492 \cdot 10^{-5}$	$-1,17597727 \cdot 10^{-8}$
2	$-5,43166997 \cdot 10^{-1}$	$5,50414649 \cdot 10^{-2}$	$3,34043133 \cdot 10^{-3}$	$5,38904961 \cdot 10^{-5}$	0	0
3	$-12,8214465$	$2,93957753$	$-0,103672612$	$1,12582214 \cdot 10^{-3}$	0	0
4	$0,982709333$	$-2,72876857 \cdot 10^{-2}$	$-1,59995949 \cdot 10^{-3}$	0	0	0
5	$0,848074681$	$-17,6927279$	$0,350197163$	0	0	0
6	$-1,02405363$	$1,21623969 \cdot 10^{-2}$	0	0	0	0
7	$-89,1116537$	$30,8088924$	0	0	0	0
8	$0,392921989$	0	0	0	0	0
9	$-328,910953$	0	0	0	0	0

with their approximation by the polynomial in Eq. (1).

When using the polynomial in Eq. (1) to analyze the experimental results, there appears the possibility of taking account of the influence of the degree to which the beam is monoenergetic on the form of the bremsstrahlung spectrum, which is necessary in deriving the cross sections of the nuclear reactions from the reaction yields. This may be done as follows:

$$d^2N/dk d\Omega = \int_0^{+\infty} d^2N(E_e)/dk d\Omega f(\bar{E}_e - E_e) dE_e,$$

where  $\bar{E}_e$  is the mean electron energy in the beam;  $f(\bar{E}_e - E_e)$  is the form of the electron energy distribution in the beam. In the simplest case, it may be regarded as Gaussian.

The method here proposed may be used to represent bremsstrahlung spectra in a different energy range and for targets of different composition.

#### LITERATURE CITED

1. L. Schiff, Phys. Rev., **83**, 52 (1951).
2. Ferdinand et al., Nucl. Instrum. Mater., **107**, 329 (1973).
3. V. E. Zhuchko and Yu. M. Tsipenyuk, At. Energ., **39**, No. 1, 66 (1975).
4. A. G. Belov et al., JINR Preprint R9-82-301 [in Russian], Dubna (1982).
5. V. V. Galaktionov et al., Library of Programs in Fortran and the Automatic Code Madlen for a BESM-6 Computer [in Russian], Vol. 2, JINR, Dubna (1977), p. 321.

# HEAT-TRANSFER COEFFICIENT WITH GLANCING FLOW AROUND FUEL ELEMENTS AND TUBES

Yu. S. Yur'ev and A. D. Efanov

UDC 536.24

In calculating heat exchangers and steam generators with complex heat-carrier motion in the intertube space and in calculating fuel assemblies with partial blocking of the cross section, the heat-transfer coefficient is determined as a function of the angle of attack of the flux flowing around the tube or fuel element [1]. Recommendations following from empirical dependences obtained in [2] for heat carrier with  $Pr \approx 1$  and in [3] for  $Pr \ll 1$  (liquid metals) are used here. The deficiency of these recommendations is the lack of a single universal formula expressing the dependence of the heat-transfer coefficient on the angle of attack from  $\varphi = 0$  (longitudinal flow) to  $\varphi = \pi/2$  (transverse flow), which is required for numerical computer calculations.

Analysis of experimental data on the local hydrodynamics and heat transfer obtained in [2] and also at the Power Physics Institute by an electromagnetic method [4] permits the construction of a schematic model of laminar heat-carrier flow with glancing flow around a bundle of tubes or fuel elements and the formulation, on this basis, of a unified dependence of the heat-transfer coefficient on the angle of attack.

Consider the features of the model of laminar flow with glancing flow around a checkerboard or corridor bundle (Fig. 1).

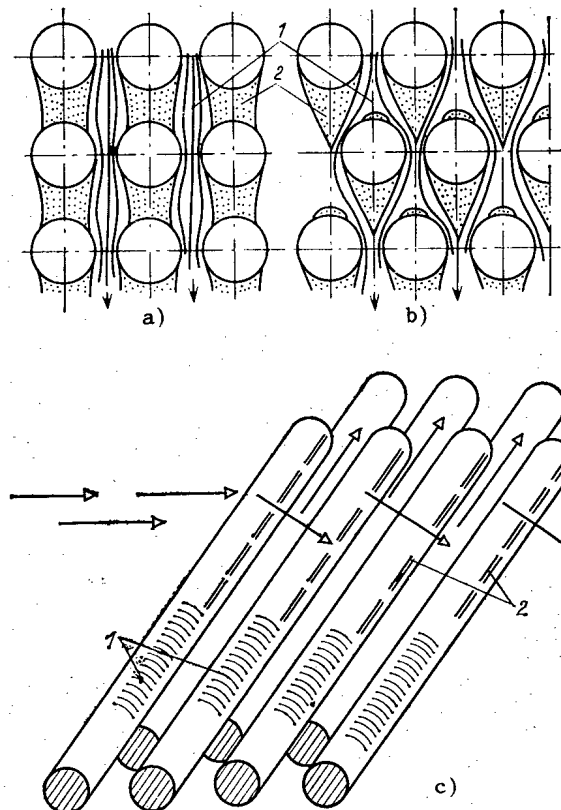


Fig. 1. Corridor (a) and checkerboard (b) bundles in glancing (c) heat-carrier flow: 1) zone of predominantly transverse flow; 2) zone of predominantly longitudinal flow.

Translated from *Atomnaya Energiya*, Vol. 59, No. 1, pp. 66-67, July, 1985. Original article submitted December 18, 1984.

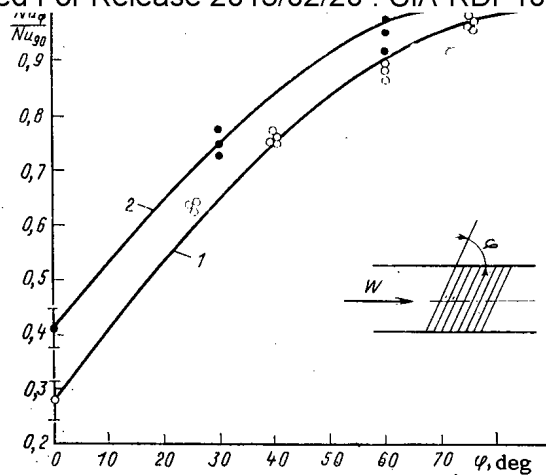


Fig. 2. Comparison of curves calculated from Eq. (4) for air (1) and liquid metal (2) with the experimental data of [2] (open circles) and [3] (filled circles).

Longitudinal liquid motion is realized basically in the "dark" zones of the intertube space, beyond the stern part of the tubes; transverse motion predominates in narrow gaps between tubes in the path of the flow (Fig. 1c). Therefore, it may be supposed that part of the perimeter  $\varepsilon_1$  of the tube is in a transverse flux ( $\alpha_1$ ) and part of the perimeter  $\varepsilon_2 = 1 - \varepsilon_1$  is in a longitudinal flux ( $\alpha_2$ ). It follows from the heat-balance condition that the mean heat-transfer coefficient is

$$\bar{\alpha} = \alpha_1 \varepsilon_1 + \alpha_2 \varepsilon_2. \quad (1)$$

Local heat transfer with transverse and longitudinal flow around parts of the perimeter is determined by the "acting" velocities  $w_1 = w \sin \varphi$  and  $w_2 = w \cos \varphi$  according to the dependences  $Nu_1 \sim Re_1^n$ ,  $Nu_2 \sim Re_2^m$ , and hence

$$\bar{\alpha} = \alpha_{tra} (\sin \varphi)^n (\varepsilon_1 / \varepsilon_1^{tra})^{1-n} + \alpha_{long} (\cos \varphi)^m (1 - \varepsilon_1)^{1-m}, \quad (2)$$

where  $\alpha_{tra}$ ,  $\alpha_{long}$  are the heat-transfer coefficients with purely transverse and purely longitudinal flow around the bundle (with the same velocity of the incoming flux reaching the bundle).

If the simplest linear dependence is assumed:

$$\varepsilon_1 = \varepsilon_1^{tra} (2\varphi/\pi), \quad \varepsilon_1^{tra} = 0.5,$$

the desired function is obtained:

$$\bar{\alpha} = \alpha_{tra} (\sin \varphi)^n (2\varphi/\pi)^{1-n} + \alpha_{long} (\cos \varphi)^m (1 - \varphi/\pi)^{1-m}, \quad (3)$$

which is in satisfactory agreement with the experimental data of [2] and [3] (Fig. 2) in the form

$$\frac{Nu_{\varphi}}{Nu_{90}} = (\sin \varphi)^{0.5} (2\varphi/\pi)^{0.5} + \left( \frac{\alpha_{long}}{\alpha_{tra}} \right) (\cos \varphi)^{0.8} (1 - \varphi/\pi)^{0.2}. \quad (4)$$

$$\frac{\alpha_{\text{long}}}{\alpha_{\text{tra}}} = \begin{cases} 0.28 \pm 0.04 & \text{for } Pr \approx 1; 1.2 \leq s/d \leq 1.5; \\ & 10^3 \leq Re \leq 10^5; \\ \frac{0.24}{\sqrt{\epsilon}} \pm 0.04 & \text{for } Pr \ll 1; 1.2 \leq s/d \leq 1.5; \\ & 10 \leq Pe \leq 600, \end{cases}$$

where  $\epsilon$  is the volume fraction of intertube space;  $s/d$  is the relative spacing of the bundle; these dependences are obtained on the basis of [5].

#### LITERATURE CITED

1. V. I. Subbotin et al., Computer Solution of Problems of Reactor Thermal Physics [in Russian], Atomizdat, Moscow (1979).
2. A. A. Zhukauskas, Convective Transfer in Heat Exchangers [in Russian], Nauka, Moscow (1982).
3. V. M. Borishanskii et al., "Heat transfer of bundles of rods at an angle to an incoming liquid-metal flow," *Inzh.-Fiz. Zh.*, **19**, No. 6, 977-983 (1970).
4. V. M. Budov et al., "Theoretical and experimental investigation of thermophysical processes with complex longitudinal-transverse flow of heat carrier in intermediate heat-exchangers of fast reactors," in: *Heat Transfer and Hydrodynamics of Single-Phase Flow in Rod Bundles* [in Russian], Nauka, Leningrad (1979), pp. 56-68.
5. P. L. Kirillov, Yu. S. Yur'ev, and V. P. Bobkov, Handbook on Thermohydraulic Calculations (Nuclear Reactors, Heat Exchangers, Steam Generators) [in Russian], Energoatomizdat, Moscow (1984).

#### USING CADMIUM TELLURIDE DETECTORS FOR THE X-RAY FLUORESCENCE

##### ANALYSIS OF URANIUM SOLUTIONS

V. V. Berdikov, A. V. Vasil'ev,  
O. I. Grigor'ev, B. S. Iokhin,  
and A. Kh. Khusainov

UDC 543.426

The x-ray fluorescence technique, particularly its version without a crystal, recently has been used more and more in systems for the analytic monitoring of the nuclear fuel cycle [1] because the technique makes it possible to determine the concentration of elements in objects to be analyzed without a preliminary chemical preparation of the sample; the technique is distinguished by adequate precision, rapid execution, and sensitivity. A system of x-ray fluorescence analysis without a crystal can also be used for continuous monitoring without taking samples. For example, the authors of [2] have reported on the introduction of x-ray fluorescence equipment without a crystal in three radiochemical plants of the USA for the purpose of continuous measurements of the uranium concentration (in the range of 0.1-500 g/liter) in the production lines proper; detectors of super-pure germanium are used to record the fluorescence radiation. When such a monitoring is introduced (it may be called "remote monitoring"), uncooled semiconductor detectors, e.g., detectors made from CdTe or  $\text{HgI}_2$ , are, in our opinion, more suitable. With these detectors, the dimensions of the apparatus are reduced, the servicing is facilitated, and monitoring is possible at points of limited access.

In our work we studied the possible use of a BDTK-1 detector unit on the basis of CdTe in apparatus for x-ray fluorescence analysis without a crystal for the purpose of analyzing solutions with low uranium concentrations (less than 100 mg/liter). Such apparatus can be employed to monitor certain waste solutions and may be used, in particular, as a threshold monitor.

The experimental setup for x-ray fluorescence analysis without a crystal resembles the previously described system of [1] with an Si(Li) detector. The system comprises a low-power

---

Translated from *Atomnaya Energiya*, Vol. 59, No. 1, pp. 67-68, July, 1985. Original article submitted November 19, 1984.

voltage source, a scattering chamber with a cylindrical assembly of pyrographite crystals, a BDTK-1 unit (CdTe detector, preamplifier, microcooler, and supply source of these units), a spectrometer amplifier, and a multichannel analyzer on the basis of a minicomputer. The scattering chamber serves for the initial energy selection of the radiation from the sample. In this way the exciting radiation scattered at the sample can be suppressed by a factor of about 100 (compared with the fluorescence of the  $UL_{\alpha}$  emission of uranium). This is necessary for reducing the background in the region of the analytic peak generated in recording scattered radiation; the background develops in such recording as a consequence of incomplete charge collection in the detector.

The resolving power of such a detector unit amounts to  $\sim 1.4$  keV at an energy of 14 keV. Therefore, restrictions are imposed on the possible useful range of the setup: it is practically impossible to determine uranium concentrations in the presence of comparable amounts of plutonium, neptunium, rubidium, and bromine.

The sensitive detector surface is  $S = 30 \text{ mm}^2$ . The counting rate in the  $UL_{\alpha}$  peak is  $70 \text{ sec}^{-1}$  at an uranium concentration of 500 mg/liter in a solution. In this case the background under the peak is  $5.3 \text{ sec}^{-1}$ , which corresponds to a uranium detection limit of  $\sim 1.5$  mg/liter with an analysis time of 10 min. This background under the peak results mainly from incomplete charge collection (the so-called "tail" of peaks of scattered exciting radiation reflected by the pyrographite assembly in the second order of diffraction). When a detector with a smaller surface is employed, the relative importance of the background increases and this implies a large increase in the detection limit ( $\sim 3$  mg/liter at  $S = 12 \text{ mm}^2$ ). When a radioisotope is used as the exciting source, the setup becomes simplified but the lower intensity of such a source leads to a deterioration of the detection limit by one order of magnitude ( $\sim 11$  mg/liter with an activity of  $2.5 \cdot 10^9$  Bq of an annular  $^{109}\text{Cd}$  source). Let us note that the use of the BDTK-1 detector unit in the system without a crystal but of conventional geometry, i.e., without a scattering chamber, does not render acceptable detection limits because the background above the analytic peak rises sharply (the detection limit exceeds 100 mg/liter in the excitation with both the tube and the radioisotope source).

In the setup described, the solution to be analyzed (sample volume  $3.5 \text{ cm}^3$ ) is inserted into a stainless steel cuvette with a 100- $\mu\text{m}$ -thick Teflon-film window. A cuvette of similar design but of the flow-type is suitable for continuous monitoring. The multichannel analyzer should be replaced by a set of adjustable single-channel analyzers the information of which can be processed with a microcomputer.

#### LITERATURE CITED

1. V. V. Berdikov and B. S. Iokhin, "A highly sensitive x-ray fluorescence technique of determining concentrations of heavy elements in solutions," *Radiokhimiya*, 24, No. 4, 525 (1982).
2. D. Camp and W. Ruther, "X-ray unit tracks heavy metals," *Nucl. Eng. Int.*, 28, No. 337, 50 (1983).

HALF-LIVES OF THE SPONTANEOUS FISSION OF  $^{239}\text{Pu}$  AND  $^{241}\text{Pu}$ 

A. A. Druzhinin, V. N. Polynov,  
A. M. Korochkin, E. A. Nikitin,  
and L. I. Lagutina

UDC 539.144.6+539.173.7

It is a well-known fact that the probability of spontaneous fission of the odd plutonium isotopes is smaller than that of the even isotopes by a factor of  $10^5$ - $10^6$  [1-4]. Therefore, samples of high purity are needed for experimental measurements of the half-lives of spontaneous fission of the odd isotopes. In the case under consideration, samples of super-pure  $^{239}\text{Pu}$  and  $^{241}\text{Pu}$  were available. The samples had been obtained by electromagnetic separation with the S-2 separator. Therefore the experimental determination of the periods of spontaneous fission of these isotopes was possible. The isotope composition of the plutonium samples was determined with mass spectrometry. The  $^{238}\text{Pu}$  concentration was measured with  $\alpha$ -spectrometry. The results are compiled in Table 1.

Targets of the plutonium isotopes were prepared by electrodeposition from isopropyl alcohol solutions onto metal substrates (platinum, nickel) with a diameter of 25 mm and a thickness of 0.2 mm. The active layer had a diameter of  $22 \pm 0.1$  mm.

TABLE 1. Isotope Composition of the Plutonium Samples

Sample	Concn. ratio of the nuclei				
	$^{238}\text{Pu}$	$^{239}\text{Pu}$	$^{240}\text{Pu}$	$^{241}\text{Pu}$	$^{242}\text{Pu}$
$^{239}\text{Pu}$ $^{241}\text{Pu}$	$(1,3 \pm 0,1) \cdot 10^{-6}$ —	1 $\sim 3,6 \cdot 10^{-6}$	$(2,41 \pm 0,04) \cdot 10^{-5}$ $(1,8 \pm 0,5) \cdot 10^{-6}$	$(1,35 \pm 0,03) \cdot 10^{-5}$ 1	$(1,2 \pm 0,4) \cdot 10^{-7}$ $< 5 \cdot 10^{-6}$

TABLE 2. Results of Measurements of the Number of Fission Events in  $^{239}\text{Pu}$  and  $^{241}\text{Pu}$  Targets

Sample	Number of the target	Mass ( $\mu\text{g}$ ) of main isotope in target	Total number of fissions in target	Number of induced fission events	No. of spontaneous fission events of admixed isotopes			No. of spontaneous fission events of the main isotope
					$^{238}\text{Pu}$	$^{240}\text{Pu}$	$^{242}\text{Pu}$	
$^{239}\text{Pu}$	1	$662 \pm 20$	$188 \pm 14$	$24 \pm 3$	$13 \pm 1$	$88 \pm 4$	$1 \pm 0,3$	$62 \pm 15$
	2	$835 \pm 25$	$189 \pm 14$	$24 \pm 3$	$13 \pm 1$	$90 \pm 5$	$1 \pm 0,3$	$61 \pm 15$
	3	$1830 \pm 50$	$406 \pm 20$	$53 \pm 6$	$28 \pm 3$	$196 \pm 10$	$2 \pm 0,7$	$127 \pm 23$
$^{241}\text{Pu}$	1	$190 \pm 6$	$18 \pm 4$	$6 \pm 2$	—	$2 \pm 0,6$	$< 8$	$\sim 2$

TABLE 3. Periods of the Spontaneous Fission of  $^{239}\text{Pu}$  and  $^{241}\text{Pu}$ 

Isotope	Number of the target	Exposure time (sec)	$\alpha$ activity (Bq) of the main isotope	No. of spontaneous fission events of the main isotope	Period (years) of spontaneous fission
$^{239}\text{Pu}$	1	$1,27 \cdot 10^7$	$1,52 \cdot 10^6$	$62 \pm 15$	$\left. \begin{array}{l} (7,5 \pm 1,8) \cdot 10^{15} \\ (7,7 \pm 1,9) \cdot 10^{15} \\ (8,1 \pm 1,5) \cdot 10^{15} \\ \leq 6 \cdot 10^{16} \end{array} \right\} (7,8 \pm 1,6) \cdot 10^{15}$
	2	$1,02 \cdot 10^7$	$1,92 \cdot 10^6$	$61 \pm 15$	
	3	$1,02 \cdot 10^7$	$4,20 \cdot 10^6$	$127 \pm 23$	
$^{241}\text{Pu}$	1	$1,15 \cdot 10^7$	$1,7 \cdot 10^4$	$\sim 2$	

Translated from Atomnaya Energiya, Vol. 59, No. 1, pp. 68-69, July, 1985. Original article submitted December 7, 1984.

The number of plutonium isotopes in the targets was measured through the  $\alpha$ -activity with the aid of a counter containing a DKPs-350 silicon detector in small solid-angle geometry. The measurement error was 2-3%.

The fission fragments were recorded with solid-state track detectors of synthetic mica (TU-41-955-71). The efficiency of recording fission fragments in the case of tight contact of the mica with the target was measured with the aid of a  $^{252}\text{Cf}$  standard and amounted to  $0.96 \pm 0.02$ .

The contribution by induced fission was monitored during the exposure time with the aid of an analogous target of high-purity  $^{235}\text{U}$  for which the spontaneous fission of uranium isotopes can be disregarded as small ( $5.8 \cdot 10^{-9}$  fissions/(sec·mg) [5]). Under the conditions of the measurements, the induced fission of plutonium isotopes amounted to  $(2.8 \pm 0.3) \cdot 10^{-6}$  fissions/(sec·mg). The results of measurements of the number of spontaneous fission events in  $^{239}\text{Pu}$  and  $^{241}\text{Pu}$  samples are listed in Table 2.

The half-lives of spontaneous fission of  $^{239}\text{Pu}$  and  $^{241}\text{Pu}$  were calculated from the measured ratio of the number of  $\alpha$  decays to the number of spontaneous fission events and the known values of  $\alpha$  decay periods of those isotopes (i.e.,  $(2.411 \pm 0.003) \cdot 10^4$  years and  $(6.04 \pm 0.06) \cdot 10^5$  years, respectively [4]). The results of the calculations are listed in Table 3.

The value obtained for the half-life of the spontaneous fission of  $^{239}\text{Pu}$  was  $(7.8 \pm 1.6) \cdot 10^{15}$  years, which is higher than the value measured in 1952 by Segre [6] ( $5.5 \cdot 10^{15}$  years). However, it has not been stated in [6] whether corrections for the induced fission of  $^{239}\text{Pu}$  during the long time of the measurements were introduced: twelve spontaneous fission events were observed during  $3.6 \cdot 10^7$  sec.

The value of  $\sim 6 \cdot 10^{16}$  years which was found for the half-life of spontaneous fission of  $^{241}\text{Pu}$  must be considered an estimate. This value will be refined in the future after a determination of the concentration of the  $^{242}\text{Pu}$  admixture has been made.

#### LITERATURE CITED

1. V. M. Gorbachev, Yu. S. Zamyatnin, and A. A. Lbov, The Basic Characteristics of the Isotopes of the Heavy Elements [in Russian], Atomizdat, Moscow (1975), p. 208.
2. A. Lorenz, INDC(NDS)-96/N, August 1978.
3. V. M. Gorbachev, Yu. S. Zamyatnin, and A. A. Lbov, The Interaction of Radiation with Heavy Nuclei of Elements and the Fission of Nuclei [in Russian], Atomizdat, Moscow (1976), p. 462.
4. V. M. Surin and É. F. Fomushkin, "The Half-Lives of the Long-Lived Isotopes of Trans-actinium Elements (from  $^{228}\text{Th}$  to  $^{257}\text{Fm}$ )" [in Russian], Problems of Atomic Science and Technology, Series: Nuclear Constants, No. 4(48), pp. 3-38 (1982).
5. H. Gunten, A. Grütter, H. Reist, and M. Baggenstos, "Ground-state spontaneous-fission half-lives of uranium isotopes," Phys. Rev., 23, No. 3, 1110 (1981).
6. E. Segre, "Spontaneous fission," Phys. Rev., 86, No. 1, 21 (1952).

# How To Comply With The New Copyright Law

*Participation in the Copyright Clearance Center (CCC) assures you of legal photocopying at the moment of need.*

Libraries everywhere have found the easy way to fill photocopy requests legally and instantly, without the need to seek permissions, from more than 3000 key publications in business, science, humanities, and social science. You can:

*Fill requests for multiple copies, interlibrary loan (beyond the CONTU guidelines), and reserve desk without fear of copyright infringement.*

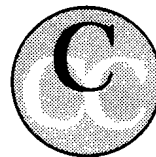
Supply copies from CCC-registered publications simply and easily.

The Copyright Clearance Center is your one-stop place for on-the-spot clearance to photocopy for internal use.

Its flexible reporting system accepts photocopying reports and returns an itemized invoice. You send only one convenient payment. CCC distributes it to the many publishers whose works you need.

And, you need not keep any records, the CCC computer will do it for you. Register now with the CCC and you will never again have to decline a photocopy request or wonder about compliance with the law for any publication participating in the CCC.

To register or for more information, just contact:



## Copyright Clearance Center

21 Congress Street  
Salem, Massachusetts 01970  
(617) 744-3350

a not-for-profit corporation

NAME	TITLE		
ORGANIZATION			
ADDRESS			
CITY	STATE	ZIP	
COUNTRY	TELEPHONE		



# CHANGING YOUR ADDRESS?

In order to receive your journal without interruption, please complete this change of address notice and forward to the Publisher, 60 days in advance, if possible.

(Please Print)

Old Address:

name

address

city

state (or country)

zip code

New Address

name

address

city

state (or country)

zip code

date new address effective

name of journal

THE LANGUAGE OF SCIENCE  
**Plenum**  
PUBLISHING CORPORATION

**233 Spring Street, New York, New York 10013**

**MEASUREMENT TECHNIQUES**

*Izmeritel'naya Tekhnika*  
Vol. 27, 1984 (12 issues) ..... \$520

**MECHANICS OF COMPOSITE MATERIALS**

*Mekhanika Kompozitnykh Materialov*  
Vol. 20, 1984 (6 issues) ..... \$430

**METAL SCIENCE AND HEAT TREATMENT**

*Metallovedenie i Termicheskaya Obrabotka Metallov*  
Vol. 26, 1984 (12 issues) ..... \$540

**METALLURGIST**

*Metallurg*  
Vol. 28, 1984 (12 issues) ..... \$555

**PROBLEMS OF INFORMATION TRANSMISSION**

*Problemy Peredachi Informatsii*  
Vol. 20, 1984 (4 issues) ..... \$420

**PROGRAMMING AND COMPUTER SOFTWARE**

*Programmirovaniye*  
Vol. 10, 1984 (6 issues) ..... \$175

**PROTECTION OF METALS**

*Zashchita Metallov*  
Vol. 20, 1984 (6 issues) ..... \$480

**RADIOPHYSICS AND QUANTUM ELECTRONICS**

*Izvestiya Vysshikh Uchebnykh Zavedenii, Radiofizika*  
Vol. 27, 1984 (12 issues) ..... \$520

**REFRACTORIES**

*Ogneupory*  
Vol. 25, 1984 (12 issues) ..... \$480

**SIBERIAN MATHEMATICAL JOURNAL**

*Sibirskii Matematicheskii Zhurnal*  
Vol. 25, 1984 (6 issues) ..... \$625

**SOIL MECHANICS AND  
FOUNDATION ENGINEERING**

*Osnovaniya, Fundamenty i Mekhanika Gruntov*  
Vol. 21, 1984 (6 issues) ..... \$500

**SOLAR SYSTEM RESEARCH**

*Astronomicheskii Vestnik*  
Vol. 18, 1984 (6 issues) ..... \$365

**SOVIET APPLIED MECHANICS**

*Prikladnaya Mekhanika*  
Vol. 20, 1984 (12 issues) ..... \$520

**SOVIET ATOMIC ENERGY**

*Atomnaya Energiya*  
Vols. 56-57, 1984 (12 issues) ..... \$560

**SOVIET JOURNAL OF GLASS PHYSICS  
AND CHEMISTRY**

*Fizika i Khimiya Stekla*  
Vol. 10, 1984 (6 issues) ..... \$235

**SOVIET JOURNAL OF  
NONDESTRUCTIVE TESTING**

*Defektoskopiya*  
Vol. 20, 1984 (12 issues) ..... \$615

**SOVIET MATERIALS SCIENCE**

*Fiziko-khimicheskaya Mekhanika Materialov*  
Vol. 20, 1984 (6 issues) ..... \$445

**SOVIET MICROELECTRONICS**

*Mikroelektronika*  
Vol. 13, 1984 (6 issues) ..... \$255

**SOVIET MINING SCIENCE**

*Fiziko-tekhnicheskie Problemy Razrabotki  
Poleznykh Iskopaemykh*  
Vol. 20, 1984 (6 issues) ..... \$540

**SOVIET PHYSICS JOURNAL**

*Izvestiya Vysshikh Uchebnykh Zavedenii, Fizika*  
Vol. 27, 1984 (12 issues) ..... \$520

**SOVIET POWDER METALLURGY AND  
METAL CERAMICS**

*Poroshkovaya Metallurgiya*  
Vol. 23, 1984 (12 issues) ..... \$555

**STRENGTH OF MATERIALS**

*Problemy Prochnosti*  
Vol. 16, 1984 (12 issues) ..... \$625

**THEORETICAL AND MATHEMATICAL PHYSICS**

*Teoreticheskaya i Matematicheskaya Fizika*  
Vol. 58-61, 1984 (12 issues) ..... \$500

**UKRAINIAN MATHEMATICAL JOURNAL**

*Ukrainskii Matematicheskii Zhurnal*  
Vol. 36, 1984 (6 issues) ..... \$500

Send for Your Free Examination Copy

Plenum Publishing Corporation, 233 Spring St., New York, N.Y. 10013

In United Kingdom: 88/90 Middlesex St., London E1 7EZ, England

Prices slightly higher outside the U.S. Prices subject to change without notice.

# RUSSIAN JOURNALS IN THE PHYSICAL AND MATHEMATICAL SCIENCES

AVAILABLE IN ENGLISH TRANSLATION

<b>ALGEBRA AND LOGIC</b> <i>Algebra i Logika</i> Vol. 23, 1984 (6 issues) ..... \$360	<b>HYDROTECHNICAL CONSTRUCTION</b> <i>Gidrotekhnicheskoe Stroitel'stvo</i> Vol. 18, 1984 (12 issues) ..... \$385
<b>ASTROPHYSICS</b> <i>Astrofizika</i> Vol. 20, 1984 (4 issues) ..... \$420	<b>INDUSTRIAL LABORATORY</b> <i>Zavodskaya Laboratoriya</i> Vol. 50, 1984 (12 issues) ..... \$520
<b>AUTOMATION AND REMOTE CONTROL</b> <i>Avtomatika i Telemekhanika</i> Vol. 45, 1984 (24 issues) ..... \$625	<b>INSTRUMENTS AND EXPERIMENTAL TECHNIQUES</b> <i>Pribory i Tekhnika Éksperimenta</i> Vol. 27, 1984 (12 issues) ..... \$590
<b>COMBUSTION, EXPLOSION, AND SHOCK WAVES</b> <i>Fizika Goreniya i Vzryva</i> Vol. 20, 1984 (6 issues) ..... \$445	<b>JOURNAL OF APPLIED MECHANICS AND TECHNICAL PHYSICS</b> <i>Zhurnal Prikladnoi Mekhaniki i Tekhnicheskoi Fiziki</i> Vol. 25, 1984 (6 issues) ..... \$540
<b>COSMIC RESEARCH</b> <i>Kosmicheskie Issledovaniya</i> Vol. 22, 1984 (6 issues) ..... \$545	<b>JOURNAL OF APPLIED SPECTROSCOPY</b> <i>Zhurnal Prikladnoi Spektroskopii</i> Vols. 40-41, 1984 (12 issues) ..... \$540
<b>CYBERNETICS</b> <i>Kibernetika</i> Vol. 20, 1984 (6 issues) ..... \$445	<b>JOURNAL OF ENGINEERING PHYSICS</b> <i>Inzhenerno-fizicheskii Zhurnal</i> Vols. 46-47, 1984 (12 issues) ..... \$540
<b>DIFFERENTIAL EQUATIONS</b> <i>Differentsial'nye Uravneniya</i> Vol. 20, 1984 (12 issues) ..... \$505	<b>JOURNAL OF SOVIET LASER RESEARCH</b> <i>A translation of articles based on the best Soviet research in the field of lasers</i> Vol. 5, 1984 (6 issues) ..... \$180
<b>DOKLADY BIOPHYSICS</b> <i>Doklady Akademii Nauk SSSR</i> Vols. 274-279, 1984 (2 issues) ..... \$145	<b>JOURNAL OF SOVIET MATHEMATICS</b> <i>A translation of Itogi Nauki i Tekhniki and Zapiski Nauchnykh Seminarov Leningradskogo Otdeleniya Matematicheskogo Instituta im. V. A. Steklova AN SSSR</i> Vols. 24-27, 1984 (24 issues) ..... \$1035
<b>FLUID DYNAMICS</b> <i>Izvestiya Akademii Nauk SSSR, Mekhanika Zhidkosti i Gaza</i> Vol. 19, 1984 (6 issues) ..... \$500	<b>LITHOLOGY AND MINERAL RESOURCES</b> <i>Litologiya i Poleznye Iskopaemye</i> Vol. 19, 1984 (6 issues) ..... \$540
<b>FUNCTIONAL ANALYSIS AND ITS APPLICATIONS</b> <i>Funktsional'nyi Analiz i Ego Prilozheniya</i> Vol. 18, 1984 (4 issues) ..... \$410	<b>LITHUANIAN MATHEMATICAL JOURNAL</b> <i>Litovskii Matematicheskii Sbornik</i> Vol. 24, 1984 (4 issues) ..... \$255
<b>GLASS AND CERAMICS</b> <i>Steklo i Keramika</i> Vol. 41, 1984 (6 issues) ..... \$590	<b>MAGNETOHYDRODYNAMICS</b> <i>Magnitnaya Gidrodinamika</i> Vol. 20, 1984 (4 issues) ..... \$415
<b>HIGH TEMPERATURE</b> <i>Teplofizika Vysokikh Temperatur</i> Vol. 22, 1984 (6 issues) ..... \$520	<b>MATHEMATICAL NOTES</b> <i>Matematicheskie Zametki</i> Vols. 35-36, 1984 (12 issues) ..... \$520

continued on inside back cover